Investigating Unexpected but Advantageous Integrated Systems for Solar Water Splitting

Thesis by
Paul D. Nunez

In Partial Fulfillment of the Requirements
for the degree of
Doctor of Philosophy

CALIFORNIA INSTITUTE OF TECHNOLOGY
Pasadena, California

2020
(Defended Oct 23rd, 2019)

Paul Daniel Nunez
ORCID: 0000-0001-7039-0516

ACKNOWLEDGEMENTS

Heart-felt writing is not my forte at all. I find it awkward and foreign so I'll attempt to keep this brief but see where it actually ends up. It's strange to write this section because it signifies the end of an additional decade of education for me—Where I thought I was going end up vs where I actually did is something that I could've never foresaw. My time at the California Institute of Technology has been interesting to say the least. I've had so much personal and professional growth since I first joined in January 2014.

Unlike some of my peers, I never thought a PhD was in my future. I always thought of it as something that was far away and irrelevant to me. This was the case until I had a very memorable conversation with Buddie Mullins around 2011-2012. He directly asked me if I was considering graduate school during a chat in his office. I mentioned that I was considering a masters. He then asked why not consider the PhD to which I replied, 'it would be too expensive,' and demonstrating my lack of knowledge about the PhD. Buddie took the time to help me understand what pursing a PhD actually entailed. It was at this point in time that I even began to consider a PhD as a possibility in my future.

Prior to joining Caltech as a graduate student, I was a summer undergraduate research fellow (SURF) working for my now advisor Nate Lewis, now committee member Harry Gray and mentored by James McKone. That summer in 2012 created and fostered my resolve to attend graduate school at Caltech. It was at that point that I learned what it meant to actually have ownership and direction in research that excited me. This was probably the most memorable summer's in my life. I'm so thankful to have had such a great experience as under the guidance of James, Nate, and Harry.

Once I finally arrived at Caltech, I was able to continue to be intellectually curious because of Nate's flexibility and guidance. Without Nate, I wouldn't have had the same experience that I had in graduate school. Along the way, I was lucky to have been further mentored by Teddy Huang, Joseph Beardslee, and Shu Hu. Unfortunately, for me I was only able to be mentored by them briefly since they subsequently moved on to bigger and better things after a year of mentorship. I would say to anyone that's reading this now, you'll always need a mentor no matter what stage in life you are. My only regret in graduate school is that I learned of this much later piece of advice quite late.

I definitely can say that I wouldn't have gotten as far as I had without the support of my colleagues around me. I've shared so many wonderful memories through the many versions of Jorgenson G131. Although we never managed to have all of the office present at once, it was great to have taken the various 'missing one' pictures. We were always so close! Additionally, I'd like to thank the entirety of the Lewis group for putting up with my 'alternative lifestyle' of never checking emails and falling asleep somewhat reliably during group meeting. And of course, none of this would've been possible without Bruce's guidance, Kimberley's experience, and Barbara's knowledge of Caltech and Nate.

Strangely enough, I first thought that coming to an institute of technology meant that I would learn mostly about science and technology. That turned out to be partially true as a sizable influence in my life at Caltech came through dancing. I still remember making fun of a classmate in undergrad for taking the social dance class. Little did I know that dance would be a passion for me. Since being peer pressured into dancing West Coast Swing by Amanda Shing and Magnus Haw as well as convinced to stay by Rebecca Saive, I've met so many people, traveled the world, and gained a community in the process. Because of this unexpected hobby, I was able to pursue a career in tech in it thanks to my fellow 'westies': Dexter Aronstam, Luan Ruan, and

Daniel Romero. It's because of them that I'm writing this thesis at the headquarters of Pinterest in San Francisco.

To anyone actually reading this: if you don't belong to a community already then go find one. It's a world of a difference. I wish I had found mine sooner. It's the reason I was able to stay sane and happy when nothing was going right. My life is richer and fuller because I found a community I resonate with.

Finally, to my father and mother, I have to thank y'all from bottom of heart for giving me a world of opportunities and supporting me no matter how much of a pain it must've been to raise me. Now that I'm older and wiser, I can see the various ways my life could've turned out and I'm annoyed to say that y'all were right all along. You've given me the brightest future possible and I'm incredibly lucky to have y'all as parents.

ABSTRACT

Advantageous systems are frequently utilized for solar water splitting sometimes are not the most well-understood. Based on fundamental understandings of semiconductor physics, certain combinations of materials should never be advantageous for applications in solar water splitting. (Un)fortunately, these expectations are unrealized. Specifically, we address herein how photogenerated current is able to pass through a-TiO_2 from n-Si as well as the formation of a barrier height from electroless-deposited Pt on p-Si.

Chapter 2 addresses how charge is able to pass through thick layers of atomic layer deposited a-TiO_2 even though the deep valence band of the a-TiO_2 should make the a-TiO_2 act as a blocking layer. It was found that the presence of mid-gap defect states, observable by x-ray photospectroscopy (XPS) valence band spectrum and electron paramagnetic resonance (EPR), in the a-TiO_2 act as a channel for current to pass. The implications of the current traversing through the mid-gap defect states are that global and local changes to the mid-gap defect concentration will strongly affect the amount of current able to pass at all potentials. Thus, the choice of top contacts is limited to metals that have a work-function less than ~5.2 eV else the resistivity would increase.

Chapter 3 focuses on explaining the origin of the barrier height for electroless Pt on p-Si during hydrogen evolution. The work function of Pt should create an ohmic contact which is observed when Pt is e-beam deposited to p-Si. The origin of the barrier height was found to be dependent on the route for charge transfer. Facile redox couples showed that the solution potential of the redox couple controlled the barrier height as charge transferred occurred favorably at the h-terminated surface. While performing hydrogen evolution reaction, the barrier height is formed through the formation of a hydrogen dipole layer that occurs at the interface of the SiO_x|Pt interface.

PUBLISHED CONTENT AND CONTRIBUTIONS

Nunez, P. D., Richter, M. H., Piercy, B. D., Roske, C. W., Cabán-Acevedo, M., Losego, M. D., Konezny, S. J., Fermin, D. J., Hu, S. & Brunschwig, B. S. "Characterization of Electronic Transport through Amorphous TiO_2 Produced by Atomic-Layer Deposition," *J. Phys. Chem. C*, doi:10.1021/acs.jpcc.9b04434.
P.D.N. contributed in the conception of the project, designed the experiments, manufactured the samples, collected measurements, and analyzed the data. The manuscript was prepared by P.D.N. with input from the other co-authors.

Nunez, P.D., Cabán-Acevedo M., Yu W., Richter M. H., Kennedy K., Villarino A. M., Brunschwig B. S., & Lewis N. S. "Investigation of the Mixed-Barriers in and Electroless Deposited Platinum Nanoparticles on p-Si," *in preparation.*
P.D.N. contributed to the conception of the project, designed the experiments, manufactured the samples, collected measurements, and analyzed the data. The manuscript was prepared by P.D.N with input from the other co-authors.

TABLE OF CONTENTS

LIST OF ILLUSTRATIONS AND/OR TABLES

Chapter 2

Chapter 1

INTRODUCTION

In order to mitigate and maybe even reverse the adverse effects of anthropogenic CO_2 production, replacing fossil fuels with fuel produced by solar energy is an attractive option. The amount of energy from the Sun that irradiates the entire Earth in an hour and a half could have powered the world for the year 2001. Solar energy is an attractive alternative due its overwhelming abundance. However, solar energy is a very intermittent energy source. Thus, having a way to capture, convert and efficiently store solar energy is required in order for it to be a large-scale solution. Solar water splitting is a potential solution to the intermittency of solar energy which could further its wide-scale adoption in order to decrease or even reverse the anthropogenic production of CO_2.

As attractive an option as solar water splitting is, many challenges exist that prevent its wide-scale adoption. First and foremost, a solar water splitting device must be efficient, inexpensive, and stable. Currently, at best, only two of the three aforementioned criteria can be attained in a single device. Several methods exist to 'circumvent' the necessary requirements for a successful water splitting device. One such method is to tack-on stability through a protection layer to make efficient, inexpensive, but unstable semiconductors a viable option. The second method is to improve the efficiency of inexpensive and stable semiconductors through the addition of catalysts without the formation of expensive buried-junctions.

Many methods to tacking-on stability have been explored and have achieved some levels of success. One of the most successful protections, to date, has been the atomic

layer deposited (ALD) amorphous TiO_2 (a- TiO_2). This protection layer greatly enhances the stability of various n-type semiconductors (e.g. n-Si, n-GaAs, n-GaP, n-CdTe). However, the stability achieved by using this protection is not the only remarkable trait about the a-TiO_2. The a-TiO_2 protection layer should never have worked as well as it did with the aforementioned n-type semiconductors for the thicknesses that was deposited.

The deep valence band of TiO_2 should have made the protection layer act as a blocking layer for charge-transfer. Previous iterations of TiO_2 protection layers have observed this blocking layer behavior, as layers have to be ultra-thin (< 5 nm) to allow for current to pass. However, devices with the ALD a-TiO_2 were able to operate efficiently for thickness greater than 100 nm without affecting the current. Although the result did not follow previous predictions of its behavior, this did not stop researchers from using the protection layer without fully understanding the nuances around the a-TiO_2. Chapter 2 investigates the source of the discrepancy and how to efficiently utilize the uncovered information to design more efficient photoanodes using the a-TiO_2 for solar water splitting.

Just like the a-TiO_2 defying expectations, the addition of Pt to p-Si via the electroless deposition for solar hydrogen production has a large discrepancy that has never been fully addressed. Although, Pt is an excellent catalyst for the hydrogen evolution reaction, the work function of Pt is so large compared to the band positions of p-Si that the combination of the two materials is expected to create an ohmic contact. Thus, this ohmic contact should render the p-Si|Pt device useless for solar hydrogen production.

This expectation is met whenever Pt is physically deposited to p-Si by means of physical depositions like sputtering or e-beam evaporation. The junction that is produced is ohmic and is unable to use light to drive hydrogen production. However,

Pt deposited by the electroless deposition method to p-Si violates the expectation as the junction that is produced is rectifying and able to use light to drive hydrogen production. Many hypotheses exist to explain the origin of the apparent rectifying junction that is formed by electroless deposition. However, no hypothesis has been systematically proven to be the origin of the apparent rectifying junction. Chapter 3 investigates the origin for the rectification and provides a model to explain the origin of the rectification as well as gives guidance on how to further enhance the rectifying junction.

Between these two systems, they have the common theme in which they are unexpectedly performant integrated systems. These systems are more complex than the simple models used to predict their behavior. This thesis provides guidance and slightly more complex models that can be used to explain the behavior of these systems and indicate potential next steps to further improve their performance.

Chapter 2

CHARACTERIZATION OF ELECTRONIC TRANSPORT THROUGH AMORPHOUS TIO_2 PRODUCED BY ATOMIC LAYER DEPOSITION

Nunez, P.D., Richter, M. H., Piercy, B. D., Roske, C. W., Cabán-Acevedo, M., Losego, M. D., Konezny, S. J., Fermin, D. J., Hu, S. & Brunschwig, B. S. Characterization of Electronic Transport through Amorphous TiO_2 Produced by Atomic-Layer Deposition. *J. Phys. Chem. C*, doi:10.1021/acs.jpcc.9b04434.

2.1 Abstract

Electrical transport in amorphous titanium dioxide (a-TiO_2) thin films, deposited by atomic layer deposition (ALD), and across heterojunctions of p^+-Si|a-TiO_2|metal substrates that had various top metal contacts has been characterized by ac conductivity, temperature-dependent dc conductivity, space-charge-limited current spectroscopy, electron para- magnetic resonance (EPR) spectroscopy, X-ray photoelectron spectroscopy, and current density versus voltage (J−V) characteristics. Amorphous TiO_2 films were fabricated using either tetrakis(dimethylamido)-titanium with a substrate temperature of 150 °C or $TiCl_4$ with a substrate temperature of 50, 100, or 150 °C. EPR spectroscopy of the films showed that the Ti^{3+} concentration varied with the deposition conditions and increases in the concentration of Ti^{3+} in the films correlated with increases in film conductivity. Valence band spectra for the a-TiO_2 films exhibited a defect-state peak below the conduction band minimum (CBM), and increases in the intensity of this

peak correlated with increases in the Ti^{3+} concentration measured by EPR as well as with increases in film conductivity. The temperature-dependent conduction data showed Arrhenius behavior at room temperature with an activation energy that decreased with decreasing temperature, suggesting that conduction did not occur primarily through either the valence or conduction bands. The data from all of the measurements are consistent with a Ti^{3+} defect-mediated transport mode involving a hopping mechanism with a defect density of 10^{19} cm^{-3}, a 0.83 wide defect band centered 1.47 eV below the CBM, and a free-electron concentration of 10^{16} cm^{-3}. The data are consistent with substantial room-temperature anodic conductivity resulting from the introduction of defect states during the ALD fabrication process as opposed to charge transport intrinsically associated with the conduction band of TiO_2.

2.2 Introduction

Water oxidation to evolve $O_2(g)$ is a key process in the (photo-)electrochemical production of carbon-neutral fuels. Semiconductors with band gaps, E_g, that allow substantial absorption of sunlight ($E_g < 2$ eV) typically corrode either through dissolution or through the formation of an insoluble insulating surface oxide, when placed in contact with an aqueous electrolyte and poised at a potential sufficiently positive to drive the water-oxidation half-reaction.[1] Such corrosion impedes the development of fully integrated solar fuel devices that involve immersion of semiconductors in an electrolyte[2] and is especially rapid in strongly acidic or strongly alkaline electrolytes that are compatible with efficient operation of electrochemical cells and with existing ion-exchange membranes.[3] Coating such semiconductors with films that combine transparent, conductive oxides with active catalysts for the oxygen evolution reaction (OER) has been shown to extend the lifetime of semiconductor anodes in aqueous electrolytes from seconds to hours or

months,[4–13] depending on the specific materials and test conditions.

Coatings of amorphous TiO_2 (a-TiO_2) supporting a Ni OER catalyst provide stability against corrosion of technologically important n-type semiconductors, including n-Si, n-GaAs, and n-CdTe, in strongly alkaline electrolytes under water oxidation conditions.[4,14] The relative alignment between the valence band maximum (VBM) of these n-type materials and the VBM of n-type TiO_2 ($E_g \approx 3.3$ eV) predicts an ~2 eV barrier to the transport of holes from the smaller band gap material into a-TiO_2.[15] Nevertheless, these heterojunction devices support high anodic current densities (>100 mA cm^{-2}).[4,14] Conduction through a-TiO_2 films has been shown to be essentially independent of the film thickness, with high conductance observed for films as thick as 143 nm; however, the interfacial conductance is strongly dependent on the top contact. Specifically, to drive anodic current densities of 50−120 mA cm^{-2}, an Ir top contact increased the voltage required by ~400 mV relative to devices with Ni top contacts.[4] X-ray photoelectron spectroscopic (XPS) data indicate a band alignment that produces rectifying behavior for a-TiO_2 interfaces with n-Si and n^+-Si surfaces and an Ohmic contact between a-TiO_2 and p^+-Si.[16] Ambient-pressure XPS (AP-XPS) data of p^+-Si|a-TiO_2 electrodes under potential control indicate that the addition of Ni to the surface of a-TiO_2 changes the electrical behavior of the a-TiO_2|liquid junction. Bare a-TiO_2 electrodes in contact with the solution are “rectifying” for the oxidation of water or $Fe(CN)_6^{4-}$. This rectifying behavior is also observed for contact between a Hg droplet and bare a-TiO_2. The addition of a Ni layer to a-TiO_2 makes the junction Ohmic, removing a large energetic barrier to conduction across a-TiO_2.[17]

These data provide a detailed picture of the energetics at n-Si|a-TiO_2|Ni|1.0 M KOH

(aq) interfaces. However, the mechanism of conduction across the n-Si|a-TiO_2|Ni junctions, despite the unfavorable band alignment energetics, remains to be elucidated. XPS valence band data show a weak peak ~2 eV above the VBM, suggesting the possibility of defect-based transport.[4] However, subsequent studies have observed anodic conduction by TiO_2 films synthesized using various techniques, including crystalline films, and did not yield a dependence of conduction on defect states.[18] For TiO_2-coated photocathodes, conduction occurs via electron transport in the TiO_2 conduction band.[19–21] Such electron transport mediated by the conduction band has been hypothesized to be a generic mechanism applicable to photoanodes, with TiO_2 operating as an Ohmic contact to the underlying n-type semiconductor, with electrons being transported from solution via the TiO_2 conduction band recombining with holes at the semiconductor|TiO_2 junction.[22]

Ti^{3+} states [observable by electron paramagnetic resonance (EPR) and XPS valence band spectra] play a large role in the conductivity, light absorption, and many other properties of TiO_2.[23–30] The mechanism of facile hole conduction through a-TiO_2, despite the 3.0 eV band gap and unfavorable band edge energetics for either electron or hole conduction from small band gap inorganic semiconductors, has not yet been elucidated. A greater understanding of the transport mechanism would provide insight into the utility and mechanism underpinning the use of atomic layer deposition (ALD) of a-TiO_2 as a protection layer for a wide variety of photoanodes.

We describe herein a detailed investigation of conduction across p^+-Si|a-TiO_2 junctions, including temperature-dependent dc conductivity, ac conductivity, space-charge-limited current (SCLC) spectroscopy, EPR spectroscopy, and XPS.

The experiments were designed to elucidate the mechanism of anodic conduction in a-TiO_2 layers as well as the factors that control the observed conductivity as the metal contact to the a-TiO_2 layer is varied. We consequently have explored the role of defect states in conduction across a-TiO_2 films fabricated by a variety of methods as well as the importance of the energy-band positions of Si and the top contact relative to the TiO_2 band positions. We have moreover applied the information gained from these studies to aid in the design of stable Si|a-TiO_2 photoanodes with high fill factors for solar-driven water oxidation in contact with acidic aqueous electrolytes.

2.3 Experimental Section

2.3.1 Sample Preparation

Materials and Chemicals

Water with resistivity, ϱ, > 18 MΩ cm was obtained from a Barnstead Millipore purification system and was used throughout. All chemicals, including sulfuric acid (99.999%, Sigma-Aldrich and ~18 M, ACS Reagent Grade, J.T. Baker), hydrogen peroxide (~30%, ~13 M, VWR), hydrochloric acid (ACS Grade, VWR), and buffered HF (aq) (semiconductor-grade, Transene) were used as received, unless otherwise noted. Two types of crystalline, single-side polished Si substrates were used: p^+-Si(100) (boron-doped, ϱ < 0.002 Ω cm, Addison Engineering) and n-Si(100) (phosphorus-doped, ϱ = 2–3 Ω cm, Addison Engineering).

Preparation of Substrates

The Si wafers were cleaned using an RCA SC-1 procedure that consisted of a 10 min soak in a 3:1 (by volume) solution made from 3 parts H_2SO_4 (aq) (~18 M) and 1 part H_2O_2 (aq) (~13 M). The samples were then briefly etched in a solution of buffered HF (aq) (Transene). The Si samples were cleaned using an RCA SC-2

procedure by soaking the samples for 10 min at 75 °C in a 5:1:1 (by volume) solution of H_2O, HCl (aq) (~11 M), and H_2O_2 (aq) (~13 M). The RCA SC-2 procedure left a thin passivating oxide layer on the Si surface.

ALD of TiO_2 Thin Films

TiO_2 films were grown using two different precursors, tetrakis(dimethylamido)-titanium (TDMAT) and $TiCl_4$. For TiO_2 films prepared from the TDMAT precursor, a Cambridge Nanotech S200 or Fiji F200 ALD system was used to deposit TiO_2 films onto Si wafers or onto Pyrex micro cover glass slides (VWR). The defect characteristics of TiO_2 were similar for films prepared from either reactor. Each ALD cycle consisted of a 0.10 s exposure to TDMAT (Sigma-Aldrich, 99.999%), a N_2(g) (Airgas, 99.999%) purge, a 0.015 s exposure to H_2O, and a final N_2(g) purge. Research grade 20 sccm N_2(g) was used for the N_2(g) purges, and each N_2(g) purge was 15 s in duration. During deposition, the substrate and the TDMAT precursor were heated to 150 and 75 °C, respectively, while the H_2O remained at room temperature. Most samples were prepared with 1500 cycles, giving a nominal thickness of 68 nm. The thickness was chosen to be consistent with a previous work. At this thickness, a-TiO_2 minimizes the reflection as a single-layer antireflection coating while still providing facile electronic conduction and corrosion protection of the underlying photoanode.[31]

TiO_2 films from the $TiCl_4$ precursor were deposited onto p^+-Si substrates in a hot-wall, flow-tube reactor with custom-designed sequencing software.[32] The precursor gas lines were maintained at 110 °C, whereas the precursor was maintained at room temperature. Each ALD cycle consisted of a 0.20 s exposure to $TiCl_4$ (Strem, 99%), a 45 s N_2(g) purge, a 0.10 s exposure to H_2O, and a final 30 s N_2(g) purge, and the N_2(g) flow rate was 150 sccm. Films were deposited to a predetermined thickness

of ~60 nm at chamber temperatures of 50, 100, or 150 °C. The film thickness and refractive index were measured via spectroscopic ellipsometry (J.A. Woollam Co., alpha-SE) and were fit to a Cauchy model.

Electron-Beam Metal Deposition

Samples were patterned via optical lithography, mounted with a double-sided carbon tape, and pumped down to a base pressure of $<10^{-5}$ Torr in an electron-beam evaporator system (Angstrom Engineering Inc.). Ti, Mg, Ni, Au, Ir, Pt, and Pd were evaporated from the source metals that had a purity of at least 4 N. Deposition rates ranged from 0.020 to 0.080 nm s^{-1}, as monitored by a quartz crystal microbalance. Deposition was stopped when the film thickness exceeded ~35 nm.

Electrode Fabrication

Electrodes were fabricated by using a scribe to cleave the e-beam deposited samples into ~0.1 cm^2 pieces. The samples were patterned into isolated pads for solid-state measurements or into islands for electrochemical measurements. A positive photoresist, S1813 (Shipley), was patterned, metal pads or islands were deposited, and then the photoresist was removed by gently sonicating in acetone for ~1 min to leave the desired pattern. Ohmic contact was made by scratching the back of the p^+-Si or n-Si sample with an In–Ga eutectic (Alfa Aesar, 99.999%), and the back contact to the sample was affixed to a Cu wire with a double-sided Cu tape. The Cu wire was threaded through a glass tube (Corning Incorporation, Pyrex tubing, 7740 glass), and all but front of the sample was encapsulated with Loctite epoxy (Hysol 9462). After curing overnight, the electrode was scanned with an Epson scanner (V370) and analyzed with ImageJ software to determine the area of the exposed region, which was ~0.1 cm^{-2}.

2.3.2 Conductivity Measurements

Current density versus voltage (J–V) data were collected on solid-state samples that had various combinations of metal contacts on degenerately boron-doped p^+-Si substrates coated with a-TiO_2. The electrical data were collected using a Bio-Logic SP-200 potentiostat in a two-electrode setup, with the working electrode lead connected to the bottom contact (Si back-side) and the counter and reference electrode leads connected to the top contact (metal pad). For electrical contact, In–Ga eutectic was scratched onto the back of Si as well as onto the top side of the double-sided Cu tape that had been affixed to a glass slide for structural support. J–V data were collected at 100 mV s^{-1}, starting at an applied bias of 0 V versus the counter electrode.

Temperature-Dependent Conductivity

The substrates for the measurements were p^+-Si wafers coated with 1500 cycles (~68 nm) of ALD a-TiO_2 that was then patterned with Ni islands. During the variable temperature measurement, the samples were loaded into a Janis CCS-100/204N cryostat, and J–V data were obtained from 10 to 310 K using an Agilent B1500A semiconductor device analyzer with medium-power source-measurement modules as well as atto-sense and switch units for high-resolution current sensing. The conductivity was obtained by fitting the measured resistance data to a computational model using the ac/dc module in COMSOL Multiphysics software.

For resistance measurements from 180 to 300 K, the samples were loaded into another cryostat. In both temperature-dependent measurements, the temperature of the sample was controlled using a Lake Shore auto-tuning temperature controller with a Si diode temperature sensor placed in thermal contact with the sample.

Potential-Dependent Conductance Measurements on Electrochemical Field-

Effect Transistors

The conductance of a-TiO_2 films in contact with an electrolyte solution was measured with interdigitated electrodes (IDEs) in an electrochemical field-effect transistor (EC-FET) configuration.[33,34] The substrates for the measurements were clean glass microscope slides that had been lithographically patterned with 224 interdigitated Ti fingers of dimensions 20 μm × 2 mm × 100 nm (width × length × thickness). Alternate fingers were spaced 20 μm apart from one another. The substrate had 1500 cycles (~68 nm) of a-TiO_2 deposited via ALD. The front contacts were kept free of the deposited material by means of a glass slide as a physical mask. The conductance of a-TiO_2 in contact with 1.0 M H_2SO_4 (aq) was measured using a Bio-Logic SP-300 bipotentiostat that allowed control of the potential of each electrode (channels) of the IDE array independently with respect to the reference electrode in the solution. Both channels were set to the desired gate potential (V_{gate}), and the capacitance current was allowed to decay for 30 s to establish the electron occupancy in the film and to set the potential of the film relative to the reference potential. The potential of channel 2 was then offset by ±25 mV with respect to channel 1, and the source–drain potential (V_{SD}) was varied in 10 mV increments. Under the conditions investigated, the source–drain current (I_{SD}) was proportional to V_{SD}, allowing an estimate of the film conductance as a function of V_{gate}. V_{gate} was varied across the potential range between the onset of accumulation and deep depletion. The film conductivity was calculated using an IDE cell constant, K_{IDE}, of 0.045 cm^{-1}, which was estimated from the geometry of the IDE[35] using eq 1

$$K_{IDE} = \frac{2(S/W)^{1/3}}{l(n-1)} \quad (1)$$

where s is the spacing between the electrode digits (20 μm), w is the width of the

electrode (20 μm), l is the length (2 mm), and n is the number of digits (224). This process produced a cell constant of $K_{ide} = 0.045\ cm^{-1}$. The measured conductance, G_{ecfet}, was converted to units of conductivity using eq 2

$$\sigma_{ecfet} = K_{ide} G_{ecfet} \quad (2)$$

2.3.3 Physical Characterization of a-TiO_2

EPR Spectroscopy

EPR spectra were collected at 77 K using a Bruker EMX X-band continuous-wave spectrometer. Data were collected for samples in liquid N_2 in a finger Dewar. Samples were prepared by depositing 1500 ALD cycles of a-TiO_2 onto VWR micro-cover glass slides (0.15 ± 0.02 micron thick). The slides were then diced into 2×2 mm^2 pieces using a Dynatex GST-150 scriber-breaker. The diced samples were then placed in EPR tubes.

Because of sample variations, all of the TiO_2 (50, 100, and 150 °C $TiCl_4$ and TDMAT) films were of slightly different thickness as measured by ellipsometry. To ensure that a uniform amount of TiO_2 was maintained between samples, the total area was varied. For instance, if TDMAT and 50 °C $TiCl_4$ TiO_2 had a thickness of 68 and 62 nm, respectively, then the area ratio of TDMAT:50 °C $TiCl_4$ TiO_2 was adjusted to 1.0:1.1 to ensure an equivalent amount of TiO_2.

Photoelectron Spectroscopy

XPS data were collected on ALD-deposited a-TiO_2 on p^+-Si using a Kratos Axis Ultra system with a base pressure of 1×10^{-9} Torr. The X-ray source was a monochromatic Al Kα line at 1486.6 eV. Photoelectrons were collected at 0° from

the surface normal with a retarding pass energy of 160 eV for survey XPS scans, 10 eV for high-resolution core levels, and 20 eV for valence band XPS scans.

Work function measurements were performed using He I ultraviolet photoelectron spectroscopy (UPS) on a Kratos Axis Ultra system. A pass energy of 5 eV was used in conjunction with an aperture of 110 μm. Prior to the measurements, pure metal samples (>99.99%) were sputter-cleaned for 30 min with 4 kV argon ions. The work function (ϕ_{WF}) was calculated from the measured spectra on a kinetic energy scale using eq 3

$$\Phi_{WF} = E_{sec,meas} - E_{F,meas} \quad (3)$$

where $E_{sec,\,meas}$ and $E_{F,\,meas}$ are the measured energy of the secondary electron cutoff and the Fermi energy, respectively, and 21.21 eV is the photon energy for He I excitation. The secondary electron cutoff and the Fermi energy were obtained by calculating the intercept of a linear fit of the steep electron cutoff to that of the background and by fitting a Fermi distribution to the VBM, respectively.

Secondary-Ion Mass Spectroscopy

Secondary-ion mass spectroscopy (SIMS) data were collected on a Cameca SIMS-7f GEO instrument. A 100 μm × 100 μm area of the sample surface was ionized and sputtered by a 7 keV Cs^+ primary ion beam with no substrate biasing. A mass spectrometer collected and analyzed the ejected secondary ions. The count rates of ^{30}Si, ^{48}Ti, $^{12}C + {}^{133}Cs$, and $^{14}N + {}^{133}Cs$ were collected as a function of the sputtering cycle. SIMS data were collected for all TDMAT and $TiCl_4$ a-TiO_2 films.

Attenuated Total Reflection Infrared Spectroscopy

Attenuated total reflection infrared spectroscopy (ATR-IR) spectra were collected

using a Thermo Scientific Nicolet 6700 optical spectrometer equipped with a thermoelectrically cooled deuterated L-alanine-doped triglycine sulfate detector, an electronically temperature-controlled EverGlo mid-IR source, a N_2(g) purge, a KBr beam splitter, and a diamond ATR crystal single-reflection Smart-iTR accessory. After data collection, the spectra for ALD films on the glass substrate were corrected using pristine glass as the background. Air was used as the background for ALD films deposited on the silicon substrate. In addition, the baseline was flattened when needed. TIRS data collection and processing was performed using OMNIC software v.9.2.41.

2.3.4 Electrochemical Characterization

Electrochemical data were obtained using a Bio-Logic SP-200 potentiostat in a three-electrode configuration with 1.0 M H_2SO_4 (aq) as the electrolyte. A carbon rod (Strem Chemicals, 99.999%) was used as the counter electrode, and a $Hg/HgSO_4$ electrode (Gamry Instruments) was used as the reference electrode. An ELH-type tungsten-halogen lamp provided light that passed through a quartz diffuser to reach the Pyrex electrochemical cell. The illumination intensity was measured by a Si photodiode (Thorlabs), and the light intensity was adjusted to produce the same current on the photodiode as was produced by illumination with 100 mW cm^{-2} of Air Mass 1.5 sunlight. Cyclic voltammetric (CV) data were collected at a 40 mV s^{-1} scan rate.

2.4 Results

2.4.1 Work Function of the Metals

Figure S1 shows the representative work function measurements by UPS for Ni, Pd, Pt, Ir, and Au. The spectra allowed determination of the work functions for these polycrystalline metals (purity > 99.99%) as 5.09 ± 0.4, 5.27 ± 0.2, 5.56 ± 0.07, 5.32 ± 0.2, and 5.05 ± 0.3 eV for Ni, Pd, Pt, Ir, and Au, respectively. These work function

values are in good agreement with prior work function measurements on polycrystalline metals.[36–38] The work functions of Mg and Ti were taken to be 3.66 ± 0.2 and 4.33 ± 0.2 eV, respectively.[36]

2.4.2 Conductivity of p^+-Si|a-TiO_2|metal Devices

J–V Characteristics of p^+-Si|a-TiO_2|metal Devices

Figure 1 shows the representative solid-state J–V characteristics for p^+-Si|a-TiO_2|metal devices with a-TiO_2 grown on p^+-Si substrates via 1500 ALD cycles using a TDMAT precursor and a substrate temperature of 150 °C. The ALD procedure yielded ~68 nm-thick a-TiO_2 films. The J–V characteristics showed Ohmic (linear) behavior at biases <50 mV. Figure S2 shows the normalized differential conductance as a function of the applied bias for a p^+-Si|a-TiO_2|Ni device, which is consistent with the behavior typical of dielectric films.[39,40]

The current density passed as a function of the applied bias depended on the top contact, Figure 1, with devices having Ti, Mg, or Ni top contacts behaving almost mutually identically, especially at low biases. At the same applied bias, devices with Au, Ir, Pt, or Pd top contacts passed ≤10% of the current densities of devices having Ti, Mg, or Ni as a top contact. For example, at an applied bias of 0.1 V, devices with Ti, Mg, or Ni top contacts passed current densities of ~60 mA cm^{-2}, as compared to the current densities passed by devices with Au (8.7 mA cm^{-2}), Ir (5.5 mA cm^{-2}), Pt (3.6 mA cm^{-2}), or Pd (1.5 mA cm^{-2}) contacts. Compared to devices with Ti, Mg, or Ni top contacts, the devices with Au, Ir, Pt, or Pd top contacts required an additional 90–250 mV of bias to pass current densities of 10 mA cm^{-2} as well as an additional 150–330 mV of bias to pass current densities of 30 mA cm^{-2}. The conductivities at low applied biases (<50 mV) were determined from linear fits of the data (Figure 1) and tabulated in Table 1. The contact resistances were determined

by transmission line measurements, and the compensated voltages between different metal contacts were measured for representative devices (Table S1). Although the contact resistance increased as the work function of the metal increased, the metals with higher work functions yielded sufficiently low current densities that the total voltage compensation would not create a noticeable change in the J–V behavior over the measurement range depicted in Figure 1.

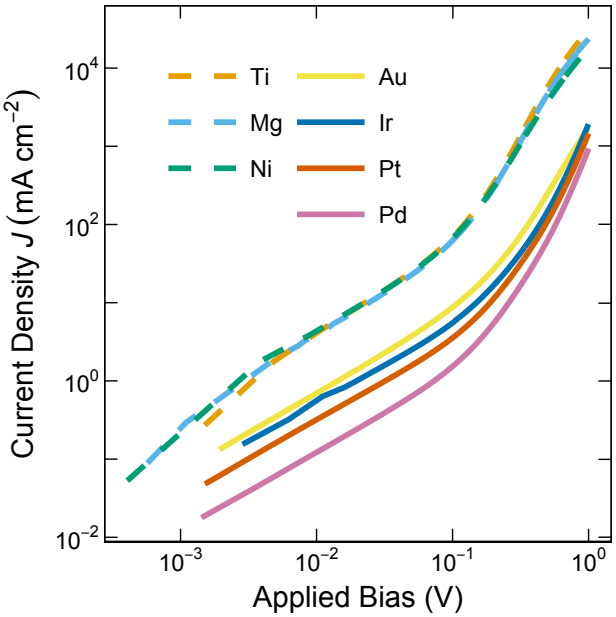

Figure 1. Current density (J) vs applied bias (V) for solid-state p^+-Si| a-TiO_2|metal devices. a-TiO_2 was ~ 68 nm thick. The devices were tested in a two-electrode configuration, and the bias was applied across the device using the p^+-Si side as the working electrode and the metal side as the counter electrode.

Table 1. Conductivities for the devices with varied metal contacts as determined from a fit of the *J*-*V* behavior in the low-bias regions. At least 5 samples with each metal were tested, and error estimates represent one standard deviation.

Top Contact	Conductivity (S cm^{-1})	Work Function (eV)
Ti	$(85 \pm 18) \times 10^{-5}$	4.33 ± 0.20
Mg	$(85 \pm 1.2) \times 10^{-5}$	3.66 ± 0.20
Ni	$(95 \pm 4.0) \times 10^{-5}$	5.09 ± 0.39
Au	$(13 \pm 1.7) \times 10^{-5}$	5.05 ± 0.30
Ir	$(4.0 \pm 1.6) \times 10^{-5}$	5.32 ± 0.18
Pt	$(8.3 \pm 1.8) \times 10^{-5}$	5.56 ± 0.07
Pd	$(2.3 \pm 0.45) \times 10^{-5}$	5.27 ± 0.18

SCLC Spectroscopy

Figure 2a shows the plot of the J–V characteristics for a p^+-Si|a-TiO_2|Pt device, extended to 5 V of applied bias. At ~5 V, the current increased abruptly, consistent with a SCLC in the trap-free regime.[41–44] Similarly, extended J–V characteristics can be seen in Figure S3 for devices with Au, Ir, or Pd contacts. The number of traps, the majority charge-carrier mobility, and the charge-carrier concentration were calculated from the threshold voltages for trap filling, the J–V behavior in the trap-free regime, and the J–V behavior in the Ohmic regime, respectively, according to eqs 4–6[41–44]

$$V_{TF} = \frac{qN_T L^2}{\varepsilon_0 \varepsilon} \tag{4}$$

$$J_{TF} = \frac{9\varepsilon\mu V^2}{8L^3} \tag{5}$$

$$J_{\Omega} = \frac{qn\mu V}{L} \tag{6}$$

where V_{TF} is the threshold voltage for trap filling, J_{TF} is the current density in the trap-free region, J_{Ω} is the current density in the Ohmic region, q is the absolute charge of an electron, N_T is the trap density, L is the thickness of the sample, ε_0 is the permittivity of free space, ε (=112) is the dielectric constant of TiO_2, μ is the mobility of the majority carriers, and n is the mobile charge-carrier density. The calculated trap densities, mobilities, and effective mobile charge-carrier densities for p^+-Si|a-TiO_2|metal devices with various metal top contacts are tabulated in Table

S2.

Figure 2b shows the dependence of the number of traps measured by SCLC spectroscopy on the work function of the top contact used for the p^+-Sila-TiO_2|metal device.[36,45,46] The number of traps measured by SCLC decreased only slightly as the work function of the top contact increased. For low-work-function metals, the trap concentration could not be measured before the voltage limits of the potentiostat were reached, implying trap densities $>1.5 \times 10^{19}$ cm^{-3}.

Figure 2c shows the variation of the calculated free-carrier concentration for each metal contact as a function of the work function of each metal. The free-carrier concentration was calculated by using the value of the mobility found in the trap-free regime (eq 5) with a Pt contact ($6.5 \pm 3 \times 10^{-4}$ cm^2 V^{-1} s^{-1}), in conjunction with the slopes of the Ohmic regions for various top contacts, according to eq 6. Below a work function of ~5.2 eV, the (averaged) carrier concentration was essentially independent of the work function of the top metal contact, whereas for a work function >5.2 eV, the (averaged) free-carrier concentration becomes dependent on the work function and thus decreased by 10^1 to 10^2 cm^{-3}. Although the mobility is not a constant for different dopant concentrations, the mobility was approximated to be independent of the free-carrier concentrations. This approximation is in agreement with the free-carrier density measured previously by Hall measurements with In contacts (Figure 2c).[4] In addition, the mobility measured is in agreement with the predicted mobility of 2×10^{-4} cm^2 V^{-1} s^{-1} by Pham and Wang using density functional theory (DFT) + U methods.[47]

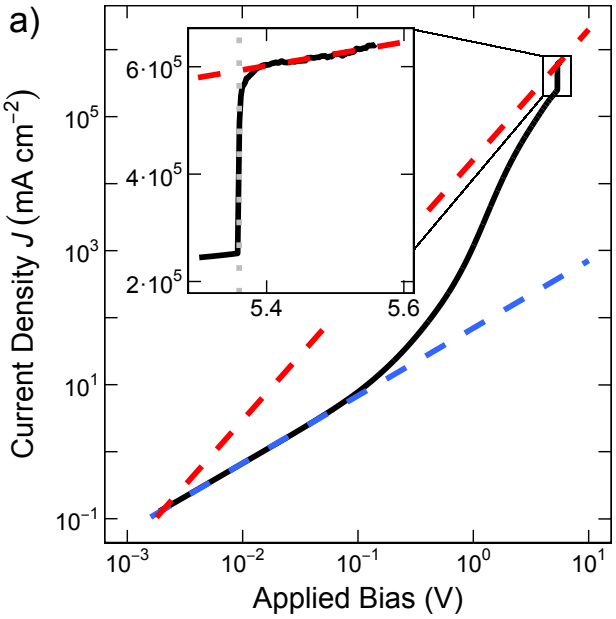
a)
Current Density J (mA cm^{-2})
Applied Bias (V)
10^{5}
10^{3}
10^{1}
10^{-1}
10^{-3}
10^{-2}
10^{-1}
10^{0}
10^{1}
$6{\cdot}10^{5}$
$4{\cdot}10^{5}$
$2{\cdot}10^{5}$
5.4
5.6

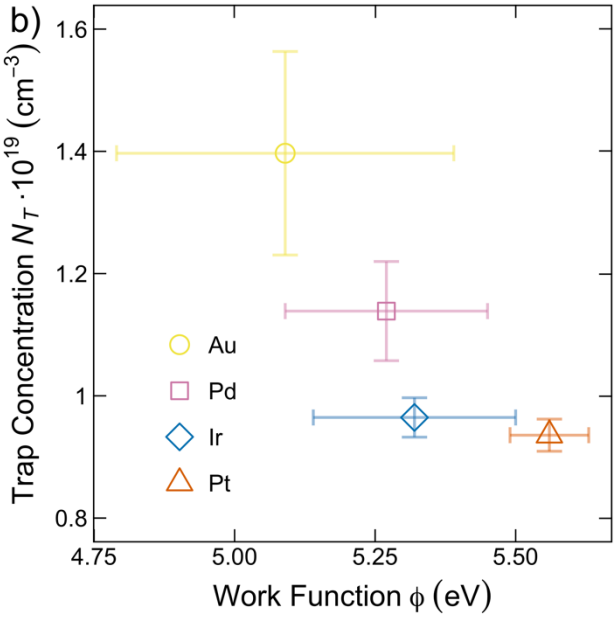
b)
Trap Concentration $N_T \cdot 10^{19}$ (cm^{-3})
Work Function ϕ (eV)
1.6
1.4
1.2
1
0.8
4.75
5.00
5.25
5.50
Au
Pd
Ir
Pt

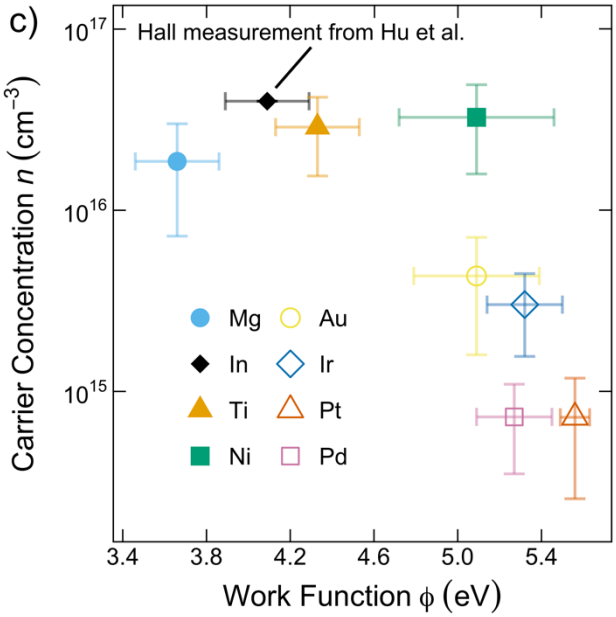

Figure 2. (a) J–V characteristics of a solid-state p^+-Sila-TiO_2|Pt device extended to applied biases >5 V. a-TiO_2 was ~68 nm thick. The inset is a plot of the crossover into the trap-filled regime. Linear regressions are shown for the Ohmic region at a low bias (blue dashed line) and for the trap-filled space-charge-limited regimes (red dashed line in the inset). (b) Concentration of trap states for devices with top contacts to high-work-function metals. (c) Calculated free-carrier concentrations for varied metal top contacts.

ac Conductivity

Figure 3 shows the ac conductivity as a function of frequency for a p^+-Sila-TiO_2|Ni device at room temperature and under an applied bias of 300 mV. The conductivity of the sample was 3.0×10^{-6} S cm^{-1} for frequencies $\leq 10^5$ Hz and increased exponentially at frequencies $>1 \times 10^4$ Hz.

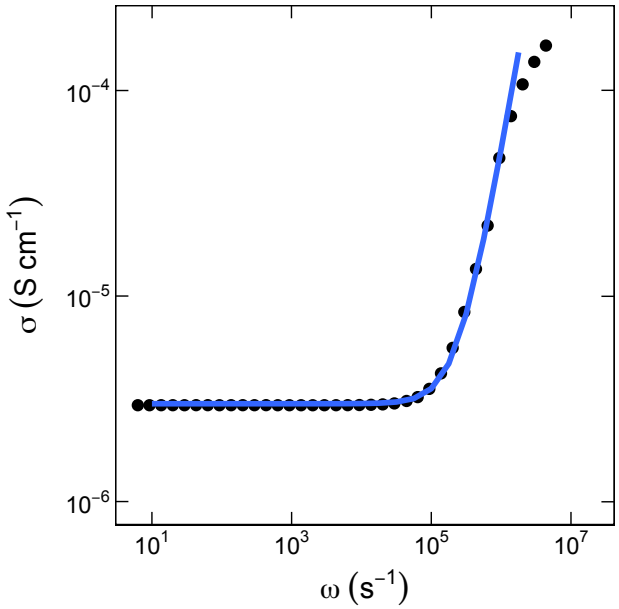

Figure 3. ac conductivity of a solid-state p^+-Si|a-TiO_2|Ni device measured in a two-electrode configuration with a bias of 300 mV applied between the p^+-Si side and the Ni side of the device. The blue line shows a fit of the frequency-dependent region of the data to a power-law model, $\sigma(\omega) = \sigma_{dc} + A\omega^s$, where $\sigma_{dc} = 2.99 \times 10^{-6}$ S cm^{-1}, $A = 9.9 \times 10^{-17}$ S cm^{-1} s$^{1.95}$, and s = 1.95.

Temperature-Dependent Conductivity Ni|a-TiO_2|Ni Devices

Figure 4 shows the conductivity as a function of temperature for a Ni|a-TiO_2|Ni through-layer device in which the thickness of the a-TiO_2 layer was 68 nm, measured at temperatures between 10 and 310 K. The data showed two regions, each with an Arrhenius-type exponential temperature dependence. Activation energies for charge transport were calculated from the slopes of the linear fits. The model yielded an activation energy of 350 ± 15 meV for charge transport at temperatures in the 250–310 K range, which is substantially larger than the ~7 meV activation energy calculated for charge transport at temperatures in the 100–125 K range. The activation energy continuously decreased as the temperature decreased.

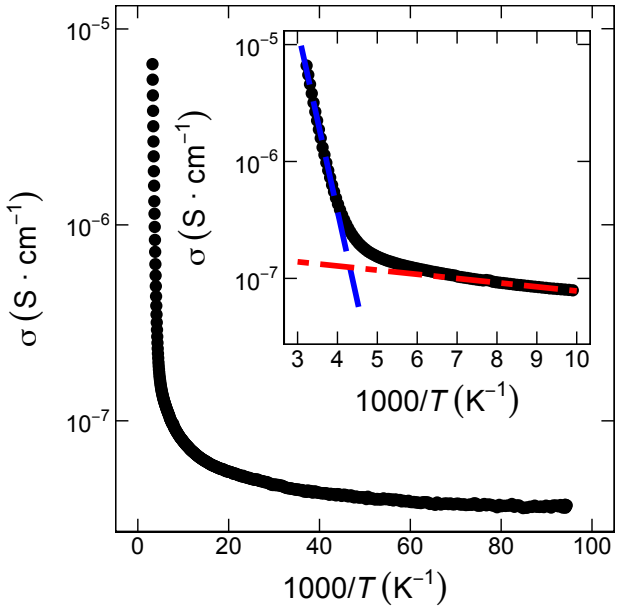

Figure 4. Temperature-dependent conductivity of a Nila-TiO_2lNi device in which the thickness of the a-TiO_2 layer was 68 nm. The inset shows the same data for the 100–310 K temperature range; the blue and red dashed lines are linear fits of the data for temperatures in the range of 250–310 and 100–125 K, respectively.

Potential-Dependent Conductivity of a-TiO_2 Devices

Figure 5 shows the dependence of conductivity on the gate potential (V_{gate}) for an a-TiO_2 film with Ti contacts in the EC-FET configuration in contact with 1.0 M H_2SO_4 (aq), which allowed the conductivity of TiO_2 to be measured as a function of the potential, or Fermi level, of the gate electrode. V_{gate} was referenced against a reversible hydrogen electrode (RHE) and was varied across a potential range relevant to water splitting (–0.4 to +1.75 V vs RHE). The data showed a sharp increase in conductivity as V_{gate} became more negative than –0.3 V versus RHE, indicating a sharp increase in electron transport in the conduction band. At these potentials, TiO_2 is in accumulation. At more positive potentials, the conductivity showed a weak dependence on V_{gate} and decreased by ~1% over a range of 2 V. These data suggest the presence of a finite density of states at potentials extending

for >2 eV below the TiO_2 conduction band edge. These results generally agree with the data for Sila-TiO_2 and Sila-TiO_2|Ni samples observed under electrochemical conditions in 1.0 M KOH (aq). Sila-TiO_2 showed a flat-band potential of –0.9 versus Ag/AgCl, that is, +0.1 V versus RHE, whereas the Sila-TiO_2|Ni sample showed Fermi level pinning over a broad potential range (0– 1.4 V vs RHE).[17,48]

The conductivity measured for a-TiO_2 using the IDE in 1.0 M H_2SO_4 (aq) was 1.17 $\pm$ 0.45 $\times$ 10^{-5} S cm^{-1}, with three samples measured (Table S3). Measurements made in air using one of the IDEs used in the EC-FET experiments showed a dry conductivity equal to that for the electrode in contact with the electrolyte, suggesting that the IDE electrode was unaffected by immersion in the electrolyte and indicating negligible electrolyte-induced effects on the conductivity.

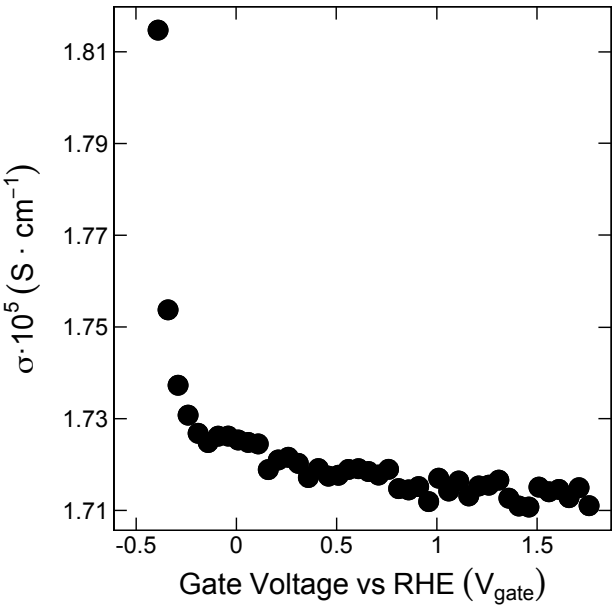

Figure 5. Conductivity of a-TiO_2 as a function of the gate voltage (V_{gate}) applied to interdigitated contacts covered by 1500 cycles (approximately 68 nm) of a-TiO_2.

2.4.3 Effects of ALD Process on the Physical Characteristics of ALD a-TiO_2

J–V Characteristics of p^+-Si|a-TiO_2|Ni Devices

Figure 6 shows the J–V characteristics of p^+-Si|a-TiO_2|Ni devices, with the a-TiO_2 films prepared via ALD using either a TDMAT precursor with the substrate held at 150 °C or a $TiCl_4$ precursor with the substrate held at 50, 100, or 150 °C. Films deposited from TDMAT at 150 °C or from $TiCl_4$ at 50 or 100 °C had undetectable levels of crystallinity, whereas small fractions of crystallinity were detected from films prepared at 150 °C, as measured by Raman spectroscopy (Figure S4a) and glancing incidence X-ray diffraction (Figure S4b).[49,50] In addition, the main phase of the films was probed by Fourier transform infrared spectroscopy. No evidence was found to support the presence of H_2TiO_3 in the films deposited on glass (Figure S5a) and Si (Figure S5b).

All of the TiO_2 devices exhibited Ohmic regions at low biases, however, for the same applied bias, the TDMAT–TiO_2 film passed more than an order of magnitude higher current density than the least resistive $TiCl_4$–TiO_2 film. The conductivities of the $TiCl_4$–TiO_2 films increased with the growth temperature. The mobilities of the various TiO_2 films were calculated according to eq 5, and the free-carrier concentrations were calculated using eq 6. The free-carrier concentrations for the $TiCl_4$–TiO_2 films were smaller by 1–3 orders of magnitude than that of the TDMAT film.

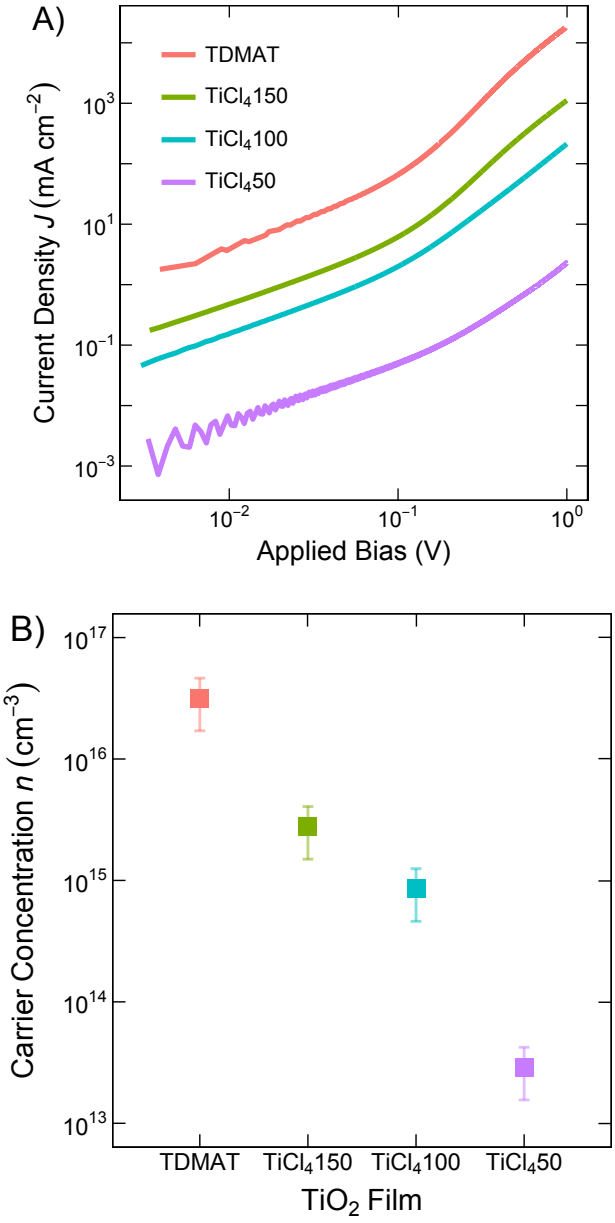

Figure 6. (a) J–V characteristics and (b) free-carrier concentrations calculated for various TiO_2 films grown on p^+-Si substrates and contacted with Ni. The film grown from TDMAT at 150 °C was ~68 nm thick; the films grown from $TiCl_4$ were ~60 nm thick and were grown at varied temperatures of 50, 100, or 150 °C.

Valence Band Spectra

Figure 7a shows the XPS valence band spectra for an a-TiO_2 film prepared by ALD using a TDMAT precursor at 150 °C. The observed signal was in accordance with the previously reported valence band spectra of identically prepared a-TiO_2.[4,18] After a Shirley background was subtracted, the spectra showed a peak centered at 1.07 ± 0.07 eV with a full width at half-maximum (fwhm) of 0.83 eV. Using the previously determined position of the Fermi level in TiO_2 as 0.40 eV below the conduction band minimum (CBM), the defect band was centered at 1.47 eV and extended from ~1 to 1.9 V below the CBM, that is, from ~0.6 to 1.5 eV below the Fermi level.[16] Previous analysis located the center of the defect band at ~1.34 eV below the CBM, with a fwhm of 0.83 eV, consistent with the results described herein.[16]

Figure 7b presents the valence band spectra of ALD-TiO_2 films prepared using different precursors and growth temperatures. All of the valence band spectra showed a peak at 1.07 ± 0.07 eV, with mutually similar fwhms. The TDMAT–TiO_2 film exhibited the largest valence band signal, whereas the $TiCl_4$–TiO_2 films exhibited weaker signals that increased with growth temperature. The relative peak intensities (normalized to the largest signal) were 0.62 ± 0.2, 0.69 ± 0.2, 0.71 ± 0.3, and 1 ± 0.6 for the $TiCl_4$–TiO_2 films grown at 50, 100, and 150 °C and TDMAT–TiO_2, respectively. The averaged spectra and the respective standard deviation can be seen in Figure S6.

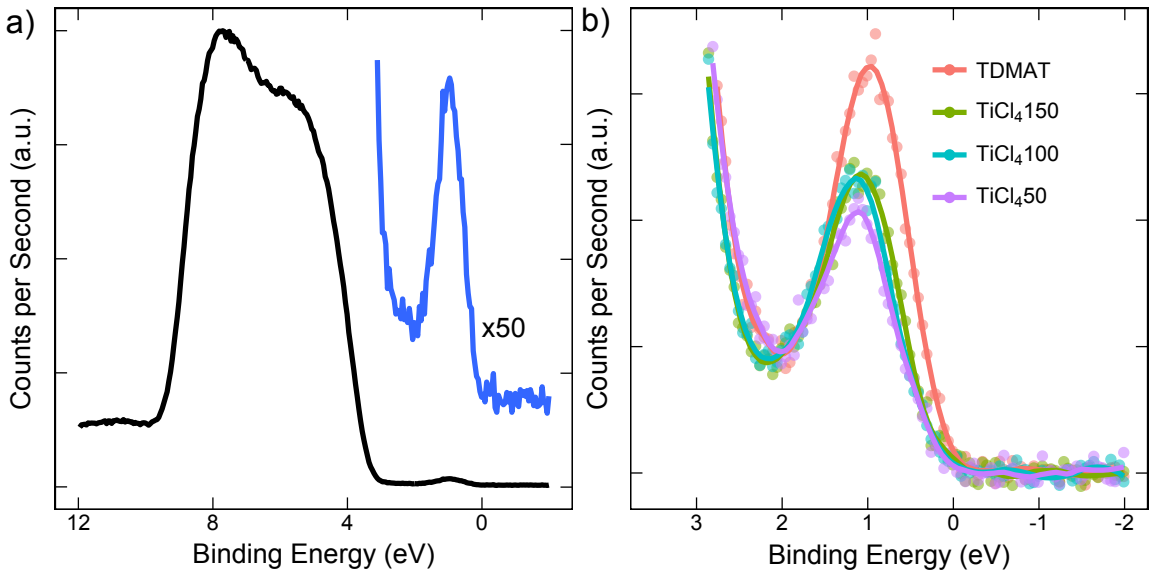

Figure 7. (a) X-ray photoemission spectra (without background subtraction) for the valence band of a-TiO_2 grown via ALD using a TDMAT precursor at 150 °C. (b) Comparison of the X-ray photoemission valence band spectra of ALD a-TiO_2 films grown using a TDMAT precursor at 150 °C or a $TiCl_4$ precursor at 50, 100, or 150 °C.

EPR Spectroscopy

Figure 8 compares the EPR spectra for the various ALD-TiO_2 films. The isotropic g-values extracted from the spectra were 1.939 and 2.000. The broad signal at 1.939 is consistent with the presence of Ti^{3+} as the signal is within the range of previously reported g-values, g = 1.92–2.00, for Ti^{3+} sites.[30,51–55] The TDMAT–TiO_2 films exhibited a substantially larger Ti^{3+} signal than the $TiCl_4$–TiO_2 films. The $TiCl_4$–TiO_2 films grown at 150 and 100 °C exhibited a detectible signal for Ti^{3+}, whereas $TiCl_4$–TiO_2 grown at 50 °C showed no appreciable Ti^{3+} signal.

The signal at 2.000 observed in the spectra for the 150 °C $TiCl_4$–TiO_2 film is attributable to either the variations of impurities within the glass substrate or electrons trapped at the oxygen vacancy sites.[26,56] The sharpness of the signal as

well as the appearance at g-values greater than the broad Ti^{3+} signal are consistent with the electrons trapped at the oxygen vacancy sites. Additional control experiments showed that only a decrease in the signal at this g-value was observed with the substrate-only and EPR silent Al_2O_3 signal, as can be seen in Figure S7a. The same decrease was present in all other TiO_2 films but was not observed in the background (cavity-only) signal, which had no prominent features.

In addition, EPR measurements were performed at various angles of rotation. No shift was observed when the TDMAT a-TiO_2 sample was rotated within the EPR instrument. This result is expected, as a-TiO_2 samples have an amorphous structure and the samples are macroscopically arranged randomly in the EPR tube. The results of the control experiments are presented in Figure S7b.

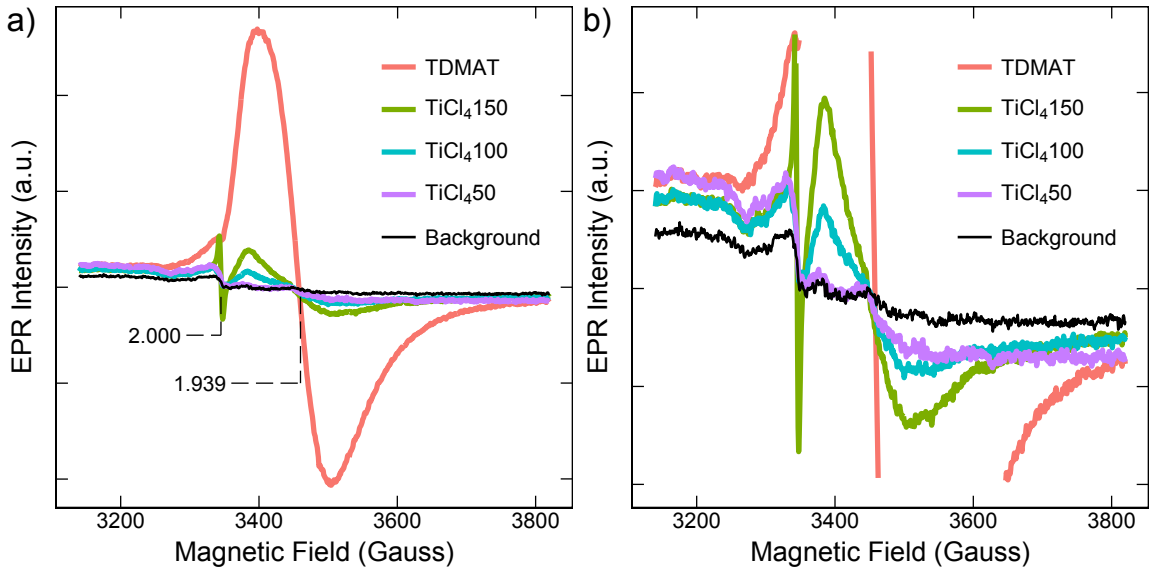

Figure 8. (a) EPR spectroscopy for a-TiO_2 films grown via ALD using a TDMAT precursor at 150 °C or a $TiCl_4$ precursor at 50, 100, or 150 °C. (b) EPR spectra rescaled to show the details of the smaller peaks. The background spectrum includes the EPR tube and the glass substrate.

2.4.4 Application to Photoelectrochemical Water Oxidation in Acidic Aqueous Electrolytes

Figure 9 shows the voltammetric behavior of non-photoactive p^+-Sila-TiO_2|Ir anodes and n-Sila-TiO_2|Ir photoanodes under 1 Sun illumination in 1.0 M H SO (aq). Ir was deposited on a-TiO_2 as catalytic islands 3 μm in diameter on a 7 μm pitch. The Ir islands were 35 nm-thick and were deposited either directly on a-TiO_2 or onto 35 nm of Ti on a-TiO_2. Ti was selected as an intermediate contact because p^+-Sila-TiO_2 devices with Ti contacts had exhibited high conduction relative to devices with Ir contacts. The samples with the Ti interconnect performed substantially better than those without the Ti interconnect, as evidenced by a reduction in the overpotential required to reach 10 mA cm^{-2} of current density of

280 mV for the TiIr n-Si devices and of 460 mV for the TiIr p^+-Si devices.

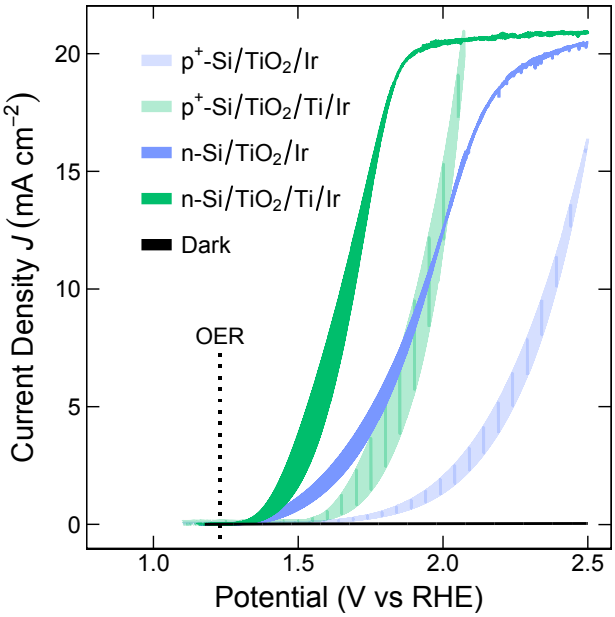

Figure 9. CV of non-photoactive p^+-Sila-TiO_2 anodes and n-Sila-TiO_2 photoanodes in contact with 1.0 M H_2SO_4. The samples were p^+-Si and n-Si substrates coated with 1500 ALD cycles of a-TiO_2 onto which metal-island top contacts were deposited. The metal top contacts to the a-TiO_2 layer were 35 nm-thick islands of Ir, 3 μm in diameter pitched 7 μm apart, deposited either directly on a-TiO_2 or onto a 35 nm-thick Ti island interconnect. The CV sweep was conducted in the dark and 1 Sun illumination for p^+-Si and n-Si, respectively, from 1.1 V vs RHE to 2.5 V vs RHE at a scan rate of 40 mV s^{-1}.

2.5 Discussion

2.5.1 Identity and Position of Defect States in ALD a-TiO_2

The valence band spectra for a-TiO_2 deposited via ALD showed a small peak within the band gap of TiO_2, centered at 0.94 eV below the Fermi level.[18,39] The band had a fwhm of 0.83 eV, indicating that a wide energy band exists within the band gap. Defect bands in TiO_2 have been observed both for amorphous films grown by ALD as well as for crystalline films grown by various methods.[57–63] The bands have been

associated with oxygen and/or other defects on the surface of the TiO_2. Oxygen vacancy sites are often implicated and have been observed by transmission electron microscopy (TEM).[58] The defect band has been correlated with the introduction of imperfections into the crystal.[47,64] Oxygen vacancies would provide doping and produce Ti^{3+} sites by the trapping of free electrons into localized Ti–O octahedra with an oxygen vacancy.[65] Theoretical calculations favor oxygen vacancies as the structural origin of the defect sites, and calculations moreover have been used to calculate conduction by small-polaron hopping.[47,66–69]

Oxygen defects and Ti^{3+} sites dominate the physical and chemical properties in TiO_2.[47,63–65,67,70–73] The bulk structure of reduced crystalline TiO_{2-x} contains defects of doubly charged oxygen vacancies, interstitial titanium defects, and other defects.[74] The defects vary with the amount of the oxygen deficiency,[23] and the vacancies on the surface were imaged by scanning tunneling microscopy.[74,75] The number of vacancies can be controlled by the method of annealing, and the surface vacancies can be healed by dosing with oxygen.[23] Additionally, self-doping of TiO_2 from oxygen vacancies yields Ti^{3+} sites.[28]

ALD TiO_2 grown at substrate temperatures <300 °C has been shown to be amorphous when annealed below 350 °C but becomes crystalline when annealed above 350 °C.[76,77] XPS studies of ALD a-TiO_2 have observed both a Ti^{3+} shoulder on the Ti 2p core level and a small shoulder on the O 1s spectra that is assigned to –OH groups on the surface.[61,62] Both normal and resonant valence band spectra show a peak at ~1 eV below the Fermi level that is due to titanium and attributable to Ti^{3+} states. The band is much weaker in crystalline TiO_2.[62]

XPS depth profiling was forgone because the Ti 2p XPS spectrum is heavily altered

after Ar-ion bombardment. Oxygen is preferentially removed thus reducing the TiO_2. The reduced states observed in the spectrum generated from the Ar-ion bombardment are thus not an accurate representation of the underlying composition of TiO_2.[78] Instead, we focused on angle-dependent XPS spectroscopy where, with increased electron emission angle Θ to the surface normal, the inelastic mean free path for electrons is reduced. The values for Al Kα radiation are given in Table S4.

The concentration of the defect states (and Ti^{3+} states) was investigated by angle-dependent XPS.[17] No change in the Ti 2p core level and the defect band was detected. However, with increasing surface sensitivity, a shoulder at 532.5 eV at the O 1s core level (attributed to dumbbell di-oxygen species, OH-groups, and/or to the reconstruction of TiO_2) was visible, which increased in intensity with increased Θ. Here, we performed scans for $\Theta = 0$ and 70 with an improved signal-to-noise ratio, which are shown in Figure S8. Again, no difference between the bulk or surface sensitive spectra could be observed, indicating no surface reoxidation of the defect band.

EPR spectra provided direct evidence of Ti^{3+} within the bulk a-TiO_2 films (Figure 8). The correlation between the strength of the Ti^{3+} signals in the EPR spectra and the strength of the defect band peaks in the XPS valence band spectra supports the assignment of the defect peak in the XPS valence band spectra to localized Ti^{3+} sites. The films are amorphous, so the Ti^{3+} sites can be expected to show a dispersion in energy because of the differences in Ti–Ti and Ti–O bond lengths,[79] consistent with the wide peak (fwhm = 0.83 eV) observed for the defect band.

The Ti^{3+} sites in the ALD a-TiO_2 films were however not directly detectable by XPS.[4,18] Hence, either the concentration of Ti^{3+} sites near the surface is below the

detection limit of XPS or such sites may not be present on the surface of air-exposed samples because of oxidation of Ti^{3+} in the presence of water and air.[4,30,53] The oxidation of surface Ti^{3+} sites would likely create a surface layer that is more resistive than the bulk of the film, consistent with the low conductance values measured when nonpenetrative, soft contacts (e.g., Hg droplet or liquid electrolyte contacts) were made to the ALD-TiO_2 films. Deposition of metal contacts by electron-beam evaporation or sputtering would thus allow low-resistance contacts to be made to the ALD-TiO_2,[4,16] consistent with expectations for penetration of a native resistive surface layer on these a-TiO_2 films.

The J–V behavior for p^+-Si|TiO_2|Ni devices formed with TiO_2 from varied ALD processes shows that conduction through films of ALD a-TiO_2 is not limited to films produced from TDMAT, although the conductivity of a-TiO_2 formed using TDMAT is greater than for films formed using $TiCl_4$. Increases in the conductivities of the films correlated with increases in the strengths of the EPR signals for Ti^{3+} as well as with increases in the amplitude of the defect peak in the valence band spectra. In combination, these data suggest that Ti^{3+} sites are important contributors to the conductivities of the films.

Previously, the high conductivities of TDMAT–TiO_2 films were hypothesized to directly arise from an increased density of C and N impurities.[4,18] The C and N impurities were measured for all films (TDMAT and 150, 100, and 50 °C $TiCl_4$ films) via SIMS, which revealed very similar concentrations of C and N impurities in all of the samples despite the large range in observed film conductivity. The C and N impurities thus appear to be independent of the precursor and preparation of the a-TiO_2 film, unlike the concentration of Ti^{3+} sites. The normalized SIMS spectra for C and N are displayed in Figure S9.

2.5.2 Conduction through the a-TiO_2 Bulk

Temperature-Dependent Conductivity

The temperature-dependent conductivity for temperatures >250 K of Nila-TiO_2|Ni layered stacks showed Arrhenius-type behavior, with an activation energy of 350 meV and a prefactor of ~4 S cm^{-1}. The observed activation energy suggests a Marcus-type of reorganization energy of 1.4 eV.[80] A transition was observed from Arrhenius-type behavior in the high-temperature limit (>250 K) to temperature-independent tunneling type behavior at low temperatures (<50 K). Similar behavior has been observed with NiO.[81] In addition, analogous behavior has also been observed for sputtered TiO_2 films, even though the sputtered TiO_2 films had 3–4 orders of magnitude higher conductivities than the a-TiO_2 films produced herein.[82,83] For crystalline rutile and anatase TiO_2, small-polaron or variable-range hopping between Ti^{3+} sites and adjacent Ti^{4+} sites is most commonly thought to be the primary conduction mechanism, and theory has been used to model small-polaron hopping in both crystalline and amorphous TiO_2.[47,57,69,84–86] Pham and Wang used DFT + U methods to calculate a reorganization energy of 1.14 eV for charge transfer between Ti^{3+} and Ti^{4+} sites in a-TiO_2, whereas Deskins and Dupuis used similar methods to estimate an activation energy of ~0.3 eV for polaron hopping in both rutile and anatase TiO_2.[47,72] Both estimates are consistent with the results reported herein.[47] Assuming that the density of Ti^{3+} sites is equal to the measured trap-site density (~10^{19} cm^{-3}) yields an average distance between Ti^{3+} sites of ~4 nm, whereas Ti–Ti distances in TiO_2 rutile or anatase crystals are 0.30–0.46 nm.[87,88]

Frequency-Dependent Conductivity

The ac conductivity of Nila-TiO_2|p^+-Si devices was constant (3.0×10^{-6} S cm^{-1}) for frequencies ≤10^5 Hz and increased rapidly for frequencies above 10^6 Hz. For charge transport within the conduction band or valence band of a semiconductor, the ac conductivity can be described by the Drude model,[44,89,90]

$$\sigma(\omega) = \frac{\sigma_0}{1 + \omega^2\tau^2} \qquad (7)$$

where σ_0 is the dc conductivity, ω is the ac radial frequency, and τ is the relaxation time. This model predicts a decrease in conductivity with increases in the ac frequency and hence is not consistent with the behavior reported herein.

For charge transport via hopping, isolated hopping sites do not contribute to the dc conductivity. However, as the frequency increases, these isolated hopping sites increasingly contribute to the ac conductivity. The frequency dependence of the conductivity in a wide variety of disordered materials obeys a power law[91–94] and can be written as

$$\sigma(\omega) = A\omega^s + \sigma_{DC} \qquad (8)$$

where A is a constant, ω is the angular frequency, s is the exponent of the angular frequency, and σ_{dc} is the dc conductivity.[40] The data reported herein are consistent with this model, and a fit of the data to eq 8 yielded $\sigma_{dc} = 2.99 \times 10^{-6}$ S cm^{-1}, A = 9.9×10^{-17} S cm^{-1} $s^{1.95}$, and s = 1.95 (Figure 3).

Potential-Dependent Conductivity

The potential-dependent conductivity measured by the EC-FET experiments showed only a 1% decrease in conductivity as the potential of the gate was moved

positively toward the valence band of TiO_2. If conduction across a-TiO_2 relied upon electrons tunneling into the TiO_2 conduction band through a shallow space-charge region at the interface, then the EC-FET experiments would be expected to exhibit a strong dependence of the conductivity on the gate voltage. Specifically, a sharp decrease in conductivity would be observed at potentials positive of the conduction band of a-TiO_2. The results are thus not consistent with conduction via tunneling of electrons into the conduction band of a-TiO_2.

The TiO_2 conductivity at positive potentials is sufficient to support faradaic current densities in the range of 10 mA cm^{-2} without substantially affecting the OER overpotential. As illustrated in Figure S10, for a-TiO_2 conductivities of ~10^{-5} S cm, the potential drop across the p^+-Si|a-TiO_2|Ni interface is smaller than the potential drop at the a-TiO_2|Ni|electrolyte interface. The simulation also shows that decreasing conductivity will affect the transport properties across the protecting layer, thus increasing the OER overpotential.

2.5.3 Conduction across a-TiO_2 Interface with Varied Metal Contacts

Contacts between a-TiO_2 and Ti (ϕ = 4.3 ± 0.2 eV) or Mg (ϕ = 3.7 ± 0.2 eV), which have smaller work functions than that of a-TiO_2 (ϕ = 4.7 eV) and have mutually similar V_{FB} values, exhibited mutually similar J–V characteristics (Figure 1). Contacts between a-TiO_2 and Au (ϕ = 5.1 ± 0.30 eV), Pd(ϕ = 5.3 ± 0.2 eV), Ir(ϕ = 5.3 ± 0.2 eV), or Pt (ϕ = 5.6 ± 0.07 eV), which have work functions greater than that of a-TiO_2, passed ≤10% of the current densities of devices that have low-work-function top contacts. The contact between a-TiO_2 and Ni (ϕ = 5.1 ± 0.4 eV) was a notable exception, exhibiting J–V characteristics similar to those with low-work-function metals but with a work function similar to the aforementioned high-work-

function contacts. Contacts to low-work-function metals moreover showed less resistance than contacts to high-work-function metals.

Some differences in the J–V behavior among devices with high-work-function contacts were evident; specifically, at biases <100 mV, devices with Pd contacts passed only ~10% of the current passed by devices with Au contacts. In the decreasing order, devices with Au, Ir, Pt, and Pd top contacts exhibited a reduction in current that matched (except for Pd) the order in which the work functions of the metal contacts increase (Au, Pd, Ir, and Pt).

The work functions for the various clean metals were measured by UPS under high-vacuum conditions, whereas the conduction was measured for the e-beam-deposited metal in contact with the TiO_2 substrate. Polycrystalline metals have multiple crystal faces exposed, so the measurements give an average over the various crystal faces. The averaging is expected to be different depending on the phenomenaused. Also, the fraction of each exposed face may not be the same for the clean metal compared to that of the metal sputtered onto a TiO_2 surface. Thus, only a rough correlation is expected between the work functions measured by UPS and the measured J–V behavior.

SCLC spectroscopy was used to determine the mobility and trap density in the TDMAT a-TiO_2 films. The trap density and mobility were found for Au, Ir, Pt, and Pd as well as for Ir, Pt, and Pd. As can be seen in Figure 2b and Table S2, the trap density and mobility were found to be 1×10^{19} cm^{-3} and $6.5 \pm 3 \times 10^{-4}$ cm^2 V^{-1} s^{-1}, respectively, and essentially independent of the top contact. The mobility value used was assumed to be independent of the top contact's work function and was thus used to determine the effective carrier concentration for all of the top contacts. The effective carrier concentration found using this mobility value is in agreement with

the carrier concentration observed when measuring the carrier concentration by the Hall effect with In contacts (Figure 2c). In addition, the mobility measured is in agreement with the predicted mobility found by DFT + U methods of 2×10^{-4} cm^2 V^{-1} s^{-1} by Pham and Wang.[47]

Devices with a top contact less than ~5.2 eV had the (effective) free-carrier concentration of the device independent of the work function. Greater than ~5.2 eV, the devices' (effective) free-carrier concentration decreases by 10^1 to 10^2 cm^{-3} and is dependent on the work function. The former devices with contacts to metals that have work functions less than the work function of a-TiO_2 had the (effective) free-carrier concentrations on the order of 10^{16} cm^{-3}. Conversely, the effective free-carrier concentrations in a-TiO_2 for devices with contacts greater than the work function of a-TiO_2 were ~10^{14} to 10^{15} cm^{-3}, again with the exception of Ni, which showed free-carrier concentrations similar to those measured for contacts with the low-work-function metals.

The dependence on the work function can consistently be ascribed to band-bending in TiO_2 induced by the respective top contact. Metals with a work function greater than the Fermi level of a-TiO_2 bend the defect band away from the Fermi level, which will not change the occupancy of the defect band. Conversely, metals with a work function less than the Fermi level of a-TiO_2 will cause the defect band to bend toward and even above the Fermi level. With states above the Fermi level, mobile charge carriers (electrons) will empty these states, thus converting Ti^{3+} into Ti^{4+}.

These free-carrier concentrations are an effective average for a-TiO_2 because the depletion width can extend through roughly half the thickness of the film. The conductivity of a-TiO_2 correlates with the Ti^{3+} concentration in the a-TiO_2 films, so

any local change to the Ti^{3+} concentration will affect the conductivity of a-TiO_2.

Conduction through the defect band can occur by hopping between sites (e.g., Ti^{4+}/Ti^{3+}). If defect sites exist above the Fermi level of the system, then those sites would have fewer free electrons that can hop between sites, and hence conduction is expected to be less favorable in that part of the band.

The J–V behavior of the films with different metal contacts is consistent with an equilibration process between a-TiO_2 and the metal contact in conjunction with Fermi level pinning in TiO_2. During equilibration, low-work-function metal (e.g., Mg, Ti) contacts inject electrons into a-TiO_2, whereas high-work-function contacts extract electrons from a-TiO_2. In this process, most of the electrons would be expected to come from, or enter, the near-surface states of the TiO_2 defect band that are responsible for the Fermi level pinning; thus, the number of Ti^{3+} sites close to the surface remain the same or decrease.

The very low work functions of Mg and Ti suggest that TiO_2 is forced into accumulation, primarily producing charge mostly on or near the surface, as opposed to substantial band bending. The Ti^{3+} defect sites would thus be available for conduction through TiO_2. Alternatively, the noble metals, with high work functions, are expected to remove electrons from the near-surface states and thus reduce the numbers of Ti^{3+} sites close to the surface.[16,42] This process would produce bending of the defect band, and Ti^{3+} sites at higher energy than the Fermi level would be lost, thus decreasing conduction through that part of the band. The near-surface states would be more affected, resulting in relatively few Ti^{3+} sites on the surface and thus forming a barrier to conduction between TiO_2 and the metal.

Attempts have been made to observe the “draining” of the defect band by both EPR

and valence band spectra. The density of states for any deposited metal would overlap and quickly overpower the Ti^{3+} signal for the valence band spectra, even for <1 nm of the deposited metal. The analogous experiment for EPR was attempted using <10 nm of the deposited metal. However, the small amount of metal was so strongly absorbing of the incoming microwaves that the instrument could not be tuned to collect the spectrum.

This simple band-bending picture does not fully explain the observations regarding changes in the measured a-TiO_2 film conductivity with different metal contacts. The work function of Ni (5.1 ± 0.4 eV) is greater than that of a-TiO_2 (4.7 eV) and closer to that of Au (5.1 ± 0.3 eV) than to Ti or Mg (≤4.3 eV). Furthermore, the data support a wide dispersion in energy (~0.8 eV) for the defect band associated with Ti^{3+} states, which would allow a substantial density of defect states to remain below the a-TiO_2 Fermi level, for all high-work-function contacts examined herein. However, after subtraction of a Shirley-type background, the defect band peak was fitted with a Gauss–Lorentz peak profile with a 40% Gaussian contribution and a 60% Lorentzian contribution. The obtained peak broadening of ~0.8 eV can thus be split into 0.32 eV instrumental broadening (Gaussian) and 0.48 eV intrinsic lifetime broadening (Lorentzian).

Differences in chemical reactivity might also contribute to the observed differences in behavior of the metal contacts; specifically, noble metals (Au, Ir, Pt, and Pd) showed lower conduction across interfaces with a-TiO_2 than non-noble metals (Mg, In, Ti, and Ni). Thus, the contact interface between the metal and TiO_2 may also play a role in providing low-resistance contacts. Ir, an active catalyst of the OER in acidic electrolytes, does not form a highly conductive contact to a-TiO_2; however, deposition of an acid-stable metal (Ti) that does form a highly conductive contact

to a-TiO_2 prior to deposition of the Ir catalyst allowed beneficial integration of the Ir catalyst with the a-TiO_2 coating, yielding photoanodes that exhibit high fill factors for water oxidation in 1.0 M H_2SO_4 (aq).

In the expected behavior of Ni when comparing its work function to the work function of a-TiO_2, it has been shown that the interface is not the source of discrepancy. The Si|TiO_2|Ni| electrolyte interface has been probed via AP-XPS.[17,48] It has been shown that for ultrathin layers of Ni (<1 nm), no conduction was observed in $Fe(CN)_6^{3-/4-}$ (aq) and 1.0 M KOH (aq). Conductivity and OER performance were observed and greatly increased for $d_{Ni} > 1$ nm. For thin Ni layers under oxidative conditions, only oxidized Ni phases are expected (NiO_x, NiOOH is the catalyst phase, and under the OER conditions at pH 14, no metallic Ni can exist). However, small amounts of metallic Ni phases for $d_{Ni} > 0.6$ nm were observed [using AP-XPS under potential control in 1.0 M KOH (aq)], which increased in intensity for increased deposition of Ni. This behavior led to the proposed picture of a TiO_2|Ni|NiO_x structure under OER, analogous to the structure of a TiO_2|Ti interface.[48] Separate ex situ ultrahigh vacuum measurements using different excitation energies and varying the electron emission angle confirmed the presence of a metallic Ni phase below the surface. In addition, cross-sectional TEM and scanning electron microscopy images of the TiO_2|Ni interface region further support the presence of metallic Ni at the interface of TDMAT a-TiO_2.[4,18]

The reason for Ni's divergence from the expected behavior is attributed to its work function. Although the work function of Ni is more positive than that of a-TiO_2, it is not sufficiently positive enough to cause a significant reduction of Ti^{3+} concentration at the interface but rather a slight reduction of the concentration at the interface because of the broad width of the Ti^{3+} defect band.

2.6 Conclusions

a-TiO_2 films deposited via ALD contained a broad (~0.8 eV) defect band between the TiO_2 Fermi level and the TiO_2 valence band. For ALD TiO_2 films deposited under varied conditions and using varied precursors, the size of the defect band correlated with both the bulk conductivity of the a-TiO_2 films and the Ti^{3+} concentration observed via EPR spectroscopy. In combination with a variety of solid-state measurements, including temperature-dependent conductivity, the data show that conduction through the bulk TiO_2 films is consistent with the hopping mechanism between Ti^{3+} and adjacent Ti^{4+} sites as opposed to conduction via the conduction or valence bands. The wide defect band associated with Ti^{3+} sites spans an energy level comparable to the valence bands of light-absorbing semiconductors such as Si. Thus, allowing anodic conduction across that would otherwise present a ~2 eV barrier to anodic conduction.

The conduction across interfaces between metal contacts and a-TiO_2 films depended on the metal. For the metals examined, interfaces with metals having work functions less than that of a-TiO_2 generally provided higher conductivities than interfaces with metals having work functions greater than that of a-TiO_2. These observations are mostly consistent with $Ti^{3+/4+}$ conduction that makes use of defect sites close to the surface both to reduce the band bending in the bulk of TiO_2 and to provide either an insulating or conducting interface between TiO_2 and the metal. Thus, for metals with a low work function, a low resistance path is provided by Ti^{3+} sites, whereas for high-work-function metals, the Ti^{3+} sites are depleted and the resistance consequently increases. Ni, while having a relatively high work function, acts like a low-work-function metal and thus constitutes a notable exception. Properties of the metal contact other than the work function may thus contribute to the different

conductivities of interfaces with a-TiO_2. The observations provide guidance for a synergistic choice for contacts to a-TiO_2 films, showing that improved performance can be obtained for sunlight-driven water oxidation using an n-Sila-TiO_2 photoanode integrated with an Ir catalyst when a Ti interconnect is inserted between a-TiO_2 and the Ir catalyst relative to the situation in which the Ir catalyst is deposited directly onto a-TiO_2.

2.7 Acknowledgements

This work was supported through the Office of Science of the U.S. Department of Energy (DOE) under award no. DE-SC0004993 to the Joint Center for Artificial Photosynthesis, a DOE Energy Innovation Hub. P.D.N. and C.W.R. thank the National Science Foundation for graduate research fellowships. C.W.R. also thanks the Link Energy Foundation for a graduate research fellowship. Research was in part carried out at the Molecular Materials Resource Center of the Beckman Institute and at the Microanalysis Center of the California Institute of Technology. D.J.F. acknowledges the financial support by the UK Engineering and Physical Sciences Research Council through the PVTEAM programme (EP/L017792/1). We thank Dr. Y. Guan for SIMS measurements, Dr. Angelo Di Bilio and Dr. Paul H. Oyala for EPR measurements, and K. Papadantonakis for assistance with editing this manuscript. S.H. and S.J.K. acknowledge the start-up support from the Tomkat Foundation.

2.8 References

1. Pourbaix, M., *Atlas of Electrochemical Equilibria in Aqueous Solutions*, Second Edition ed.; National Association of Corrosion, 1974.

2. Lewis, N. S., Developing a Scalable Artificial Photosynthesis Technology Through Nanomaterials by Design. *Nat. Nanotechnol.* **2016**, *11*, 1010-1019.

3. Haussener, S.; Hu, S.; Xiang, C.; Weber, A. Z.; Lewis, N. S., Simulations of the Irradiation and Temperature Dependence of the Efficiency of Tandem Photoelectrochemical Water-Splitting Systems. *Energy Environ. Sci.* **2013**, *6*, 3605.
4. Hu, S.; Shaner, M. R.; Beardslee, J. A.; Lichterman, M.; Brunschwig, B. S.; Lewis, N. S., Amorphous TiO_2 Coatings Stabilize Si, GaAs, and GaP Photoanodes for Efficient Water Oxidation. *Science* **2014**, *344*, 1005-1009.
5. Shaner, M. R.; Hu, S.; Sun, K.; Lewis, N. S., Stabilization of Si Microwire Arrays for Solar-Driven H_2O Oxidation to O_2(g) in 1.0 M KOH(aq) Using Conformal Coatings of Amorphous TiO_2. *Energy Environ. Sci.* **2015**, *8*, 203-207.
6. Sun, K.; McDowell, M. T.; Nielander, A. C.; Hu, S.; Shaner, M. R.; Yang, F.; Brunschwig, B. S.; Lewis, N. S., Stable Solar-Driven Water Oxidation to O_2(g) by Ni-Oxide Coated Silicon Photoanodes. *J. Phys. Chem. Lett.* **2015**, *6*, 592-598.
7. Chen, Y. W.; Prange, J. D.; Dühnen, S.; Park, Y.; Gunji, M.; Chidsey, C. E. D.; McIntyre, P. C., Atomic Layer-Deposited Tunnel Oxide Stabilizes Silicon Photoanodes for Water Oxidation. *Nat. Mater.* **2011**, *10*, 539-544.
8. Kainthla, R. C.; Zelenay, B.; Bockris, J. O. M., Protection of n-Si Photoanode Against Photocorrosion in Photoelectrochemical Cell for Water Electrolysis. *J. Electrochem. Soc.* **1986**, *133*, 248-253.
9. Kenney, M. J.; Gong, M.; Li, Y.; Wu, J. Z.; Feng, J.; Lanza, M.; Dai, H., High-Performance Silicon Photoanodes Passivated with Ultrathin Nickel Films for Water Oxidation. *Science* **2013**, *342*, 836-840.
10. Mei, B.; Seger, B.; Pedersen, T.; Malizia, M.; Hansen, O.; Chorkendorff, I.; Vesborg, P. C. K., Protection of p^+-n-Si Photoanodes by Sputter-Deposited Ir/IrO_x Thin Films. *J. Phys. Chem. Lett.* **2014**, *5*, 1948-1952.

11. Yang, J., et al., Efficient and Sustained Photoelectrochemical Water Oxidation by Cobalt Oxide/Silicon Photoanodes with Nanotextured Interfaces. *J. Am. Chem. Soc.* **2014**, *136*, 6191-4.
12. Zhou, X.; Liu, R.; Sun, K.; Papadantonakis, K. M.; Brunschwig, B. S.; Lewis, N. S., 570 mV Photovoltage, Stabilized n-Si/CoO_x Heterojunction Photoanodes Fabricated Using Atomic Layer Deposition. *Energy Environ. Sci.* **2016**, *9*, 892-897.
13. McDowell, M. T.; Lichterman, M. F.; Spurgeon, J. M.; Hu, S.; Sharp, I. D.; Lewis, N. S., Improved Stability of Polycrystalline Bismuth Vanadate Photoanodes by Use of Dual-Layer Thin TiO_2/Ni Coatings. *J. Phys. Chem. C* **2014**, *118*, 19618-19624.
14. Lichterman, M. F.; Carim, A. I.; McDowell, M. T.; Hu, S.; Gray, H. B.; Brunschwig, B. S.; Lewis, N. S., Stabilization of n-Cadmium Telluride Photoanodes for Water Oxidation to O_2(g) in Aqueous Alkaline Electrolytes Using Amorphous TiO_2 Films Formed by Atomic-Layer Deposition. *Energy Environ. Sci.* **2014**, *7*, 3334-3337.
15. Kohl, P. A.; Frank, S. N.; Bard, A. J., Semiconductor Electrodes XI. Behavior of n- and p-Type Single-Crystal Semiconductors Covered with Thin Normal-TiO_2 Films. *J. Electrochem. Soc.* **1977**, *124*, 225-229.
16. Hu, S.; Richter, M. H.; Lichterman, M. F.; Beardslee, J.; Mayer, T.; Brunschwig, B. S.; Lewis, N. S., Electrical, Photoelectrochemical, and Photoelectron Spectroscopic Investigation of the Interfacial Transport and Energetics of Amorphous TiO_2/Si Heterojunctions. *J. Phys. Chem. C* **2016**, *120*, 3117-3129.
17. Lichterman, M. F., et al., Direct Observation of the Energetics at a Semiconductor/Liquid Junction by Operando X-Ray Photoelectron Spectroscopy. *Energy Environ. Sci.* **2015**, *8*, 2409-2416.

18. McDowell, M. T.; Lichterman, M. F.; Carim, A. I.; Liu, R.; Hu, S.; Brunschwig, B. S.; Lewis, N. S., The Influence of Structure and Processing on the Behavior of TiO_2 Protective Layers for Stabilization of n-Si/TiO_2/Ni Photoanodes for Water Oxidation. *ACS Appl. Mater. Interfaces* **2015**, *7*, 15189-15199.
19. Bae, D.; Shayestehaminzadeh, S.; Thorsteinsson, E. B.; Pedersen, T.; Hansen, O.; Seger, B.; Vesborg, P. C. K.; Ólafsson, S.; Chorkendorff, I., Protection of Si Photocathode Using TiO_2 Deposited by High Power Impulse Magnetron Sputtering for H_2 Evolution in Alkaline Media. *Sol. Energy Mater. Sol. Cells* **2016**, *144*, 758- 765.
20. Seger, B.; Pedersen, T.; Laursen, A. B.; Vesborg, P. C.; Hansen, O.; Chorkendorff, I., Using TiO_2 as a Conductive Protective Layer for Photocathodic H_2 Evolution. *J. Am. Chem. Soc.* **2013**, *135*, 1057-1064.
21. Seger, B.; Tilley, D. S.; Pedersen, T.; Vesborg, P. C. K.; Hansen, O.; Grätzel, M.; Chorkendorff, I., Silicon Protected with Atomic Layer Deposited TiO_2: Durability Studies of Photocathodic H_2 Evolution. *RSC Adv.* **2013**, *3*, 25902.
22. Mei, B.; Pedersen, T.; Malacrida, P.; Bae, D.; Frydendal, R.; Hansen, O.; Vesborg, P. C.; Seger, B.; Chorkendorff, I., Crystalline TiO_2: A Generic and Effective Electron-Conducting Protection Layer for Photoanodes and Cathodes. *J. Phys. Chem. C* **2015**, *119*, 15019-15027.
23. Li, M.; Hebenstreit, W.; Diebold, U.; Tyryshkin, A. M.; Bowman, M. K.; Dunham, G. G.; Henderson, M. A., The Influence of the Bulk Reduction State on the Surface Structure and Morphology of Rutile TiO_2(110) Single Crystals. *The Journal of Physical Chemistry B* **2000**, *104*, 4944-4950.
24. Su, J.; Zou, X.-X.; Zou, Y.-C.; Li, G.-D.; Wang, P.-P.; Chen, J.-S., Porous Titania with Heavily Self-Doped Ti^{3+} for Specific Sensing of CO at Room Temperature. *Inorg Chem* **2013**, *52*, 5924-5930.

25. Khomenko, V.; Langer, K.; Rager, H.; Fett, A., Electronic Absorption by Ti^{3+} Ions and Electron Delocalization in Synthetic Blue Rutile. *Phys Chem Miner* **1998**, *25*, 338-346.
26. Amano, F.; Nakata, M.; Yamamoto, A.; Tanaka, T., Effect of Ti^{3+} Ions and Conduction Band Electrons on Photocatalytic and Photoelectrochemical Activity of Rutile Titania for Water Oxidation. *J. Phys. Chem. C* **2016**, *120*, 6467-6474.
27. Chen, X.; Liu, L.; Peter, Y. Y.; Mao, S. S., Increasing Solar Absorption for Photocatalysis with Black Hydrogenated Titanium Dioxide Nanocrystals. *Science* **2011**, *331*, 746-750.
28. Zuo, F.; Wang, L.; Wu, T.; Zhang, Z.; Borchardt, D.; Feng, P., Self-Doped Ti^{3+} Enhanced Photocatalyst for Hydrogen Production Under Visible Light. *J. Am. Chem. Soc.* **2010**, *132*, 11856-11857.
29. Xing, M.; Fang, W.; Nasir, M.; Ma, Y.; Zhang, J.; Anpo, M., Self-Doped Ti^{3+}-Enhanced TiO_2 Nanoparticles with a High-Performance Photocatalysis. *J. Catal.* **2013**, *297*, 236-243.
30. Hoang, S.; Berglund, S. P.; Hahn, N. T.; Bard, A. J.; Mullins, C. B., Enhancing Visible Light Photo-oxidation of Water with TiO_2 Nanowire Arrays via Cotreatment with H_2 and NH_3: Synergistic Effects Between Ti^{3+} and N. *J. Am. Chem. Soc.* **2012**, *134*, 3659-3662.
31. Verlage, E.; Hu, S.; Liu, R.; Jones, R. J. R.; Sun, K.; Xiang, C.; Lewis, N. S.; Atwater, H. A., A Monolithically Integrated, Intrinsically Safe, 10% Efficient, Solar-Driven Water-Splitting System Based on Active, Stable Earth-Abundant Electrocatalysts in Conjunction with Tandem III–V Light Absorbers Protected by Amorphous TiO_2 Films. *Energy Environ. Sci.* **2015**, *8*, 3166-3172.
32. Piercy, B. D.; Losego, M. D., Tree-Based Control Software for Multilevel Sequencing in Thin Film Deposition Applications. *J. Vac. Sci. Technol. B.* **2015**, *33*, 043201.

33. Plana, D.; Humphrey, J.; Bradley, K.; Celorrio, V.; Fermín, D., Charge Transport Across High Surface Area Metal/Diamond Nanostructured Composites. *ACS Appl. Mater. Interfaces* **2013**, *5*, 2985-2990.

34. Roest, A.; Kelly, J.; Vanmaekelbergh, D.; Meulenkamp, E., Staircase in the Electron Mobility of a ZnO Quantum Dot Assembly Due to Shell Filling. *Phys. Rev. Lett.* **2002**, *89*, 036801.

35. Olthuis, W.; Streekstra, W.; Bergveld, P., Theoretical and Experimental-Determination of Cell Constants of Planar-Interdigitated Electrolyte Conductivity Sensors. *Sens. Actuators, B* **1995**, *24*, 252-256.

36. Michaelson, H. B., The Work Function of the Elements and Its Periodicity. *J. Appl. Phys.* **1977**, *48*, 4729-4733.

37. Hofmann, T.; Yu, T. H.; Folse, M.; Weinhardt, L.; Bar, M.; Zhang, Y. F.; Merinov, B. V.; Myers, D. J.; Goddard, W. A.; Heske, C., Reply to "Comment on 'Using Photoelectron Spectroscopy and Quantum Mechanics to Determine d-Band Energies of Metals for Catalytic Applications'". *Journal of Physical Chemistry C* **2013**, *117*, 6916-6917.

38. Hofmann, T.; Yu, T. H.; Folse, M.; Weinhardt, L.; Bar, M.; Zhang, Y. F.; Merinov, B. V.; Myers, D. J.; Goddard, W. A.; Heske, C., Using Photoelectron Spectroscopy and Quantum Mechanics to Determine d-Band Energies of Metals for Catalytic Applications. *Journal of Physical Chemistry C* **2012**, *116*, 24016-24026.

39. Chiu, F. C., A Review on Conduction Mechanisms in Dielectric Films. *Adv. Mater. Sci. Eng.* **2014**.

40. Bottger, H.; Bryksin, V. V., *Hopping Conduction in Solids*; Akademie-Verlag Berlin, 1985.

41. Rose, A., Space-Charge-Limited Currents in Solids. *Phys. Rev.* **1955**, *97*, 1538.

42. Tredgold, R. H., *Space Charge Conduction in Solids*; Elsevier Pub. Co., 1966.

43. Kim, S.; Jeong, H. Y.; Choi, S. Y.; Choi, Y. K., Comprehensive Modeling of Resistive Switching in the Al/TiO_x/TiO_2/Al Heterostructure Based on Space-Charge-Limited Conduction. *Appl. Phys. Lett.* **2010**, *97*.
44. Kao, K.-C.; Hwang, W., *Electrical Transport in Solids: with Particular Reference to Organic Semiconductors*
, 1st ed.; Pergamon Press: Oxford ; New York, 1981.
45. Riviere, J., Work Function: Measurements and Results. In *Solid State Surface Science*, Green, M., Ed. Decker: New York, 1969; Vol. 1, pp 179–289.
46. Hölzl, J.; Schulte, F. K., Work Function of Metals. In *Solid Surface Physics*, Höhler, G., Ed. Springer-Verlag: Berlin, 1979; pp 1-150.
47. Pham, H. H.; Wang, L. W., Oxygen Vacancy and Hole Conduction in Amorphous TiO_2. *Phys. Chem. Chem. Phys.* **2015**, *17*, 541-550.
48. Lichterman, M. F., et al., An Electrochemical, Microtopographical and Ambient Pressure X-Ray Photoelectron Spectroscopic Investigation of Si/TiO_2/Ni/Electrolyte Interfaces. *J. Electrochem. Soc.* **2016**, *163*, H139 - H146.
49. Niilisk, A.; Moppel, M.; Pärs, M.; Sildos, I.; Jantson, T.; Avarmaa, T.; Jaaniso, R.; Aarik, J., Structural Study of TiO_2 Thin Films by Micro-Raman Spectroscopy. *Open Physics* **2006**, *4*, 105-116.
50. Piercy, B. D.; Leng, C. Z.; Losego, M. D., Variation in the Density, Optical Polarizabilities, and Crystallinity of TiO_2 Thin Films Deposited Via Atomic Layer Deposition From 38 to 150° C Using the Titanium Tetrachloride-Water Reaction. *J. Vac. Sci. Technol., A* **2017**, *35*, 03E107.
51. Suriye, K.; Jongsomjit, B.; Satayaprasert, C.; Praserthdam, P., Surface Defect (Ti^{3+}) Controlling in the First Step on the Anatase TiO_2 Nanocrystal by Using Sol-Gel Technique. *Appl. Surf. Sci.* **2008**, *255*, 2759-2766.

52. Suriye, K.; Praserthdam, P.; Jongsomjit, B., Impact of Ti^{3+} Present in Titania on Characteristics and Catalytic Properties of the Co/TiO_2 Catalyst. *Ind. Eng. Chem. Res.* **2005**, *44*, 6599-6604.

53. Howe, R. F.; Gratzel, M., EPR Observation of Trapped Electrons in Colloidal Titanium Dioxide. *J. Phys. Chem.* **1985**, *89*, 4495-4499.

54. Reddy, S. L.; Reddy, G. S.; Endo, T., *Electronic (Absorption) Spectra of 3d Transition Metal Complexes*; INTECH, 2012.

55. Fu, G.; Zhou, P.; Zhao, M. M.; Zhu, W. D.; Yan, S. C.; Yu, T.; Zou, Z. G., Carbon Coating Stabilized Ti^{3+}-Doped TiO_2 for Photocatalytic Hydrogen Generation Under Visible Light Irradiation. *Dalton Trans.* **2015**, *44*, 12812-12817.

56. Liu, H.; Ma, H.; Li, X.; Li, W.; Wu, M.; Bao, X., The Enhancement of TiO_2 Photocatalytic Activity by Hydrogen Thermal Treatment. *Chemosphere* **2003**, *50*, 39-46.

57. Yildiz, A.; Iacomi, F.; Mardare, D., Polaron Transport in TiO_2 Thin Films. *J. Appl. Phys.* **2010**, *108*, 083701.

58. Wendt, S.; Sprunger, P. T.; Lira, E.; Madsen, G. K.; Li, Z.; Hansen, J. Ø.; Matthiesen, J.; Blekinge-Rasmussen, A.; Lægsgaard, E.; Hammer, B., The Role of Interstitial Sites in the Ti3d Defect State in the Band Gap of Titania. *Science* **2008**, *320*, 1755-1759.

59. Schierbaum, K.-D.; Fischer, S.; Wincott, P.; Hardman, P.; Dhanak, V.; Jones, G.; Thornton, G., Electronic Structure of Pt Overlayers on (1×3) Reconstructed TiO_2 (100) Surfaces. *Surf. Sci.* **1997**, *391*, 196-203.

60. Linderälv, C.; Lindman, A.; Erhart, P., A Unifying Perspective on Oxygen Vacancies in Wide Band Gap Oxides. *J. Phys. Chem. Lett.* **2018**, *9*, 222-228.

61. Henkel, K.; Das, C.; Kot, M.; Schmeißer, D.; Naumann, F.; Kärkkänen, I.; Gargouri, H., In-Gap States in Titanium Dioxide and Oxynitride Atomic Layer Deposited Films. *J. Vac. Sci. Technol., A* **2017**, *35*, 01B135.

62. Das, C.; Richter, M.; Tallarida, M.; Schmeißer, D., Electronic Properties of Atomic Layer Deposition Films, Anatase and Rutile TiO_2 Studied by Resonant Photoemission Spectroscopy. *J. Phys. D: Appl. Phys.* **2016**, *49*, 275304.

63. Park, S.-J.; Lee, J.-P.; Jang, J. S.; Rhu, H.; Yu, H.; You, B. Y.; Kim, C. S.; Kim, K. J.; Cho, Y. J.; Baik, S., In Situ Control of Oxygen Vacancies in TiO_2 by Atomic Layer Deposition for Resistive Switching Devices. *Nanotechnology* **2013**, *24*, 295202.

64. Zhang, Y.; Ding, Z.; Foster, C. W.; Banks, C. E.; Qiu, X.; Ji, X., Oxygen Vacancies Evoked Blue TiO_2 (B) Nanobelts with Efficiency Enhancement in Sodium Storage Behaviors. *Adv. Funct. Mater.* **2017**, *27*, 1700856.

65. Di Valentin, C.; Pacchioni, G.; Selloni, A., Reduced and n-Type Doped TiO_2: Nature of Ti^{3+} Species. *J. Phys. Chem. C* **2009**, *113*, 20543-20552.

66. Deskins, N. A.; Dupuis, M., Intrinsic Hole Migration Rates in TiO_2 from Density Functional Theory. *J. Phys. Chem. C* **2009**, *113*, 346 - 358.

67. Deskins, N. A.; Rousseau, R.; Dupuis, M., Localized Electronic States from Surface Hydroxyls and Polarons in TiO_2 (110). *J. Phys. Chem. C* **2009**, *113*, 14583-14586.

68. Deskins, N. A.; Rousseau, R.; Dupuis, M., Distribution of Ti^{3+} Surface Sites in Reduced TiO_2. *J. Phys. Chem. C* **2011**, *115*, 7562-7572.

69. Deskins, N. A.; Rousseau, R.; Dupuis, M., Defining the Role of Excess Electrons in the Surface Chemistry of TiO_2. *J. Phys. Chem. C* **2010**, *114*, 5891 - 5897.

70. Xia, T.; Zhang, Y.; Murowchick, J.; Chen, X., Vacuum-Treated Titanium Dioxide Nanocrystals: Optical Properties, Surface Disorder, Oxygen Vacancy, and Photocatalytic Activities. *Catal Today* **2014**, *225*, 2-9.

71. Morgan, B. J.; Watson, G. W., Intrinsic n-Type Defect Formation in TiO_2: A Comparison of Rutile and Anatase from GGA+ U Calculations. *J. Phys. Chem. C* **2010**, *114*, 2321-2328.

72. Deskins, N. A.; Dupuis, M., Electron Transport via Polaron Hopping in Bulk TiO_2: A Density Functional Theory Characterization. *Phys Rev B* **2007**, *75*.

73. Nakamura, I.; Negishi, N.; Kutsuna, S.; Ihara, T.; Sugihara, S.; Takeuchi, K., Role of Oxygen Vacancy in the Plasma-Treated TiO_2 Photocatalyst with Visible Light Activity for NO Removal. *J. Mol. Catal. A: Chem.* **2000**, *161*, 205-212.

74. Diebold, U., The Surface Science of Titanium Dioxide. *Surf. Sci. Rep.* **2003**, *48*, 53-229.

75. Fukui, K.-i.; Onishi, H.; Iwasawa, Y., Atom-Resolved Image of the TiO_2 (110) Surface by Noncontact Atomic Force Microscopy. *Phys. Rev. Lett.* **1997**, *79*, 4202.

76. Jin, C.; Liu, B.; Lei, Z.; Sun, J., Structure and Photoluminescence of the TiO_2 Films Grown by Atomic Layer Deposition Using Tetrakis-Dimethylamino Titanium and Ozone. *Nanoscale research letters* **2015**, *10*, 95.

77. Saha, D.; Ajimsha, R.; Rajiv, K.; Mukherjee, C.; Gupta, M.; Misra, P.; Kukreja, L., Spectroscopic Ellipsometry Characterization of Amorphous and Crystalline TiO_2 Thin Films Grown by Atomic Layer Deposition at Different Temperatures. *Appl. Surf. Sci.* **2014**, *315*, 116-123.

78. Hashimoto, S.; Tanaka, A., Alteration of Ti 2p XPS Spectrum for Titanium Oxide by Low-Energy Ar Ion Bombardment. *Surf. Interface Anal.* **2002**, *34*, 262-265.

79. Mott, N., Electrons in Non-Crystalline Materials: The Last Twenty Five Years. *Contemp. Phys.* **1985**, *26*, 203.

80. Brunschwig, B. S.; Sutin, N., Energy Surfaces, Reorganization Energies, and Coupling Elements in Electron Transfer. *Coordin Chem Rev* **1999**, *187*, 233-254.

81. Austin, I. G.; Mott, N. F., Polarons in Crystalline and Non-Crystalline Materials. *Adv. Phys.* **2001**, *50*, 757-812.

82. Yildiz, A.; Lisesivdin, S.; Kasap, M.; Mardare, D., Electrical Properties of TiO_2 Thin Films. *J. Non-Cryst. Solids* **2008**, *354*, 4944-4947.

83. Austin, I. G.; Mott, N. F., Polarons in Crystalline and Non-Crystalline Materials. *Adv. Phys.* **1969**, *18*.

84. Liu, T.; Dupuis, M.; Li, C., Band Structure Engineering: Insights from Defects, Band Gap, and Electron Mobility, from Study of Magnesium Tantalate. *J. Phys. Chem. C* **2016**, *120*, 6930 - 6937.

85. Ju, Y.; Wang, M.; Wang, Y.; Wang, S.; Fu, C., Electrical Properties of Amorphous Titanium Oxide Thin Films for Bolometric Application. *Adv. Condens. Matter Phys.* **2013**, *2013*, 1 - 5.

86. Rao, M. V. R.; Gandhi, Y.; Rao, L. S.; Sahayabaskaran, G.; Veeraiah, N., Electrical and Spectroscopic Properties of $LiF–Bi_2O_3–P_2O_5$:TiO_2 Glass System. *Mater. Chem. Phys.* **2011**, *126*, 58 - 68.

87. Sugiyama, K.; Takeuchi, Y., The Crystal Structure of Rutile as a Function of Temperature up to 1600º C. *Z. Kristallogr. Cryst. Mater.* **1991**, *194*, 305-313.

88. Howard, C. J.; Sabine, T. M.; Dickson, F., Structural and Thermal Parameters for Rutile and Anatase. *Acta Crystallogr. Sec. B* **1991**, *47*, 462-468.

89. Ihle, D.; Lorenz, B., Small-Polaron Conduction and Short-Range Order in Fe_3O_4. *J. Phys. C: Solid State Phys.* **1986**, *19*, 5239-5251.

90. Mott, N. F.; Davis, E. A., *Electronic Processes in Non-Crystalline Materials*, 2nd ed.; Clarendon Press: Oxford,, 1979.

91. Jonscher, A. K., Universal Dielectric Response. *Nature* **1977**, *267*, 673-679.

92. Long, A. R., Frequency-Dependent Loss in Amorphous-Semiconductors. *Adv. Phys.* **1982**, *31*, 553-637.

93. Konezny, S. J.; Richter, C.; Snoeberger, R. C.; Parent, A. R.; Brudvig, G. W.; Schmuttenmaer, C. A.; Batista, V. S., Fluctuation-Induced Tunneling Conductivity in Nanoporous TiO_2 Thin Films. *J. Phys. Chem. Lett.* **2011**, *2*, 1931-1936.
94. Elliott, S. R., AC Conduction in Amorphous-Chalcogenide and Pnictide Semiconductors. *Adv. Phys.* **1987**, *36*, 135-218.

2.9 Supplementary Information

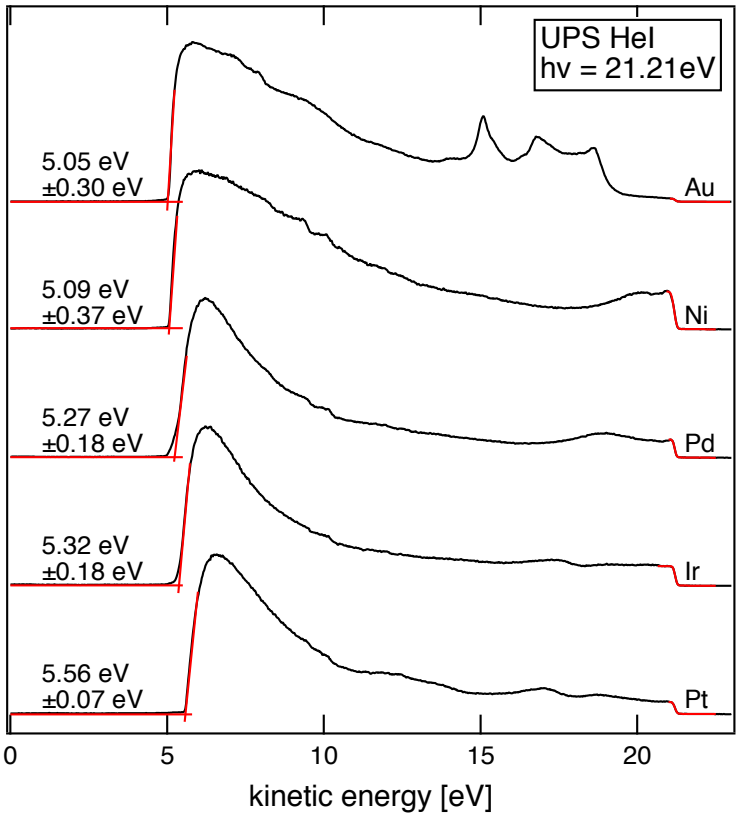

Figure S1 Ultraviolet photoelectron spectra for Ni, Pd, Pt, Ir, and Au. The work function for each element is indicated. The intersections of the two red lines on the low and high kinetic energy sides indicate the positions of energy of the secondary electron cutoff and the Fermi energy, respectively.

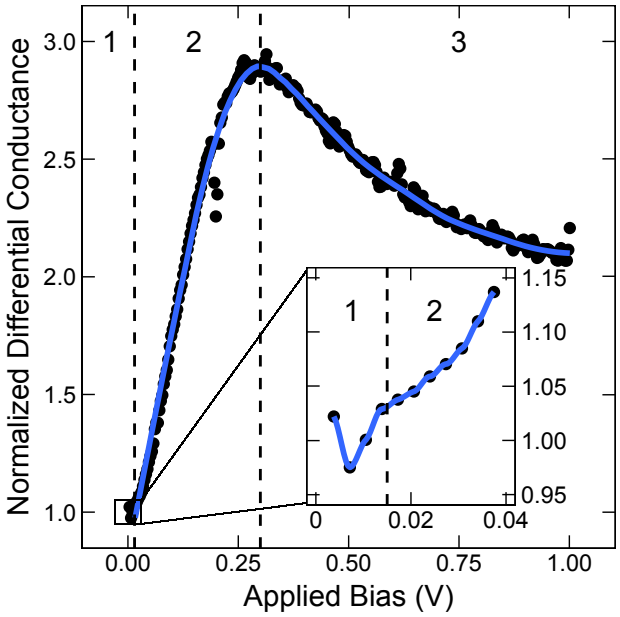

Figure S2 Normalized differential conductance for a p$^+$-Si|*a-TiO*$_2$|Ni device and *J-V* data plotted to show specific regions. The ohmic regime (region I) is depicted in a) and b), with the Schottky regime (region II) as well as the Fowler-Nordheim (like) transport (region III) depicted in c) and d). The normalized differential conductance is defined as $\frac{dJ}{dV}\left(\frac{V}{J}\right)$.

Table S1. Contact resistance measured by transmission line measurement method for various metal contacts. The compensated voltage was using the current respectively listed to the left.

Top Contact	Contact Resistance (Ω)	Current @ 10^{-2} V (A)	Compensated Voltage (V)	Current @ 0.1 V (A)	Compensated Voltage (V)
Ti	945 ± 44	~8×10^{-6}	7.6×10^{-3}	~100×10^{-6}	9.5×10^{-2}
Ir	5450 ± 750	~1×10^{-6}	5.5×10^{-3}	~10×10^{-6}	5.5×10^{-2}

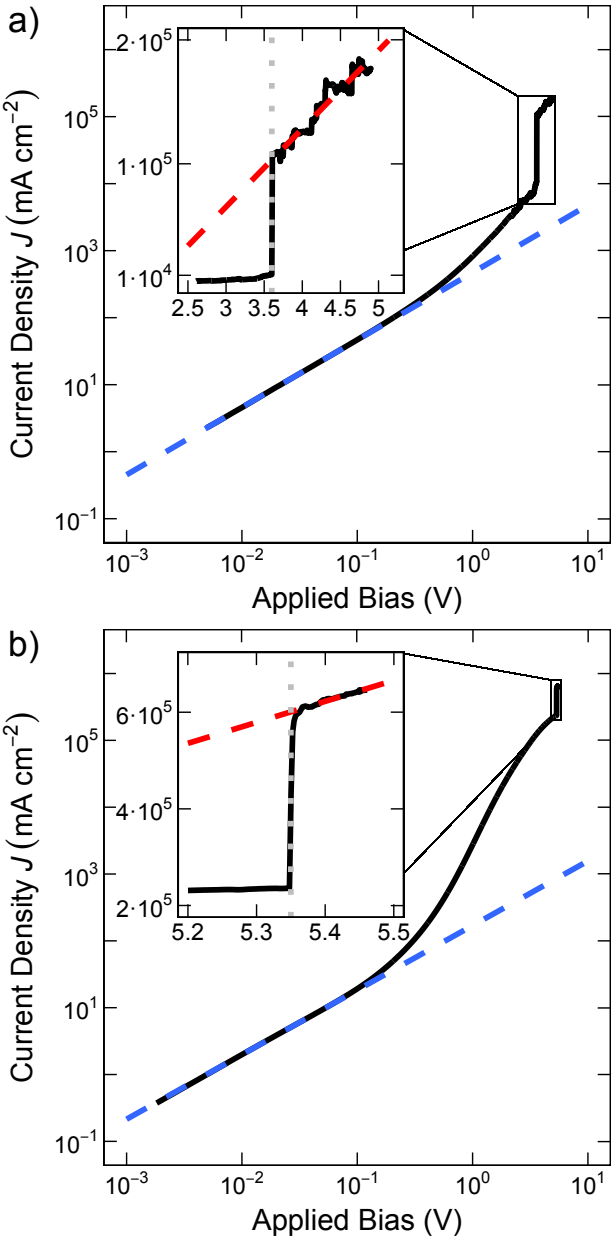
a)
Current Density J (mA cm^{-2})
Applied Bias (V)
b)
Current Density J (mA cm^{-2})
Applied Bias (V)

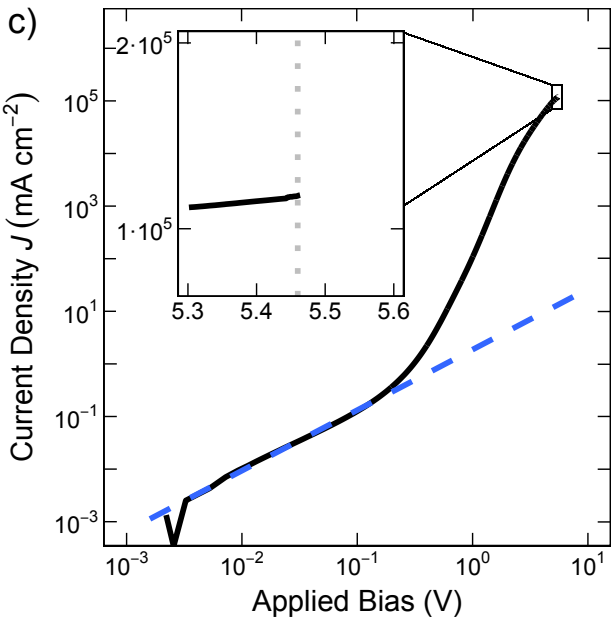

Figure S3 - *J-V* characteristics of a solid-state (a) p^+-Si|a-TiO_2|Au, (b) p^+-Si|a-TiO_2|Ir and (c) p^+-Si|a-TiO_2|Pd device, extended to applied biases > 5 V. The a-TiO_2 was ~ 68 nm thick. The inset is a plot of the crossover into the trap-filled regime. Linear regressions are shown for the ohmic region at low bias (blue dashed line), and the trap-filled space-charge-limited regimes (red dashed line in the inset). All devices had a secondary region except the p^+-Si|a-TiO_2|Pd device which exceeded the current limit of the potentiostat.

Table S2. Calculated trap densities, mobilities, and effective mobile charge-carrier densities for p^+-Si|a-TiO_2|metal devices with various metal top contacts.

	Trap Density (cm^{-3})	Mobility ($cm^2\ V^{-1}\ s^{-1}$)	Effective Mobile Charge-carrier Density (cm^{-3})
Mg	N/A	N/A	$(1.64\pm1.0)\times10^{16}$
Ti	N/A	N/A	$(2.54\pm1.2)\times10^{16}$
Ni	N/A	N/A	$(2.88\pm1.5)\times10^{16}$
Au	$(1.40\pm0.17)\times10^{19}$	$(2.08\pm0.02)\times10^{-4}$	$(3.83\pm2.4)\times10^{15}$
Ir	$(9.65\pm0.32)\times10^{18}$	$(9.45\pm0.26)\times10^{-4}$	$(2.66\pm1.3)\times10^{15}$
Pd	$(1.14\pm0.081)\times10^{19}$	N/A	$(6.38\pm3.29)\times10^{14}$
Pt	$(9.36\pm0.26)\times10^{18}$	$(5.67\pm0.15)\times10^{-4}$	$(6.35\pm4)\times10^{14}$

The interdigitated electrodes (IDEs) were used to measure the potential resolved conductance (EC-FET) in the a-TiO_2 (Figure 5). The conductance, *G,* was obtained from the conductivity by use of the cell constant, ($\sigma_{ecfet} = K \cdot G_{ecfet}$) where *K* is the cell constant and was estimated from:

$$K = \frac{2}{l(n-1)}\left(\frac{s}{w}\right)^{1/3} \quad \text{(S1)}$$

where *s* is the spacing between the electrode digits, *w* is the width of the electrode, *l* is the length, and *n* is the number of digits, 20 μm, 20 μm, 0.2 cm, and 224, respectively. This relationship produced a cell constant of $K = 0.045$ cm^{-1}. Samples showed a weak potential dependence of the conductance (G_{ecfet}) in the potential range -0.25 to 1.75 V vs RHE.

Table S3. Conductance and conductivity for the corresponding IDE samples.

Sample	G_{ecfet} / S	σ_{ecfet} / S cm^{-1}
1	2.2×10^{-4}	9.8×10^{-6}
3	3.8×10^{-4}	1.7×10^{-5}
4	1.9×10^{-4}	8.6×10^{-6}

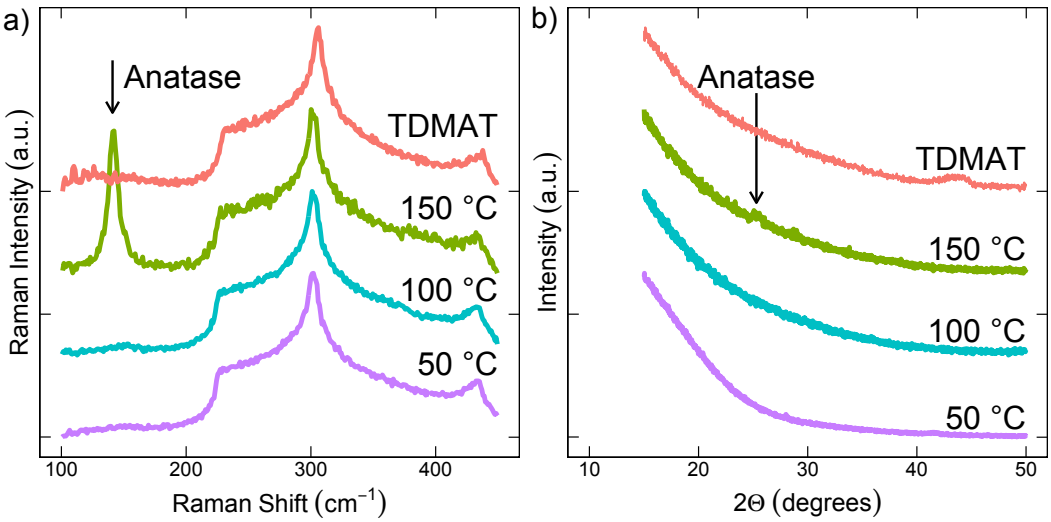

Figure S4 – a) Raman measurement of the various ALD deposited $TiCl_4$ precursor TiO_2 films and the same films measured by b) glancing incident x-ray diffraction (GIXRD). $TiCl_4$ films deposited at 50 and 100 ºC as well as the TDMAT film had an undetectable amount of crystallinity as evident in the lack of signal in the appropriate region of the Raman and GIXRD measurements. The film deposited at 150 ºC had a small fraction of crystallinity (Anatase) from the regions marked in both the Raman and GIXRD measurements.

Figure S5 shows the ATR-IR spectra for ALD TiO_2 films deposited using glass and silicon as the substrates, and $TiCl_4$ and TDMAT as the titanium precursor. On the ATR-IR spectra we observed that main peak features can be assigned to IR absorptions coming from the substrate. Furthermore, we observed the absence of Ti-OH absorption peaks related to metatitanic acid (H_2TiO_3) within the IR region of 3310 cm^{-1} and 1200–1071 cm^{-1}, indicating that the ALD TiO_2 films deposited in this work are free of H_2TiO_3 species.[1]

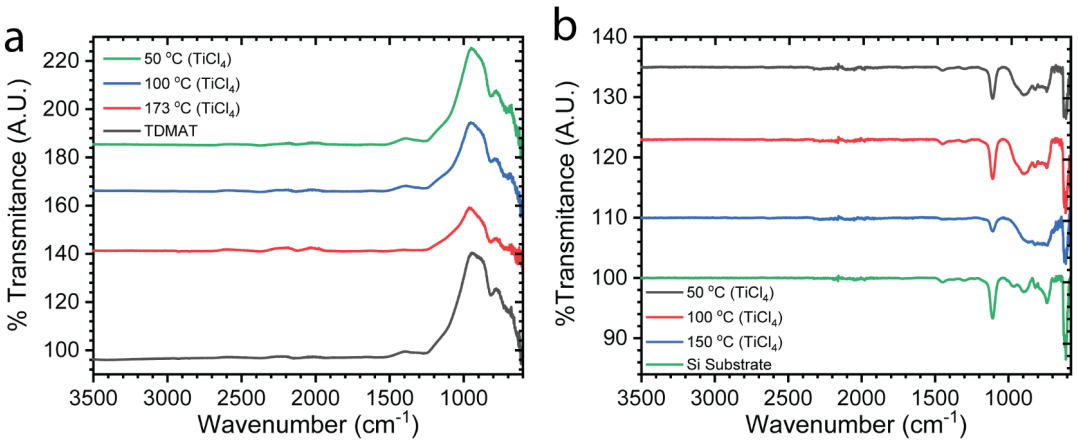

Figure S5 – ATR-IR spectra for ALD TiO2 films on a) glass and b) silicon substrate.

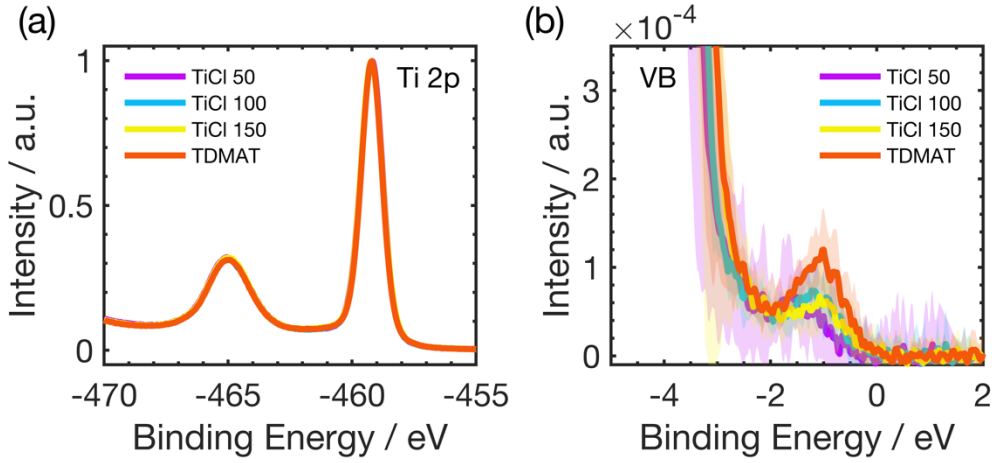

Figure S6. Average XPS (a) Ti 2p and (b) valence band spectra for TDMAT, $TiCl_4$-150, $TiCl_4$-100 and TiCl4-50 ºC for 10 different sample for each species. The average

spectra and respective standard deviation has been calculated for the valence band spectra and is visible in (b).

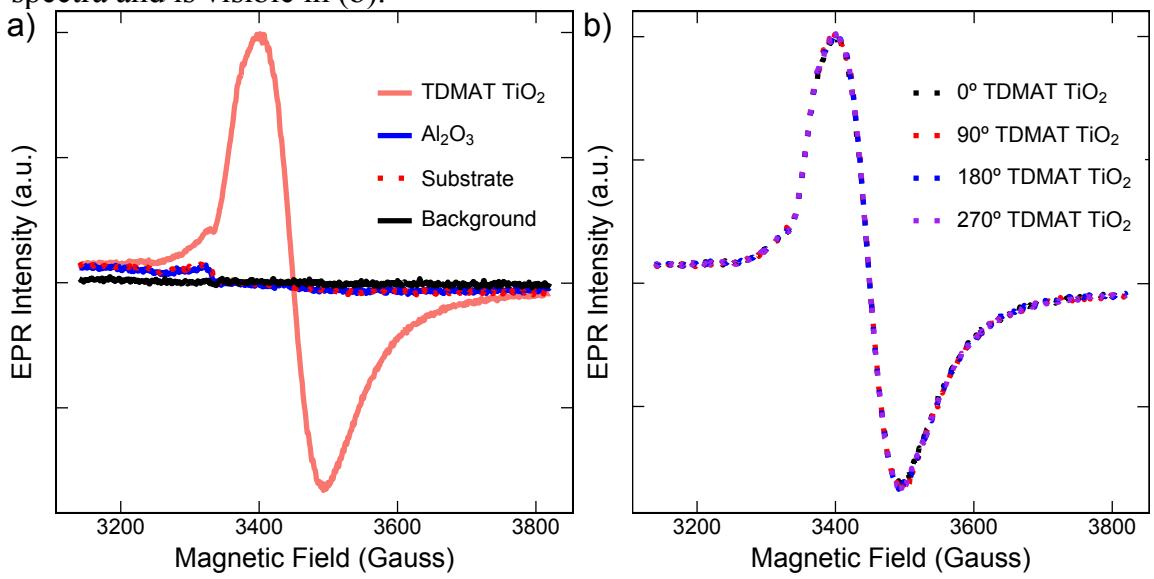

Figure S7. a) Comparison of the EPR spectra of TDMAT TiO_2 to the EPR spectra of ALD-deposited Al_2O_3, substrate-only and the background (an empty EPR tube). The broad peak was only present in the TDMAT TiO_2 whereas the slight bend at ~3300 G was due to the substrate. b) Comparison EPR spectra of TDMAT TiO_2 at various angles of rotation. The signal was independent of any rotation that the sample had with respect to the magnetic field.

Table S4. Attenuation length d for valence band states depending on take-off angle Θ. λ was calculated with QUASES-IMFP-TPP2M.

	d for Θ=0°	d for Θ=70°
AlKa (1486.6eV)	28.23 Å	9.66 Å

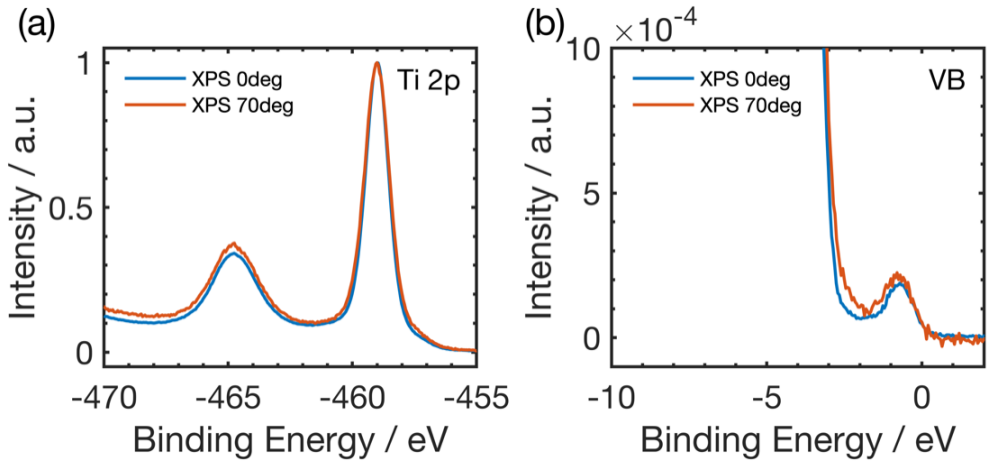

Figure S8. XPS spectra of the Ti 2p core levels of TDMAT TiO_2 and of the valence band for different emission angles (Θ=0° and 70°) relative to the surface normal. With increased surface sensitive (increased Θ), an increase in the oxygen shoulder at 532.5 eV was observed.[2]

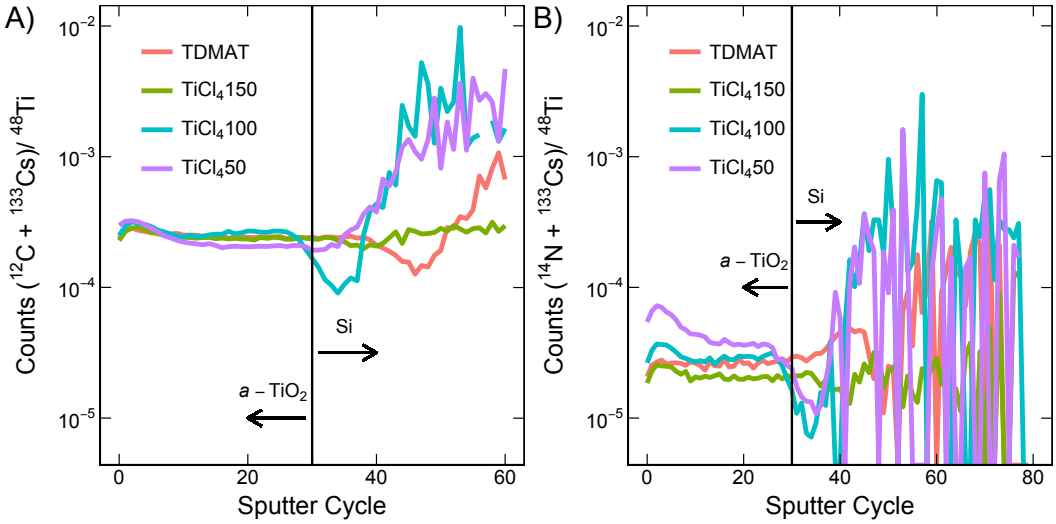

Figure S9. Normalized SIMS spectra of (a) ^{12}C and (b) ^{14}N for all a-TiO_2 samples. The first 30 sputter cycles are measuring the a-TiO_2 while the remaining cycles are measuring the underlying p^+-Si substrate. When comparing the SIMS spectra with the respective conductivity, no trend is apparent.

The charge transfer across the Ti|a-TiO_2|Ti|Ir|electrolyte junction can be modeled in terms of a double barrier generating a potential drop across the metal-insulator-catalyst (V_Ω) and catalyst-electrolyte junctions (V_{tafel}),[3-5]

$$V_{total} = \mathrm{V}_\Omega + V_{Tafel} = \frac{L}{q\mu N_D} i + \alpha \times 2.303 \ln\left(\frac{i}{i_0}\right) \quad \text{(S2)}$$

where L, α, and i_0 are the a-TiO_2 film thickness, Tafel slope, and the exchange current density, respectively. We assumed that the current is kinetically controlled across the potential range.

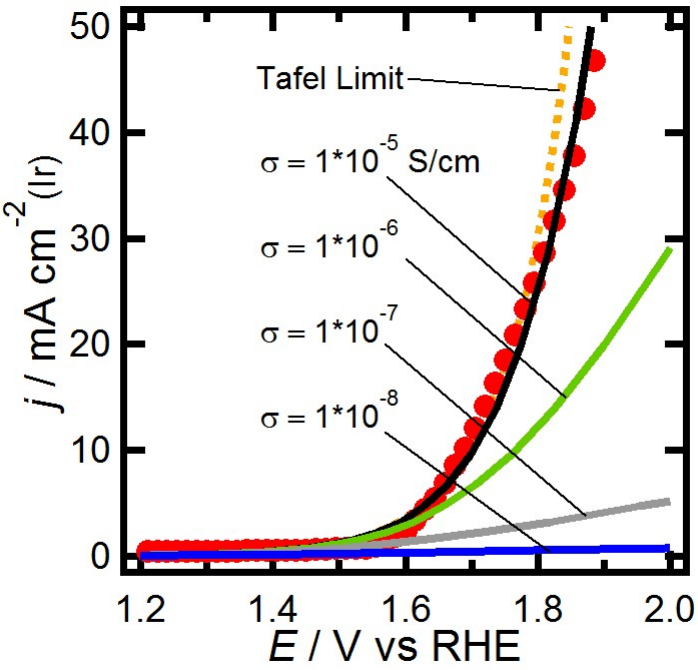

Figure S10. Comparison of the current-voltage curve obtained for p^+-Si|a-TiO_2|Ti|Ir films in 1 M H_2SO_4 with the values obtained from eq. S2, taking α = 41 mV dec^{-1} and I_0 = 0.07 mA cm^{-2}. It should be noted that the current has been renormalized with respect to the area covered by the Ir islands (14% coverage), since charge transfer is negligible in the absence of the catalysts. The orange trace shows the Tafel limit (charge transfer unhindered by the TiO_2 layer), which is very close to the experimental values though somewhat lower than on state-of-the-art Ir catalysts.[6-7] The simulations show that a-TiO_2 conductivity of the order of 10^{-5} S cm^{-1} has very little influence on the voltammetric responses, while significant current damping can be observed upon decreasing the conductivity by one order of magnitude. These trends demonstrate that the characteristic conductivity measured for the a-TiO_2 film obtained by ALD are capable of sustaining current in the range of 10 mA cm^{-2} without the need for invoking mediation by the valence or conduction bands.

2.10 Supplementary Information References

1. Mockūnaitė, S.; Ostachavičiūtė, S.; Valatka, E., Photocatalytic and Adsorptive Properties of Titanium Dioxide Prepared by Thermal Decomposition of Metatitanic Acid. *Chemija* **2012**, *23*.
2. Lichterman, M. F., et al., Direct Observation of the Energetics at a Semiconductor/Liquid Junction by Operando X-Ray Photoelectron Spectroscopy. *Energy Environ. Sci.* **2015**, *8*, 2409-2416.
3. Chazalviel, J.-N.; Allongue, P., On the Origin of the Efficient Nanoparticle Mediated Electron Transfer Across a Self-Assembled Monolayer. *J. Am. Chem. Soc.* **2011**, *133*, 762-764.
4. Kissling, G. P.; Miles, D. O.; Fermín, D. J., Electrochemical Charge Transfer Mediated by Metal Nanoparticles and Quantum Dots. *Phys. Chem. Chem. Phys.* **2011**, *13*, 21175-21185.
5. Bradbury, C. R.; Zhao, J.; Fermín, D. J., Distance-Independent Charge-Transfer Resistance at Gold Electrodes Modified by Thiol Monolayers and Metal Nanoparticles. *J. Phys. Chem. C* **2008**, *112*, 10153-10160.
6. Reier, T.; Oezaslan, M.; Strasser, P., Electrocatalytic Oxygen Evolution Reaction (OER) on Ru, Ir, and Pt Catalysts: A Comparative Study of Nanoparticles and Bulk Materials. *ACS Catal.* **2012**, *2*, 1765-1772.
7. McCrory, C. C. L.; Jung, S.; Ferrer, I. M.; Chatman, S. M.; Peters, J. C.; Jaramillo, T. F., Benchmarking Hydrogen Evolving Reaction and Oxygen Evolving Reaction Electrocatalysts for Solar Water Splitting Devices. *J. Am. Chem. Soc.* **2015**, *137*, 4347-4357.

Chapter 3

INVESTIGATION OF THE ORIGIN OF THE ELECTRONIC BARRIER IN ELECTROLESS DEPOSITED PLATINUM NANOPARTICLES ON P-SI

Nunez, P.D., Cabán-Acevedo M., Yu W., Richter M. H., Kennedy K., Villarino A. M., Brunschwig B. S., & Lewis N. S. " Investigation of the Origin of the Electronic Barrier in Electroless Deposited Platinum Nanoparticles on p-Si," *in preparation*.

3.1 Abstract

Inhomogeneous junctions between Pt and p-Si has been characterized by impedance spectroscopy, X-ray photoelectron spectroscopy (XPS), transmission electron microscopy (TEM), scanning electron microscopy (SEM), and electrochemical current density versus voltage (J-V) characteristics. The inhomogeneous junctions were formed by either electroless deposition onto a p-Si substrate. SEM spectroscopy showed that the films deposited particles with an average area of 1300 ± 1500 nm^2 and fractional coverage of 0.35 ± 0.02. XPS and TEM showed that the junction between the metal particle and the silicon are separated by an ultra-thin SiO_x layer. Electrochemical open circuit potential measurements with vanadium species at various solution potentials showed that the junction is not fixed but scales with the solution potential. In order to recreate a similar junction by e-beam deposition, it was required the SiO_x to be present before deposition to have the junction not pinned by the deposited Pt and controlled by either the solution potential or hydrogen present. Utilizing this information, a model for barrier height formation for p-Si|electroless Pt is constructed which indicates that the barrier height is determined based on the pathway the electrons traverse.

3.2 Introduction

The hydrogen evolution reaction by water splitting is a key process in the photoelectrochemical production of carbon-neutral fuels. P-type semiconductors with band gaps, E_g, that allow substantial absorption of sunlight ($E_g < 2$ eV) to enable the light-driven electrochemical reaction typically forms an ohmic junction, when placed in contact with a typical high-performing HER electrocatalysts and even newer generations of electrocatalysts.[1-2] This ohmic contact is unable to effectively convert harvested photons to a chemical bond in the form of H_2. In order to mitigate the formation of an ohmic contact, the junction must not be dominated by the high-performing electrocatalysts (HPEC).[1] Thus, energy-intensive buried junctions are formed by creating a p-n junction in order to mitigate the formation of an ohmic contact.[2-4] Less energy intensive processes like electrodeposition or electroless deposition of HPEC has been shown to produce a usable junction that performs better than the ohmic junction but worse than the buried junction.[1, 5-7]

Electrodeposition or electroless deposition of Pt has been shown to demonstrate this favorable junction when combined with p-Si or p-InP even though the valence band maximum (VBM) is significantly more positive than the work function of Pt.[1, 6-7] The relative alignment between the VBM of these p-type materials and the work function of Pt predicts that an ohmic contact should form which is the case for e-beam or sputter deposited Pt.[1, 3, 8] However, devices that are comprised of electroless and electrodeposited Pt onto p-Si are able to generate sizable photovoltages (~300 mV). Photovoltages from these types of systems appear to be somewhat independent of the VBM. XPS data indicate a band alignment that produces ohmic behavior for Pt on p-Si. The evaporation of Pt to the surface of p-Si confirms that the contact should be ohmic.[1, 3, 8]

These data hint at the energetics of p-Si with Pt deposited at the surface. However, the mechanism for the formation of a barrier height via electrodeposition and electroless deposition, despite the unfavorable band alignment energetics, remains to be elucidated. XPS data shows a weak peak in the Si 2p spectrum suggesting the formation of SiO_x after electrodeposition or electroless deposition that is not present after e-beam deposition of the same metal.[1] Other studies have investigated other deposition techniques and found similarly physical vapor deposition techniques create ohmic contacts while chemical deposition techniques do not.[8] Previous work utilizing these junctions have hypothesized that the formation of the barrier to be due to hydrogen amalgamation or the pinch-off effect.[1] However, no study to date has effectively proven or disproven either hypothesis. By having a greater understanding of the formation of the barrier height, then it could allow for more intelligently design photocathodes.

We describe herein a detailed investigation of the formation of the barrier height across a p-Si|Pt junctions formed in various manners, including impedance spectroscopy, X-ray photoelectron spectroscopy (XPS), transmission electron microscopy (TEM), scanning electron microscopy (SEM), and electrochemical current density versus voltage (*J-V*) characteristics. The experiments were designed to elucidate the formation of the barrier height as well as the factors that control the observed barrier as the solution junction to the system is varied. We consequently explore the role of the size of the catalyst to p-Si by fabricating analogous photocathodes by e-beam deposition. We have moreover applied the information gained from these studies to aid in the design of a more efficient Si photocathode for solar-driven hydrogen evolution.

3.3 Experimental Section

3.3.1 Sample Preparation

Materials and Chemicals

$FeCl_3$ (97%), $FeCl_2 \cdot 4H_2O$ (>99%), $CoCp_2PF_6$ (98%), $CoCp_2$ (recrystallized), CH_3CN (anhydrous) were all purchased from Sigma-Aldrich®. Compressed H_2 gas purchased from Air Liquide America Specialty Gases LLC. Water with a resistivity, ρ, >18 MΩ·cm was obtained from a Barnsted Millipore purification system and was used throughout. All chemicals, including sulfuric acid (99.999%, Sigma-Aldrich and ~18 M, ACS Reagent Grade, J.T. Baker), hydrogen peroxide (~30%, ~13 M, VWR), hydrochloric acid (ACS Grade, VWR), and buffered HF (aq) (semiconductor-grade, Transene), were used as received, unless otherwise noted. Two types of crystalline, single-side polished, Si substrates were used: p-Si(111) (Boron-doped, ρ = 7 – 8 Ω·cm, Addison Engineering).

Preparation of Substrates

The Si wafers were cleaned using an RCA SC-1 procedure that consisted of a 10 min soak in a 3:1 (by volume) solution made from 3 parts H_2SO_4 (aq) (~18 M) and 1 part H_2O_2(aq) (~13 M). The samples were then briefly etched in a solution of buffered HF(aq) (Transcene). The Si samples were cleaned using an RCA SC-2 procedure by soaking the samples for 10 min at 75 °C in a 5:1:1 (by volume) solution of H_2O, HCl(aq) (~11 M), and H_2O_2(aq) (~13 M). The RCA SC-2 procedure left a thin passivating oxide layer on the Si surface.

Electroless Deposition

Before each experiment, the electrodes were individually subjected to a 1 min buffered hydrofluoric acid (BHF, Transcene Inc.) treatment, followed by a 2 min 1 mM H_2PtCl_6/0.5 M HF electroless platinization procedure, similar to as previously published work.[1] Each electrode was thoroughly rinsed with deionized water before

and after each chemical treatment, and characterized immediately, to avoid excess electrode aging.

Electron-Beam Metal Deposition

Samples were patterned via optical lithography or placed onto a shadow mask, mounted, and pumped down to a base pressure of $<10^{-5}$ Torr in an electron-beam evaporator system (Ångstrom Engineering Inc.). Pt was evaporated from source metals that were at least 4N purity. Deposition rates ranged from 0.020 to 0.080 nm s^{-1}, as monitored by a quartz-crystal microbalance. Deposition was stopped when the film thickness reached a thickness of 7.5 ± 2.5 nm and ~35 nm for electrochemical and solid-state samples, respectively.

Electrode Fabrication

Electrodes were fabricated by using a scribe to cleave the e-beam deposited samples into ~0.1 cm^2 pieces. The samples were patterned into islands for electrochemical measurements. A positive photoresist, S1813 (Shipley), was patterned, metal pads or islands deposited, and then the photoresist was removed by gently sonicating in acetone for ~1 min to leave the desired pattern. Ohmic contact was made by scratching the back of the Si sample with an In-Ga eutectic (Alfa-Aesar, 99.999%), and the back contact to the sample was affixed to a Cu wire with double-sided Cu tape. The Cu wire was threaded through a glass tube (Corning Incorporation, Pyrex tubing, 7740 glass), and all but the front of the sample was encapsulated with Loctite epoxy (Hysol 9462). After curing overnight, the electrode was scanned with an Epson scanner (V370) and analyzed with ImageJ software to determine the area of the exposed region, which was ~0.1 cm^{-2}.

3.3.2 Physical Characterization

3.3.3 Photoelectron Spectroscopy

X-ray photoelectron spectroscopic (XPS) data were collected on p-Si after electroless platinization using a Kratos Axis Ultra system with a base pressure of 1×10^{-9} Torr. The x-ray source was a monochromatic Al Kα line at 1486.6 eV. Photoelectrons were collected at 0° from the surface normal with a retarding pass energy of 160 eV for survey XPS scans, 10 eV for high-resolution core levels, and 20 eV for valence-band XPS scans.

Work function measurements were performed using He I ultraviolet photoelectron spectroscopy (UPS) on the Kratos Axis Ultra system. A pass energy of 5 eV was used in conjunction with an aperture of 110 μm. Prior to the measurements, pure metal samples (>99.99%) were sputter cleaned for 30 min with 4 kV Argon Ions. The work function (φ_{WF}) was calculated from the measured spectra on a kinetic energy scale using eq 1:

$$\phi_{WF} = E_{sec,meas} - E_{F,meas} + 21.21 \qquad (1)$$

where $E_{\text{sec, meas}}$ and $E_{\text{F, meas}}$ are the measured energy of the secondary electron cutoff and the Fermi energy, respectively, and 21.21eV is the photon energy for He I excitation. The secondary electron cutoff and Fermi energy were obtained by calculating the intercept of a linear fit of the steep electron cutoff to that of the background and by fitting a Fermi distribution to the valance-band maximum, respectively.

Transmission Electron Microscopy

Transmission electron microscopy (TEM) lamella samples of p-Si|electroless Pt and p-Si|SiO_x|e-beam Pt were prepared by focused Ga-ion beam (FIB) using a FEI Nova-600 Nanolab FIB/FESEM. The surface was coated with a carbon protection layers

prior to the deposition of a Pt capping layer and exposure to the FIB. The lamella was thinned using 30 kV Ga ions and the damaged zone of the lamella was reduced by performing the final thinning steps using 8 kV Ga ions. High-resolution TEM (HRTEM) data was collected using a FEI Tecnai Polara (F30) TEM at an accelerating voltage of 300 keV.

3.3.4 Electrochemical Characterization

Electrochemical data were obtained using a Bio-Logic SP-200 potentiostat in a three-electrode configuration with 1.0 M H_2SO_4(aq) as the electrolyte. A carbon rod (Strem Chemicals, 99.999%) was used as the counter electrode, and a $Hg/HgSO_4$ electrode (Gamry Instruments) was used as the reference electrode. An ELH-type tungsten-halogen lamp provided light that passed through a quartz diffuser to reach the Pyrex electrochemical cell. The illumination intensity was measured by a Si photodiode (Thorlabs) and the light intensity was adjusted to produce the same current on the photodiode as was produced by illumination with 100 mW cm^{-2} of Air Mass 1.5 sunlight. Cyclic voltammetric data were collected at a 40 mV s^{-1} scan rate.

Sample characterization consisted of cyclic voltammetry (CV) under illumination and no illumination, and electrochemical impedance spectroscopy (EIS) in the dark. The EIS data was then fitted using the instrument's software (EC-Lab®) to produce capacitance-voltage, or more commonly Mott-Schottky, plots. Before each complete experiment, a CV was run using a Pt disk working electrode to confirm a stable solution potential ($E_{Ref} \approx 0$ V), and the light source was calibrated as previously mentioned. In addition, the cobaltocene CV data was corrected for 85% of the uncompensated resistance calculated from the slope of the straight line of the reduction wave in the Pt disk data.

Vanadium Redox Couple

The open-circuit potential of various p-Si electrodes was measured under 1 sun of illumination in a solution of 1.0 M H_2SO_4 saturated with V_2O_5 in an oxygen-free glovebox. Since vanadium has three well-defined redox couples ($V^{2+/3+}$, $V^{3+/4+}$ and $V^{4+/5+}$), the electrochemical potential was varied by reducing the solution with a zinc rod or by pipetting in fresh solution of 1.0 M H_2SO_4 saturated with V_2O_5 until the desired solution potential was reached.[9-11] Once the desired solution potential was reached, the light source was calibrated to ensure an equivalent light flux for each measurement.

Photoelectrochemical Hydrogen Evolution

The cyclic voltammogram (CV) of all photoelectrodes were obtained in a custom-made two-compartment glass (pyrex) cell with a flat bottom, separated by a Nafion membrane (Fuel Cell Store). All electrodes were etched in buffered HF for 60 s prior to CV tests. All tests were performed in 1.0 M H_2SO_4(aq) electrolyte (VWR Chemical) under continuous H_2 purging, vigorous stirring and ~1-Sun illumination. The ELH-type tungsten-halogen lamp with a custom housing was used as a light source and its illumination intensity at the position of working electrode was calibrated using a calibrated Si photodiode (FDS100, Thorlab). The mercury sulfate electrode (MSE) (CH Instrument) was used as the reference electrode, the potential of which was calibrated to be +0.687 V vs. RHE under the same condition. A Pt wire was used as the counter electrode. The CV data were obtained on a MPG-2-44 potentiostat (Bio-Logic Science Instrument) at a scan rate of 40 mV/s. The CV tests start from measuring the values of open-circuit potentials (OCP) under illumination for 10-20 s, followed by scanning from -0.025 V to the OCP potential towards more negative potentials so as to avoid passing anodic currents.

3.3.5 Conductivity Measurements

Current density versus voltage (*J-V*) data were collected on solid-state analogous samples that consisted of p-Si with an RCA-2 SiO_x layer and a 35 nm Pt top contact (p-Si|SiO_x|Pt). For electrical contact, In-Ga was scratched on to the back of Si and the exposed Cu of Cu double-sided tape affixed to a glass slide. The electrical data were collected using either a Bio-Logic SP-200 or SP-300 in a two-electrode setup with the working electrode lead connected to the bottom contact (Cu tape) and the reference electrode lead connected to the top contact (Pt). *J-V* data were collected at 100 mV s^{-1}.

Temperature-Dependent Conductivity

The samples used for the measurement were the same as the aforementioned sample used to measure the *J-V* characteristics. Using a home-built cryostat, dry N_2(g) was flowed at temperatures ranging from 100 to 290 K. The temperature of the sample was monitored by a type K thermocouple. The sample was allowed to thermally equilibrate for 5 minutes prior to each measurement in the dark. The data were collected using a Bio-Logic SP-200 or SP-300.

Impedance Measurements

Impedance measurements were conducted in the dark using a Bio-Logic SP-200. The flat-band potential, dopant density and barrier height were determined from the impedance data using Mott-Schottky analysis. The 25 mV (peak-to-peak) AC signal was swept through a frequency range of 1 KHz to 1 MHz with a DC bias of -1.5 to 0 V in 31 equal steps. The area normalized differential capacitance of the space-charge region was determined by fitting the data to a Randles circuit, a resistor in series with a parallel capacitor and resistor.

3.4 Results

3.4.1 Effect of the Solution Potential

Figure 1 shows the dependence of the open circuit potential (V_{oc}) on the measured solution potential for H-terminated p-Si (red, squares), p-Si|e-beam Pt islands (green, circles), and p-Si|electroless Pt (blue, triangles) in contact with 1.0 M H_2SO_4 saturated with V_2O_5 under 100 mW cm^{-2} of illumination. In the case of the p-Si|e-beam Pt island sample, 2 nm of platinum were deposited to prepare a discontinuous film with a morphology that more closely resembles the Pt islands deposited by electroless deposition which can be seen in Figure S1. Each point represents an average of at least 5 electrodes. The response of the H-terminated p-Si is in relative agreement with previous works that used various non-aqueous redox couples.[12] Three regions exist that are present in the H-terminated p-Si and p-Si| electroless Pt electrodes: low, intermediate, and high V_{oc} regimes. Both the low and high V_{oc} regimes are insensitive to changes in the solution and maintain a potential of 50 ± 25 mV and 470 ± 20 mV, respectively. The intermediate regime scales directly with changes to the solution potential. The p-Si|e-beam Pt islands electrodes were insensitive to the changes in the solution potential and maintained a V_{oc} of 80 ± 20 mV. The p-Si|electroless Pt electrodes consistently produced a smaller V_{oc} compared to the H-terminated p-Si electrodes.

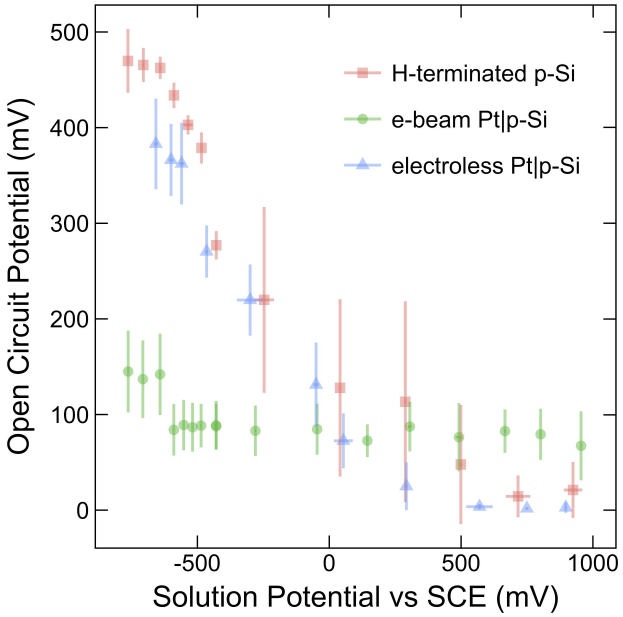

Figure 1. V_{oc} of H-terminated p-Si, p-Si|e-beam Pt islands and p-Si|electroless Pt in contact with 1.0 M H_2SO_4 saturated with V_2O_5 at various solution potentials under 100 mW cm^{-2} of illumination.

3.4.2 Effect of the Solution Potential

Structure of the Electroless Pt Photocathode

Figure 2 scanning electron micrographs show that 2 min of electroless deposition of Pt onto the p-Si surface produces discontinuous nanoparticles. Coalesced particles were considered to be single particle if there was contact. The particles have a large range of areas (1300 ± 1500 nm^2) and cover 35 ± 2 % of the surface. When the area of the particle is converted to a circular patch the effective diameter was found to be 41 ± 24 nm with an effective pitch of 61 ± 24 nm in a square configuration.

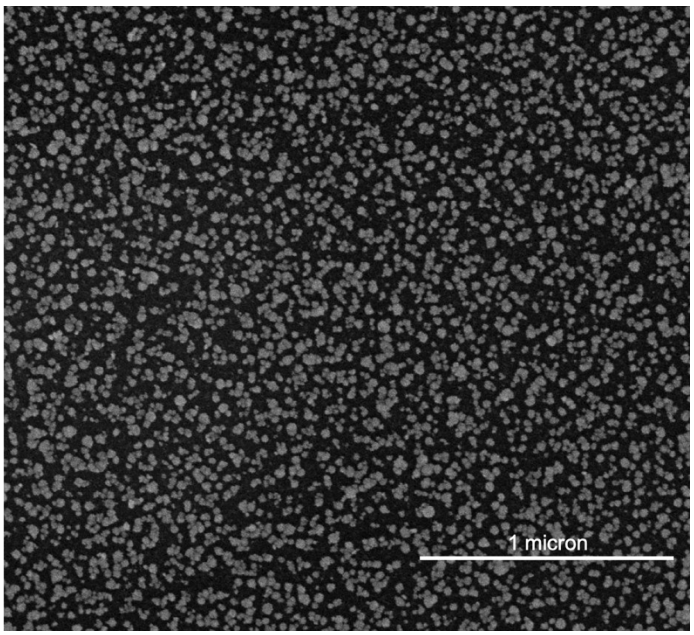

Figure 2. SEM micrograph of Pt deposited on the surface of p-Si. Coverage was found to be 0.35 ± 0.02. Overall the average area for each particle was found to be 1300 ± 1500 nm^2 which results in an effective diameter of 41 ± 24 nm and pitch of 61 ± 24 nm.

X-ray Photo-spectroscopy

Figure 3 shows the XPS spectra of the p-Si surface after various surface treatments that consisted of etching and/or Pt electroless deposition. Samples that had Pt deposited on the surface from exposure to a solution of 1.0 mM K_2PtCl_6 and 0.1 M HF showed significantly higher levels of oxidation as compared to the surface after chemically-producing silicon oxide by RCA-2 cleaning. Samples that had Pt deposited on the surface underwent the same HF etching process that produced the H-terminated surface. The level of surface oxidation experienced a slight decrease after etching; however, the levels of silicon oxide remained greater than the chemically-produced silicon oxide. The Si 2p peaks shift towards higher binding energies by 130, 320, and 130 meV relative to the H-terminated Si 2p peak for the RCA-2 cleaned, electroless Pt deposited and electroless Pt deposited after further HF

treatment, respectively. The relative oxide peak for the electroless Pt deposited surface before and after HF etching remains higher than the fully oxidized RCA2-cleaned surface. The Si 2p peaks show no evidence of silicide formation. The Pt 4f peaks show that the Pt deposited by electroless deposition is metallic Pt.

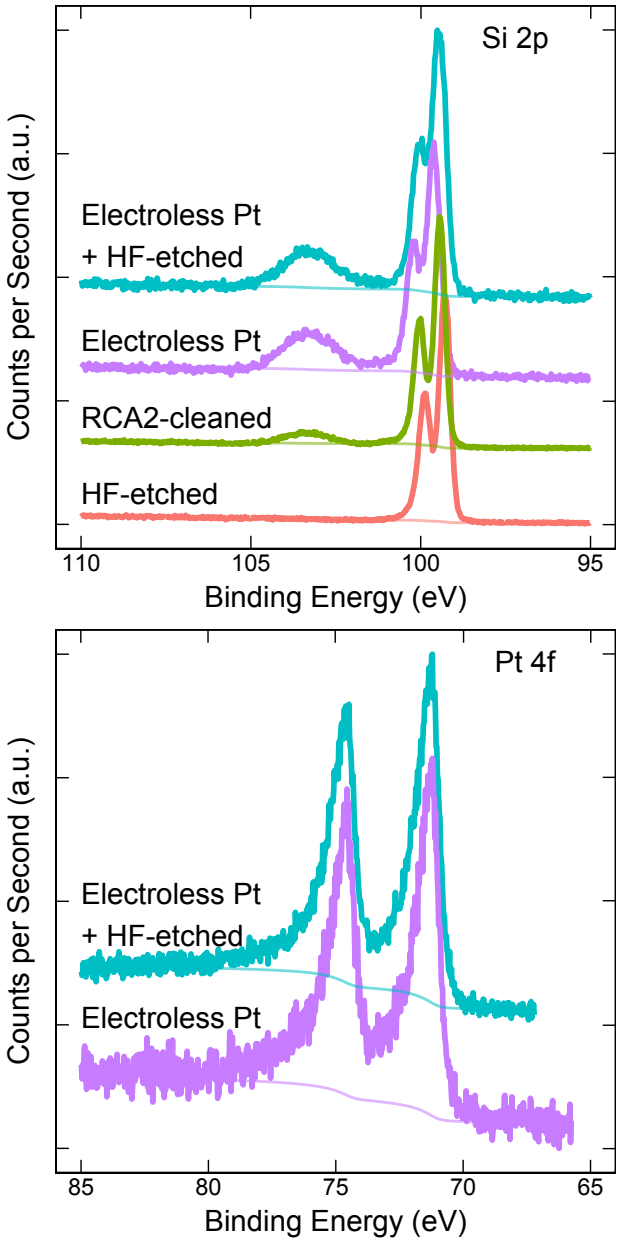

Figure 3. XPS spectra of Si 2p core levels for H-terminated, post RCA-2 cleaning, post electroless Pt deposition and post HF etching after electroless Pt deposition as

well as Pt 4f after electroless Pt deposition and subsequent HF etching after the electroless Pt deposition.

Transmission Electron Microscopy

Figure 4 show an HRTEM image of the surface interface for p-Si|electroless Pt. In the HRTEM image for p-Si|electroless Pt we also observed the presence of an interfacial amorphous SiO_x layer between the Pt layer and the silicon surface while the underlying silicon surface is rough. We attribute both the presence of the SiO_x layer and the roughening of the silicon surface to be a byproduct of the electroless Pt deposition reaction. The roughening of the silicon surface makes it difficult to make an accurate determination of the thickness of the SiO_x layer, but the thickness is estimated to be ~ 2 nm.

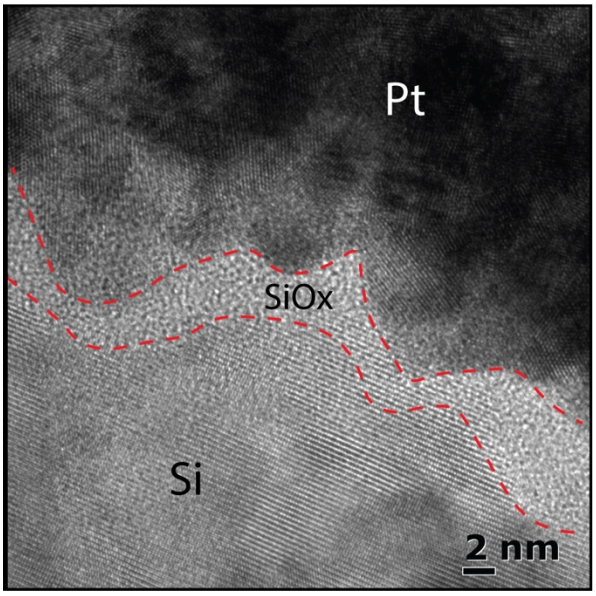

Figure 4. High-resolution electron microscopy (HRTEM) images of the p-Si|electroless Pt surface interface. Dashed red lines were added to highlight the boundary of the interfacial silicon oxide (SiO_x) layer.

3.4.3 Analogous Photocathode

Figure 5 shows that p-Si|SiO_x|e-beam Pt electrodes were fabricated and achieved similar levels of performance to the p-Si|electroless Pt electrodes in light-driven hydrogen evolution. The Pt catalyst were patterned into a 3 x 7 μm square pattern and isolated from the p-Si by a thin oxide layer grown by RCA-2 cleaning the wafer. HF etching of the the p-Si|SiO_x|e-beam Pt samples was required prior to testing to achieve a similar level of performance as the p-Si|electroless Pt samples. If etching was not conducted on the p-Si|SiO_x|e-beam Pt sample then the performance was similar to the p-Si|electroless Pt dark performance. Pt deposited directly to the p-Si using e-beam (p-Si|e-beam Pt), performed similarly to the Pt disk, and showed no difference between illuminated and dark conditions. The presence of the SiO_x after etching was confirmed by HRTEM in Figure S2.

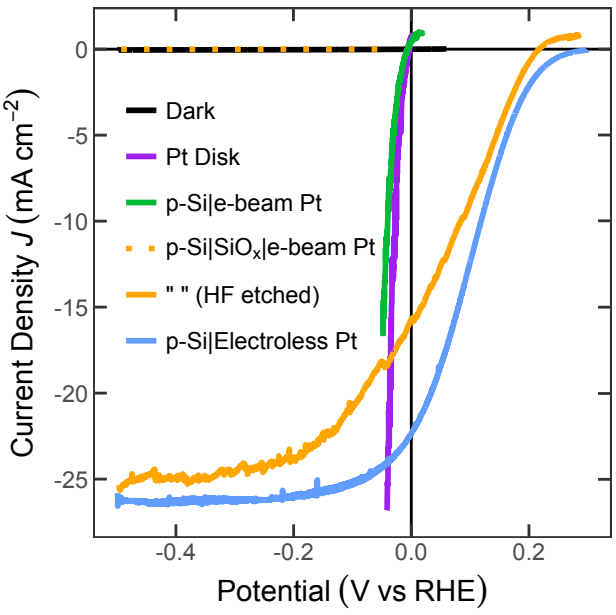

Figure 5. Electrochemical *J-V* measurement in 1.0 M H_2SO_4 and 1 atmosphere of H_2 comparing the performance for 3 x 7 μm analogous

electrodes with and without the SiO_x isolating the Pt catalyst to the electroless Pt.

Single Pt Island Electrical Characterization

Figure 6 shows the solid-state *J-V* characteristics for a p-Si|SiO_x|Pt device with a pad size of 0.016 cm^2. It can be seen that the electrode does not exhibit an ohmic response as would be expected without the SiO_x as is in the case of the p-Si|e-beam Pt. The asymmetric *J-V* characteristics show that applying a bias is met with a large resistance. This resistance is consistent with observations for performing HER and nanoelectrical measurements with p-Si|electroless Pt samples.[1, 13]

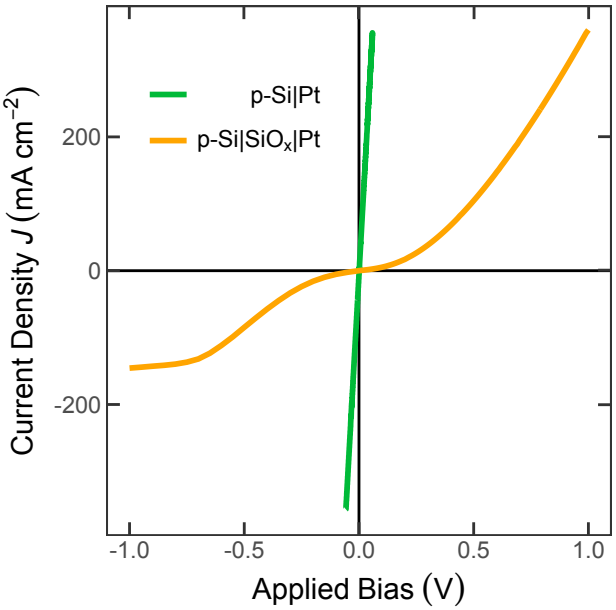

Figure 6. Solid-state *J-V* measurement of p-Si|SiO_x|Pt and p-Si|Pt devices. The p-Si|Pt device exhibits an ohmic *J-V* characteristic while the p-Si|SiO_x|Pt device has an asymmetrical *J-V* characteristic.

Impedance Spectroscopy

Impedance spectroscopy was conducted to determine the differential capacitance of the p-Si|SiO_x|Pt device. Figure 7 shows the resulting C^{-2}-V characteristics. The slope of the linear region indicates a dopant density $1.6 \pm 0.2 \times 10^{15}$ cm^{-3} which corresponds to a resistivity of ~9 Ω·cm, close to the manufacturer's specified rating of 7-8 Ω · cm. By extending the linear region, the x-intercept indicates a flat-band potential -0.48 ± 0.1 eV which, combined with the dopant density, yields a barrier height of -0.17 eV ± 0.1 eV. The negative barrier height indicates that the junction directly underneath the Pt contact is in accumulation. The SiO_x between the deposited Pt and the p-Si does not force the junction to produce an effective usable barrier height.

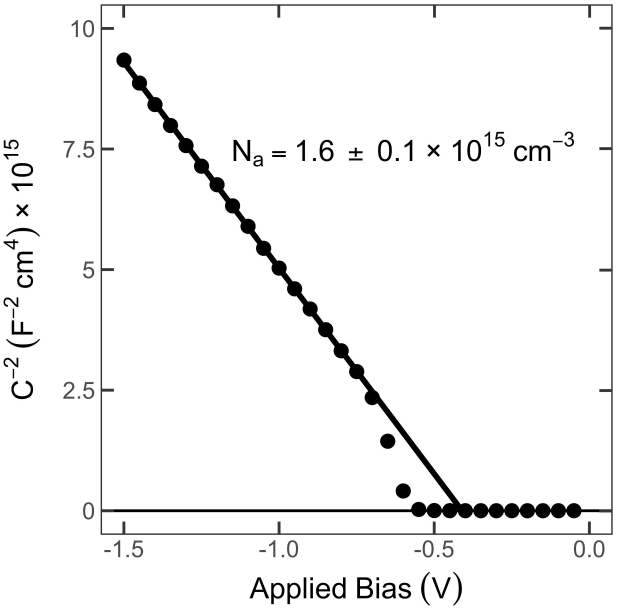

Figure 7. Mott-schottky plot of p-Si|SiO_x|Pt solid-state device. From the slope and x-intercept the number of holes, flat-band potential and barrier height is found to be $1.6 \pm 0.2 \times 10^{15}$ cm^{-3}, -0.48 ± 0.1 and -0.17 eV, respectively.

3.4.4 Influence of Catalyst Size

Ensemble Pt Islands Electrochemical Characteristics

Since the patterned 3 x 7 µm p-Si|SiO_x|Pt structured electrode had similar characteristics to the p-Si|electroless Pt electrode, the dependence of the electrode relative to the catalyst size was investigated in light-driven hydrogen evolution. The results can be seen in Figure 7. The diameter and pitch of the catalyst islands were scaled, but held to a constant coverage of ~14%. The performance of the devices was found to be independent of the size of the catalyst even though the p-Si|SiO_x|Pt structured electrodes scaled over ~3 orders of magnitude. If the effective diameter and pitch of the p-Si|electroless Pt electrodes are taken into account then the performance independence scales for 5 orders of magnitude. The V_{oc} of the same electrodes were measured against various solution potentials using the same vanadium redox couples at low, intermediate, and high solution potentials. No visible trend was apparent with the resulting Voc and the catalyst size. The resulting V_{oc} was very similar to the electroless Pt which can be seen in Figure 8.

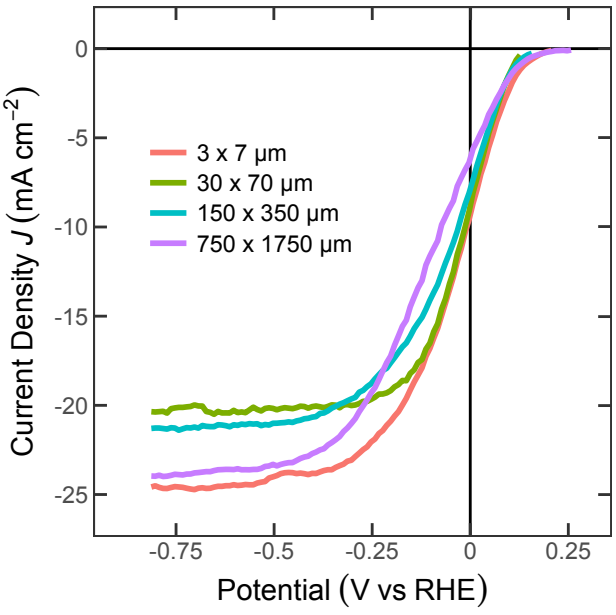

Figure 8. Electrochemical *J-V* measurement in 1.0 M H_2SO_4, 1 atmosphere of H_2 and 1 sun of illumination comparing the performance of various diameter and constant coverage for p-Si|SiO_x|Pt structured electrodes. All electrodes that were HF etched prior to the measurement.

3.4.5 Influence of Hydrogen

The structure p-Si|SiO_x|e-beam Pt solid-state device exhibited a response in the *J-V* characteristics once exposed to H_2 (g). The response before and during exposure can be seen in Figure 9. The exposure to hydrogen gas is exhibiting not just a resistive response but also a change in the barrier height. The impedance-spectroscopy of the MOS-structured electrode while exposed to hydrogen gas shows that the flat-band potential shifts by 0.8 ± 0.1 eV underneath the Pt catalyst as seen in Figure 10. This change in the barrier height translates into a usable barrier as the MOS-structured device exhibits a sizable photoresponse when measuring the V_{oc} (Figure S3).

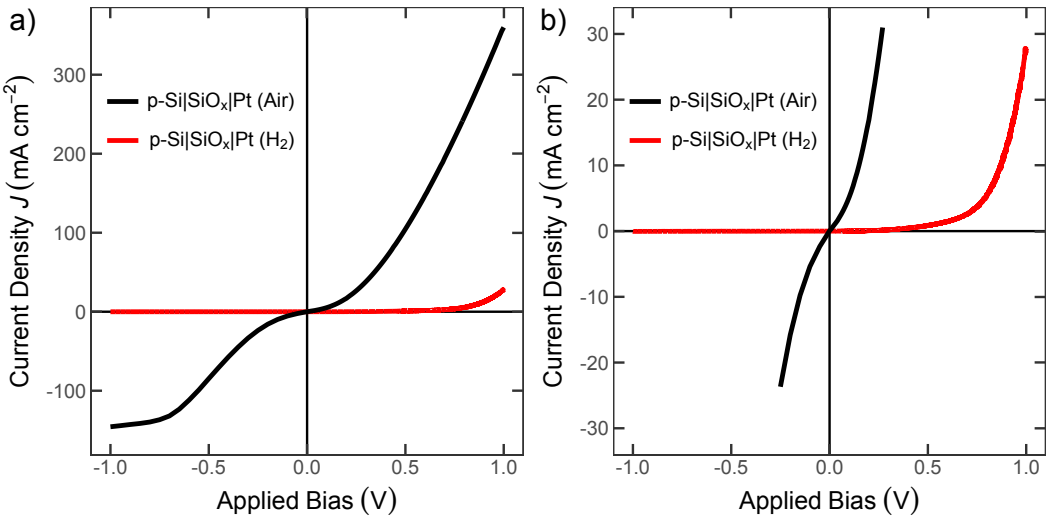

Figure 9. a) Solid-state *J-V* characteristics of p-Si|SiO_x|Pt solid-state device before and during exposure to H_2 (g) and b) zoomed in of a).

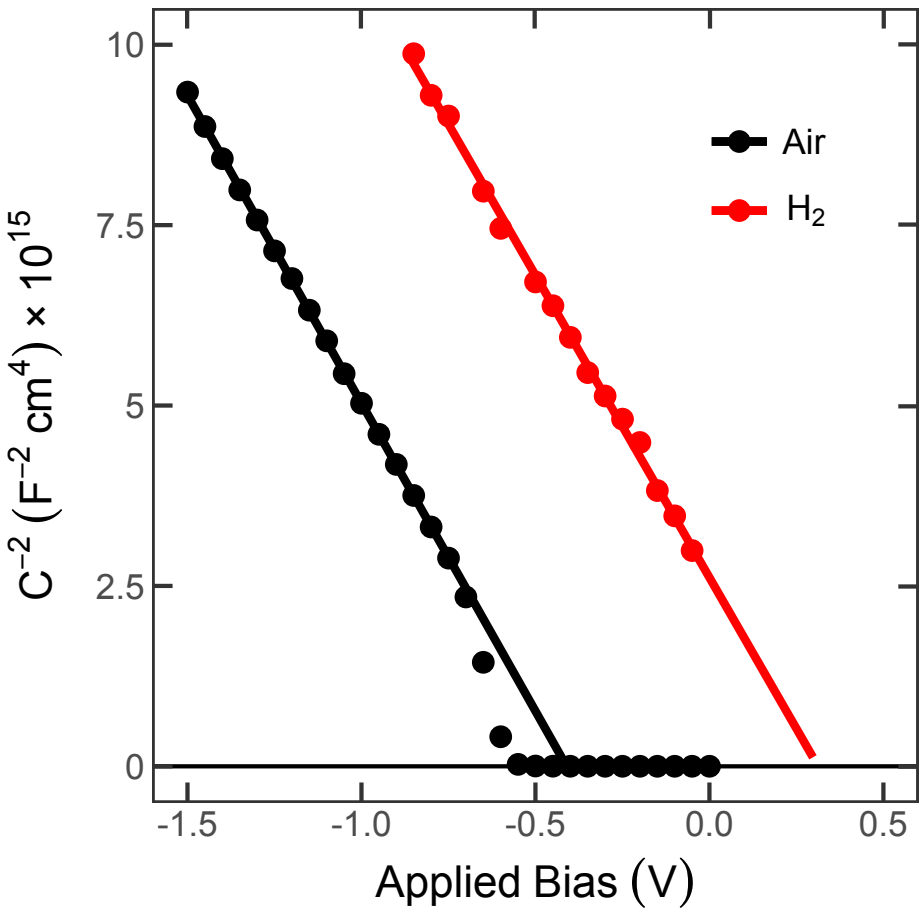

Figure 10. Mott-schottky plot of p-Si|SiO_x|Pt solid-state device before and during exposure to H_2 (g). The dopant densities derived from the slope of the linear regions agree with each other and the manufacturer's specification. Upon exposure to H_2 (g), the flat-band potential shifts by 0.8 ± 0.1 eV resulting in a final flat-band potential and barrier height of 0.35 ± 0.1 eV and 0.58 ± 0.1 eV, respectively.

3.5 Discussion

3.5.1 Solution Potential Controlled Barrier Height

Figure 1 shows the dependence of the V_{oc} on the measured solution potential for H-terminated p-Si, p-Si|e-beam Pt islands, and p-Si|electroless Pt in contact with 1.0 M H_2SO_4 saturated with V_2O_5 under 100 mW cm^{-2} of illumination. The response of the H-terminated p-Si is in agreement with previous works that used various non-aqueous redox couples even though only one solution is used and the solution potential was adjusted through the addition of metallic zinc.[12] As was observed by Grimm et al.,

three regions are present in the H-terminated: low, intermediate and high V_{oc} regimes. Both the low and high V_{oc} regimes are relatively insensitive to changes in the solution while the intermediate regime scales directly with changes to the solution potential.

These results validate the use of the vanadium electrolyte solution as an alternative to using various redox couples in order to probe the response of a semiconductor electrode to a change in the solution potential. A slight difference exists though between the two methods. The amount V_{oc} generated from the H-terminated p-Si using the vanadium electrolyte solution was slightly lower than the various redox couples at an equivalent solution potential. This difference is likely due to the reduction of oxidized species that are able to collect the photogenerated electrons from the surface of the semiconductor electrode.[14]

The three V_{oc} regimes of respond to the solution potential are also present in the p-Si|electroless Pt electrodes which would indicate that the barrier height of the electroless Pt is controlled by the solution potential. In addition, the p-Si|electroless Pt electrodes exhibits a consistent level of V_{oc} when compared to the same electrodes performing light-driven HER.[1, 3, 5-8, 13] This consistency between the V_{oc} attained when performing HER with the p-Si|electroless Pt electrode and the V_{oc} attained when at similar solution potential further validates the use of the vanadium redox couple.

It was found that the p-Si|e-beam Pt islands electrodes were insensitive to the changes in the solution potential and maintained a V_{oc} of 80 ± 20 mV. The p-Si|electroless Pt electrodes consistently produced a smaller V_{oc} compared to the H-terminated p-Si electrodes. The consistently smaller V_{oc} of the p-Si|electroless Pt electrode compared to the H-terminated p-Si can be attributed to partial attenuation of light by Pt particles on the surface as seen in Figure 3.

3.5.2 Structure of the Electroless Pt Photocathode

Figure 2 shows the morphology of the deposited discontinuous Pt particles after 2 min of electroless deposition the p-Si surface. Coalescing particles were considered to be single particle if there was sufficient contact between them. The particles have a wide range of areas (1300 ± 1500 nm^2) and cover 35 ± 2 % of the surface. When the area of the particles and their coverage is converted to a circular patch the effective diameter was found to be 41 ± 24 nm with an effective pitch of 61 ± 24 nm in a square configuration.

Figure 3 shows the XPS spectra of the p-Si surface after HF etch and Pt deposition treatments. Samples that had Pt deposited on the surface from exposure to the deposition solution showed significantly higher levels of oxidation as compared to the surface after chemically-producing silicon oxide by RCA-2 cleaning. Samples that had Pt deposited on the surface underwent the same HF etching process that produced the H-terminated surface. The level of surface oxidation experienced a 'slight' decrease after etching; however, the levels of silicon oxide remained greater than the chemical-produced silicon oxide. The relative oxide peak for the electroless Pt deposited surface before and after HF etching remains higher than the oxidized RCA-2 cleaned Si surface. This would suggest that the silicon oxide resides underneath the Pt particle and that the Pt particle acts as an etch barrier, thus preventing the removal of the SiO_x. Since the surface is covered by 35 ± 2% Pt particles, this can be a proxy for the silicon oxide coverage. Since the signal for silicon oxide is greater than after the entire surface is oxidized after the RCA-2 cleaning process, this would suggest that there is a greater volume of silicon dioxide that is detectable by XPS. Thus, the silicon dioxide underneath the Pt particle should extend further into the Si beyond the ~2 nm layer produced by the RCA-2 cleaning step or that the surface should be highly roughened.

The Si 2p peaks shift towards higher binding energies by 130, 320, and 130 meV relative to the H-terminated Si 2p peak for the RCA-2-cleaned, electroless Pt deposited and electroless Pt deposited after further HF etching, respectively. The Si 2p peaks show no evidence of silicide formation. The Pt 4f peaks show that the Pt deposited, by electroless deposition is metallic Pt. In addition, this shift would indicate that the bands of the p-Si are in accumulation and bent in an unfavorable direction for extraction of photogenerated carriers.

The structure of the p-Si|electroless Pt surface interface was further probed by HRTEM which can be seen in Figure 4. The HRTEM image corroborates the inferences made by XPS by showing the presence of an interfacial amorphous SiO_x layer between the Pt deposition and Si. The thickness of the amorphous SiO_x layer happened to be ~2 nm; however, the surface was roughened considerably. This surface roughness after the electroless deposition of Pt would be reflected in the XPS spectra as there would be a greater volume of SiO_x in the same area compared to smooth SiO_x interface.

3.5.3 Analogous Structured Electrode

Upon exposure to H_2 (g), the p-Si|SiO_x|e-beam Pt solid-state device exhibited a noticeable response in the resulting *J-V* characteristics. The difference in the *J-V* characteristics in air and under H_2 (g) can be seen in Figure 9. The change in the *J-V* characteristics is not just a resistive response but also a change in the barrier height. The impedance-spectroscopy of the p-Si|SiO_x|e-beam Pt solid-state device shows the flat-band potential shifts from -0.48 ± 0.1 eV to 0.35 ± 0.1 eV as seen in Figure 10. This change in the barrier height translates into a usable barrier as the p-Si|SiO_x|e-beam Pt solid-state device exhibits a photoresponse in the V_{oc} when is present H_2 (g)

and none when H_2 (g) is not present. The photoresponse of the device in H_2 (g) can be seen in Figure S3.

This voltage shift observed in the capacitance and subsequently band-bending for metal-oxide-semiconductor (MOS) devices has been well documented and studied for hydrogen sensing applications.[15-21] While various mechanisms exist and are dependent on the atmosphere and catalytic metal, all of the mechanisms involve a measurable shift in the capacitance-voltage (*C-V)* characteristics. This measurable shift originates from a dipole that is caused by the disassociation of hydrogen into protons and electrons. The protons migrate into the oxide while the electrons remain at the catalyst thus forming the dipole at the Pt-SiO_x interface.[22] In order for the shift to occur silicon oxide, catalytic metal, and H_2 (g) must be present and the change is reversible upon exposure to oxygen. The reversibility has been observed in which further supports the hydrogen-induced dipole being present. The measurement barrier height change from the p-Si|SiO_x|e-beam Pt solid-state device under H_2 (g) and the V_{oc} response (Figure S3) are consistent with typical results for performing light-driven HER on a p-Si|electroless Pt electrode.

The hydrogen-induced dipole origin for the barrier-height would suggest room for improvement as well as translation. For the p-Si|electroless Pt electrode because of the logarithmic dependence between the dipole strength and the hydrogen pressure, the barrier-height shift couple be increased by increasing the overall pressure of the system.[23]In addition, this effect is not limited to just Pt but also a host of other catalytic metals such as Pd and Ir.[18] However, there's no indication that newer generation of HER catalysts such as NiMo or CoP could generate the hydrogen-induced dipole. Thus, further investigation is necessary to determine how general the formation of the hydrogen-induced barrier is to high-performing HER catalysts.

3.5.4 Influence of Hydrogen

Upon exposure to H_2 (g), the p-Si|SiO_x|e-beam Pt solid-state device exhibited a noticeable response in the resulting *J-V* characteristics. The difference in the *J-V* characteristics in air and under H_2 (g) can be seen in Figure 9. The change in the *J-V* characteristics is not just a resistive response but also a change in the barrier height. The impedance-spectroscopy of the p-Si|SiO_x|e-beam Pt solid-state device shows the flat-band potential shifts from -0.48 ± 0.1 eV to 0.35 ± 0.1 eV as seen in Figure 10. This change in the barrier height translates into a usable barrier as the p-Si|SiO_x|e-beam Pt solid-state device exhibits a photoresponse in the V_{oc} when is present H_2 (g) and none when H_2 (g) is not present. The photoresponse of the device in H_2 (g) can be seen in Figure S3.

This voltage shift observed in the capacitance and subsequently band-bending for metal-oxide-semiconductor (MOS) devices has been well documented and studied for hydrogen sensing applications.[15-21] While various mechanisms exist and are dependent on the atmosphere and catalytic metal, all of the mechanisms involve a measurable shift in the capacitance-voltage (*C-V)* characteristics. This measurable shift originates from a dipole that is caused by the disassociation of hydrogen into protons and electrons. The protons migrate into the oxide while the electrons remain at the catalyst thus forming the dipole at the Pt-SiO_x interface.[22] In order for the shift to occur silicon oxide, catalytic metal and H_2 (g) must be present and the change is reversible upon exposure to oxygen. The reversibility has been observed in which further supports the hydrogen-induced dipole being present. The measurement barrier height change from the p-Si|SiO_x|e-beam Pt solid-state device under H_2 (g) and the V_{oc} response (Figure S3) are consistent with typical results for performing light-driven HER on a p-Si|electroless Pt electrode.

The hydrogen-induced dipole origin for the barrier-height would suggest room for improvement as well as translation. For the p-Si|electroless Pt electrode because of the logarithmic dependence between the dipole strength and the hydrogen pressure, the barrier-height shift couple be increased by increasing the overall pressure of the system.[23]In addition, this effect is not limited to just Pt but also a host of other catalytic metals such as Pd and Ir.[18] However, there's no indication that newer generation of HER catalysts such as NiMo or CoP could generate the hydrogen-induced dipole. Thus, further investigation is necessary to determine how general the formation of the hydrogen-induced barrier is to high-performing HER catalysts.

3.5.5 Mechanism for Barrier Height Formation

The data presented herein suggests that are two mechanisms for the formation of the barrier height in p-Si|electroless Pt electrodes that is dependent on the path traveled for the current. Name, for fast redox couples, the barrier-height is solution potential dependent and the *J-V* characteristics most closely resemble that of the H-terminated Si. For HER, the barrier-height is controlled by the generated barrier from H_2 (g) exposure and the *J-V* characteristics are of the p-Si|SiO_x|Pt.

First is the case in which the electrode is performing electrochemistry on a fast redox couple that requires no catalyst. These redox couples would entail redox couples like $V^{2+/3+/4+/5+}$, $Fe^{2+/3+}$ or $CoCP^{0/+}$. With these redox couples, the barrier height is determined by the solution potential which is what is observed in Figure 1.

It can be seen that as the solution potential increases, so does the V_{oc}. Since the V_{oc} is directly dependent on the barrier height and the V_{oc} scales with the solution potential then this indicates that the barrier height is scaling with the solution potential. Since the $V^{2+/3+/4+/5+}$ redox couple is sufficiently fast, no catalyst is required to perform the reaction and thus the reaction is not limited to being reduced or oxidized at the deposited Pt catalyst sites. It is more preferential for electrons to

perform the reaction at exposed H-terminated Si sites rather than traverse to the Pt catalyst because of the large resistance formed by the SiO_x underneath the Pt. The electron pathway for fast redox couples is illustrated in Figure 11a.

On the other hand, slow, catalyst-necessary reactions like HER differ from the facile redox couples since the exposed H-terminated Si no longer catalytically significant. Because the deposited Pt requires the least overpotential to drive reaction, then electrons enter/exit most favorably through the SiO_x to reach the Pt catalyst. Therefore, the *J-V* characteristics that are observed are of the junction directly underneath the Pt catalyst. The electron pathway for HER is illustrated in Figure 11b.

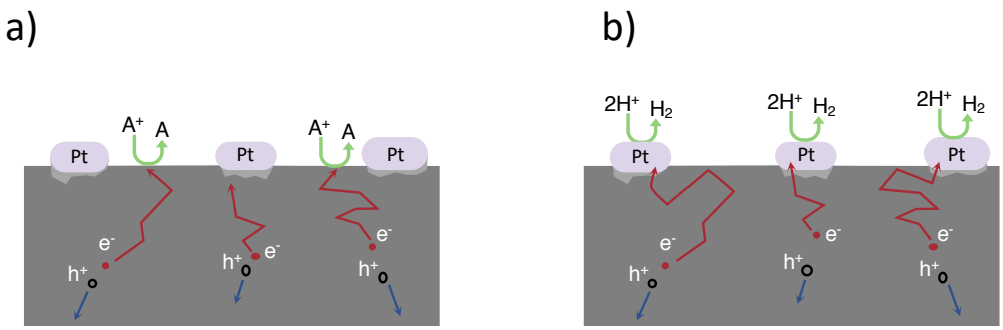

Figure 11. Schematic for a) solution-potential and b) hydrogen-dipole controlled pathways for electrons to traverse.

A mixed system was investigated in order to demonstrate that the least resistance pathway dominates the effective barrier-height. A fast, low barrier-height redox couple was used in order to demonstrate the favorable pathway. The with or without H_2 (g), the p-Si|electroless Pt electrode demonstrated an ohmic contact which shows that the most preferential exit pathway was throught the p-Si|H-terminated Si instead of through the SiO_x to reach the Pt catalyst.

3.6 Conclusions

Pt particles deposited onto p-Si via an electroless deposition method were characterized in order to determine the origins of the systems barrier height. From

physical characterization, the metallic Pt particles were deposited and separated from the p-Si via a thin amorphous SiO_x which was observable by XPS and HRTEM. The position Pt particle relative to the SiO_x makes it such that the Pt particle acts as an etch barrier, thus preventing the removal of the interfacial SiO_x. This SiO_x layer proved to be crucial in the formation of a usable barrier-height and was confirmed by creating analogous patterned electrodes.

Patterned anaologous p-Si|SiO_x|Pt electrodes after etching exposed SiO_x attained a similar level of performance as the p-Si|electroless Pt electrodes in light-driven HER as well as V_{oc} attained in the vanadium electrolyte solution. Excess SiO_x proved to be detrimental to the overall performance of the device. Without the interfacial, SiO_x, p-Si|Pt electrodes demonstrated no barrier-height formation and was insensitive to illumination.

Depending on the redox couple, the reaction will either occur at the exposed Si sites or at the Pt particle for both p-Si|electroless Pt and patterned p-Si|SiO_x|Pt electrodes. In the case of fast redox couples, the reaction preferentially occurs at the exposed Si sites, thus the observed barrier-height is solution-potential controlled. For slow redox couples that require a Pt catalyst, the reaction will preferentially occur at the Pt particle sites, thus making the observed barrier-height controlled by the junction underneath the Pt particle. In the case that hydrogen is present then the hydrogen-induced dipole will dominate the observed barrier-height underneath the Pt particle. The hydrogen-induced dipole shifts the observed barrier-height by 0.8 ± 1 eV such that the final barrier-height is 0.58±0.1 eV. This shift is observable in the *J-V* and *C-V* characteristics of the p-Si|SiO_x|Pt solid-state device. This shift in the barrier height enabled the junction underneath the Pt to be photoactive. For either mechanism for barrier-height formation, the performance of the device is independent of the size of the catalysts size.

3.7 References

1. McKone, J. R.; Warren, E. L.; Bierman, M. J.; Boettcher, S. W.; Brunschwig, B. S.; Lewis, N. S.; Gray, H. B., Evaluation of Pt, Ni, and Ni–Mo Electrocatalysts for Hydrogen Evolution on Crystalline Si Electrodes. *Energy Environ. Sci.* **2011**, *4*, 3573-3583.

2. Cabán-Acevedo, M.; Stone, M. L.; Schmidt, J.; Thomas, J. G.; Ding, Q.; Chang, H.-C.; Tsai, M.-L.; He, J.-H.; Jin, S., Efficient Hydrogen Evolution Catalysis Using Ternary Pyrite-Type Cobalt Phosphosulphide. *Nat. Mater.* **2015**, *14*, 1245.

3. Boettcher, S. W.; Warren, E. L.; Putnam, M. C.; Santori, E. A.; Turner-Evans, D.; Kelzenberg, M. D.; Walter, M. G.; McKone, J. R.; Brunschwig, B. S.; Atwater, H. A., Photoelectrochemical Hydrogen Evolution Using Si Microwire Arrays. *J. Am. Chem. Soc.* **2011**, *133*, 1216-1219.

4. Warren, E. L.; McKone, J. R.; Atwater, H. A.; Gray, H. B.; Lewis, N. S., Hydrogen-Evolution Characteristics of Ni–Mo-Coated, Radial Junction, n^+ p-Silicon Microwire Array Photocathodes. *Energy Environ. Sci.* **2012**, *5*, 9653-9661.

5. Dominey, R. N.; Lewis, N. S.; Bruce, J. A.; Bookbinder, D. C.; Wrighton, M. S., Improvement of Photoelectrochemical Hydrogen Generation by Surface Modification of p-type Silicon Semiconductor Photocathodes. *J. Am. Chem. Soc.* **1982**, *104*, 467-482.

6. Heller, A.; Aharon-Shalom, E.; Bonner, W.; Miller, B., Hydrogen-Evolving Semiconductor Photocathodes: Nature of the Junction and Function of the Platinum Group Metal Catalyst. *J. Am. Chem. Soc.* **1982**, *104*, 6942-6948.

7. Lombardi, I.; Marchionna, S.; Zangari, G.; Pizzini, S., Effect of Pt Particle Size and Distribution on Photoelectrochemical Hydrogen Evolution by p-Si Photocathodes. *Langmuir : the ACS journal of surfaces and colloids* **2007**, *23*, 12413-12420.

8. Maier, C.; Specht, M.; Bilger, G., Hydrogen Evolution on Platinum-Coated p-Silicon Photocathodes. *International journal of hydrogen energy* **1996**, *21*, 859-864.

9. Heller, A.; Lewerenz, H.; Miller, B., Silicon Photocathode Behavior in Acidic Vanadium (II)-Vanadium (III) Solutions. *J. Am. Chem. Soc.* **1981**, *103*, 200-201.

10. Heller, A.; Miller, B.; Lewerenz, H.; Bachmann, K., An Efficient Photocathode for Semiconductor Liquid Junction Cells: 9.4% Solar Conversion Efficiency with p-InP/VCl_3-VCl_2-HCl/C. *J. Am. Chem. Soc.* **1980**, *102*, 6555-6556.

11. Heller, A.; Miller, B.; Thiel, F., 11.5% Solar Conversion Efficiency in the Photocathodically Protected p‐InP/V^{3+}‐V^{2+}‐HCI/C Semiconductor Liquid Junction Cell. *Appl. Phys. Lett.* **1981**, *38*, 282-284.

12. Grimm, R. L.; Bierman, M. J.; O'Leary, L. E.; Strandwitz, N. C.; Brunschwig, B. S.; Lewis, N. S., Comparison of the Photoelectrochemical Behavior of H-Terminated and Methyl-Terminated Si (111) Surfaces in Contact with a Series of One-Electron, Outer-Sphere Redox Couples in CH_3CN. *J. Phys. Chem. C* **2012**, *116*, 23569-23576.

13. Jiang, J.; Huang, Z.; Xiang, C.; Poddar, R.; Lewerenz, H. J.; Papadantonakis, K. M.; Lewis, N. S.; Brunschwig, B. S., Nanoelectrical and Nanoelectrochemical Imaging of Pt/p‐Si and Pt/p^+‐Si Electrodes. *Chemsuschem* **2017**, *10*, 4657-4663.

14. Rosenbluth, M. L.; Lewis, N. S., " Ideal" Behavior of the Open Circuit Voltage of Semiconductor/Liquid Junctions. *The Journal of Physical Chemistry* **1989**, *93*, 3735-3740.

15. Lundstrom, I., Why Bother About Gas-Sensitive Field-Effect Devices? *Sensors and Actuators a-Physical* **1996**, *56*, 75-82.

16. Lundström, I.; Shivaraman, S.; Svensson, C.; Lundkvist, L., A Hydrogen−Sensitive MOS Field− Effect Transistor. *Appl. Phys. Lett.* **1975**, *26*, 55-57.

17. Lundström, K.; Shivaraman, M.; Svensson, C., A Hydrogen‐Sensitive Pd‐Gate MOS Transistor. *J. Appl. Phys.* **1975**, *46*, 3876-3881.
18. Hubert, T.; Boon-Brett, L.; Black, G.; Banach, U., Hydrogen Sensors - A Review. *Sens. Actuators, B* **2011**, *157*, 329-352.
19. Spetz, A.; Armgarth, M.; Lundström, I., Hydrogen and Ammonia Response of Metal‐Silicon Dioxide‐Silicon Structures with Thin Platinum Gates. *J. Appl. Phys.* **1988**, *64*, 1274-1283.
20. Lundström, I.; Svensson, C.; Spetz, A.; Sundgren, H.; Winquist, F., From Hydrogen Sensors to Olfactory Images—Twenty Years with Catalytic Field-Effect Devices. *Sensors and Actuators B: Chemical* **1993**, *13*, 16-23.
21. Löfdahl, M.; Eriksson, M.; Johansson, M.; Lundström, I., Difference in hydrogen Sensitivity Between Pt and Pd Field-Effect Devices. *J. Appl. Phys.* **2002**, *91*, 4275-4280.
22. Lundström, I.; Söderberg, D., Hydrogen Sensitive Mos-Structures Part 2: Characterization. *Sensor Actuator* **1981**, *2*, 105-138.
23. Dannetun, H.; Petersson, L.-G.; Söderberg, D.; Lundström, I., A Hydrogen Sensitive Pd-MOS Structure Working over a Wide Pressure Range. *Applications of surface science* **1984**, *17*, 259-264.

3.8 Supplementary Information

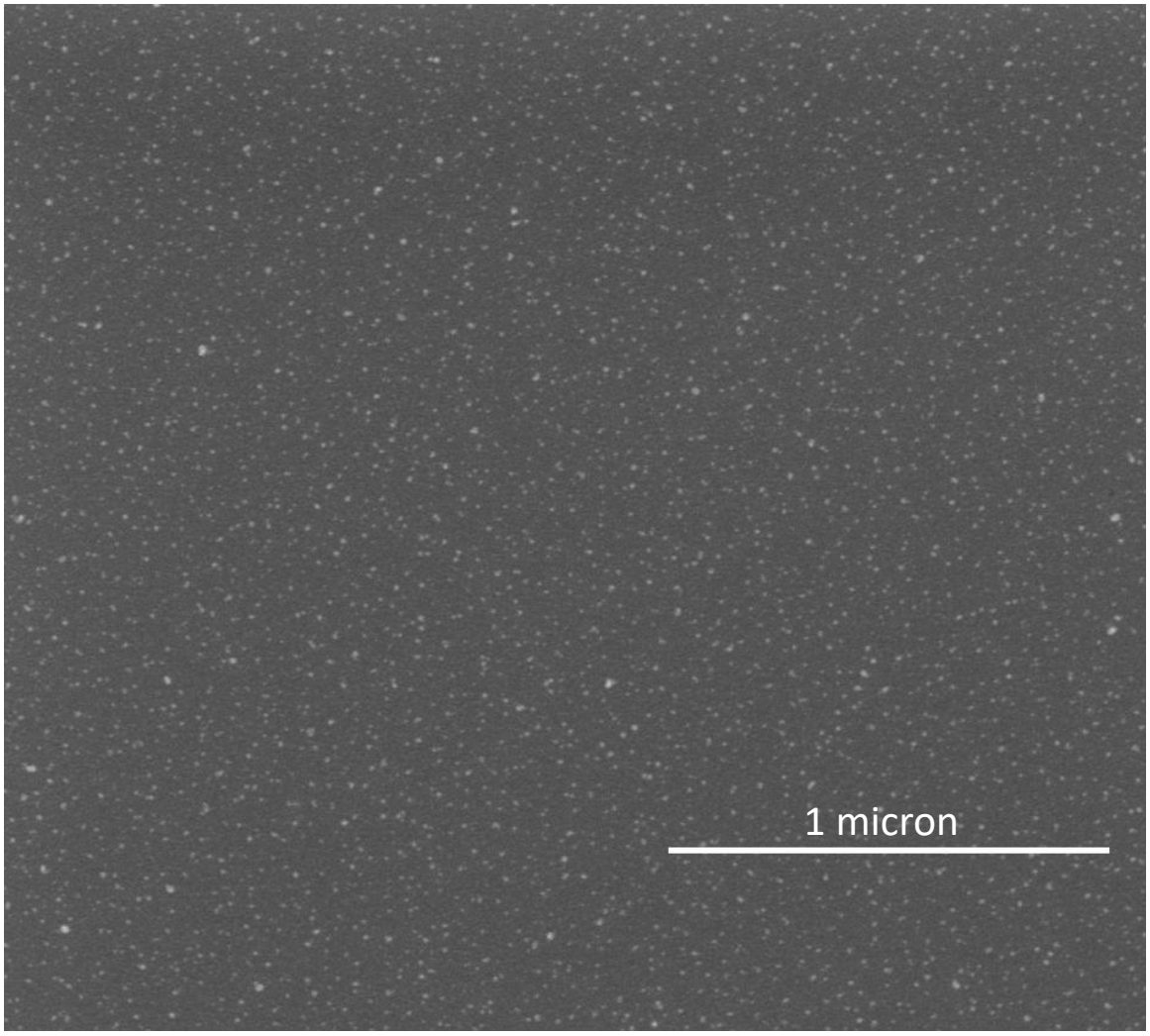

Figure S1. SEM micrograph of "2 nm" of Pt deposited by e-beam deposition on the surface of p-Si. Coverage was found to be 0.05 ± 0.01. Overall the average area for each particle was found to be 74 ± 61 nm^2, which results in an effective diameter of 4.8 ± 4.4.

Figure S2 show an HRTEM image of the surface interface for p-Si|SiO_x|e-beam Pt. In the HRTEM image for p-Si|SiO_x|e-beam Pt we observed the presence of an interfacial amorphous SiO_x layer which was formed by RCA treatment. The interfacial amorphous SiO_x has a uniform thickness of 1.7–1.9 nm between the e-beam Pt layer and the silicon surface. In addition, the surface of the underlying Si surface is smooth.

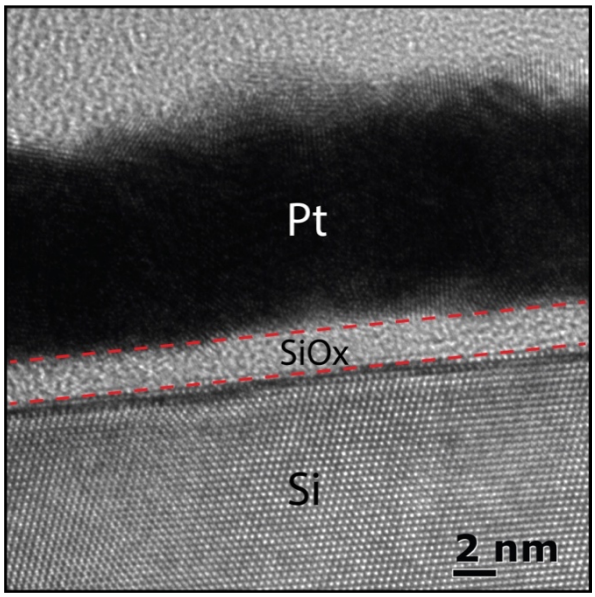

Figure S2. High-resolution electron microscopy (HRTEM) images of the that p-Si|SiO_x|e-beam Pt surface interface. Dashed red lines were added to highlight the boundary of the interfacial silicon oxide (SiO_x) layer.

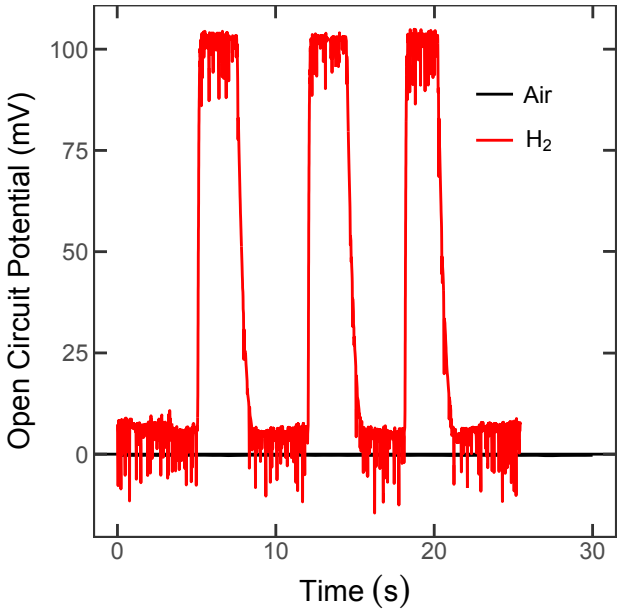

Figure S3. Open circuit potential (V_{oc}) of a p-Si|SiO_x|Pt solid-state device under chopped 1 sun of illumination in air and H_2 (g). Under an atmosphere of air, the device produces no V_{oc}. Under H_2 (g), a barrier-height is generated which can produce a V_{oc} of ~100 mV.